

CHAPTER 1 INTRODUCTION

1. Significance and purposes

1.1 Significance

Ferroelectric, ferroelastic, and ferromagnetic materials have been extensively studied for potential applications in sensors, actuators and transducers. Electrostrictive $\text{Pb}(\text{Mg}_{1/3}\text{Nb}_{2/3})\text{-xPbTiO}_3$ (PMN-xPT) crystals with ultrahigh electromechanical properties [1] ($d_{33}>2500\text{pC/N}$, $d_{15}>5500\text{pC/N}$ [2], $k_{33}>94\%$, strain $>1.7\%$) and magnetostrictive Fe-xat.%Ga (Fe-xGa) alloys with large magnetostriction ($3\lambda_{(100)}/2\sim 400\text{ppm}$) [3,4] are two novel materials systems being studied for such purposes.

The structure of PMN-xPT is ABO_3 perovskite, where the B site is occupied by Mg^{2+} , Nb^{5+} or Ti^{4+} ions. A chemical heterogeneity on the microscale is due to fluctuations of the B-site occupancy. Variation in the concentrations on B-site cations gives rise to interesting crystal structure and physical property relationships, dependent on thermal and electrical histories of the crystals. Analogously, in Fe-xGa alloys, the addition of Ga atoms into the bcc $\alpha\text{-Fe}$ phase results in phase separations and structural heterogeneity, where the magneto-elastic properties and phase stability can also be altered by the thermal and magnetic histories.

1.2 Purposes

The purpose of this thesis was to investigate the phase transformations in PMN-xPT and Fe-xGa crystals which have various thermal and field (electrical/magnetic) histories. It is hoped that an understanding of the similarities of local structural behaviors will provide an intellectual paradigm by which new generations of sensor and actuator materials can be designed by domain engineering of systems having apparent phase fragility.

Specifically, the goals of my thesis are as follows:

(1) PMN-xPT crystals

- use high resolution x-ray diffraction to determine the phase transformational sequence under electric field along various crystallographic orientations, [001], [110] and [111];
- determine how the phase stability is dependent on electrical and thermal histories;
- use neutron inelastic scattering to investigate lattice dynamics and how the results relate to structural heterogeneity.

(2) Fe-xGa alloys

- measure the magnetostriction under different stress, magnetic field and thermal histories;
- use high resolution x-ray diffraction to investigate structural transformations and phase stability under for crystals of different thermal histories;
- use neutron diffuse scattering to investigate fine scale decomposition products, structural heterogeneity and short-range chemical ordering;

1.2. Ferroelectricity and ferroelectric materials

1.2.1 Ferroelectricity and perovskite ferroelectrics

The definition of a ferroelectric is a nonlinear polarizable and deformable solid. A crystal is said to be ferroelectric when it possesses at least two equilibrium orientations of the spontaneous polarization in the absence of an external electric field, and the spontaneous polarization can be switched between the orientations by an applied electric field (E). Figure 1 present a typical hysteresis loop, illustrating the polarization switching in ferroelectric materials. Important materials parameters, such as coercive field (E_c), and remnant polarization (P_r) are indicated in the figure.

The cord carrying characteristic of a ferroelectric is the spontaneous polarization (P), which is a polar vector. It develops as a result of a symmetry reducing phase transformation that displaces positive and negative charges along a restricted family of crystallographic directions, resulting in a permanent electric dipole moment. To be ferroelectric, this dipole

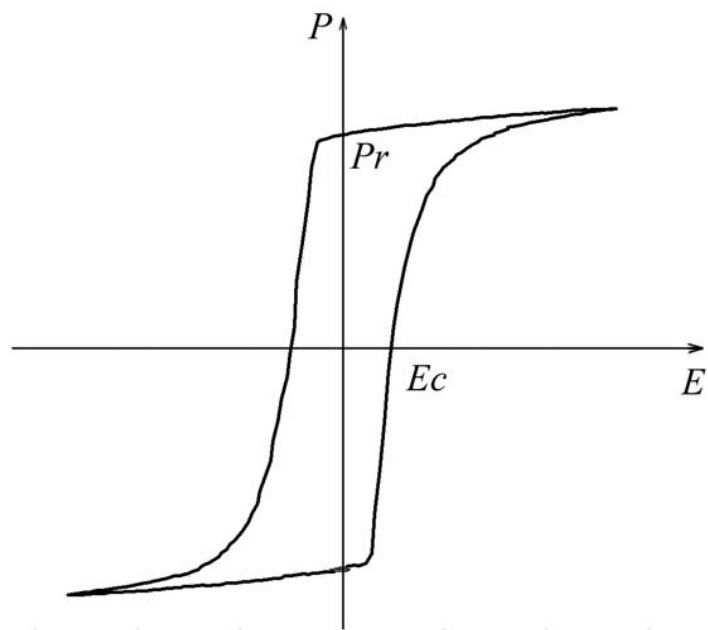


Figure 1.1 Sketch of ferroelectric hysteresis loop illustrating the polarization switching under an external electric field.

moment must have two or more crystallographic equivalent directions. Amongst the 32 crystal point groups, only eleven of them are characterized by the existence of a center of symmetry, which by application of Neuman's Principle [5] can not possess polar properties. The remaining twenty-one do not have a center of symmetry: thus, making it possible to possess (i) one or more polar axes, and (ii) odd-rank tensor properties. There is only one exception: the point group 432 which lacks of a center of symmetry, but has other symmetry operation that destroys polarity. All twenty non-center-symmetric point groups exhibit piezoelectricity which is defined by a change in electric charge under an external stress, and vice versa. Out of twenty piezoelectric classes, only ten possess a spontaneous polarization. These ten point groups must also be pyroelectric, in addition to piezoelectric. This requirement restricts the point groups to those that have a reversible polarization. These are necessary, but not sufficient criteria, for a crystal to be ferroelectric.

Among all ferroelectrics, the most extensively studied and widely used ones are the perovskites, which have a general formula of ABO_3 (where the valences of AB could be either $A^{+2}B^{+4}$, $A^{+3}B^{+3}$, or $A^{+1}B^{+5}$). Figure 1.2 presents a sketch of the ABO_3 unit cell: six face centers are occupied by O anions, eight corners are occupied by A ions, and one body center is occupied by B ions which is located at the center of the oxygen octahedron. The B site ions are relatively small compared to the size of the oxygen octahedron, and thus move relatively freely inside the oxygen octahedron with relative small restoration forces. The polarization in perovskite ferroelectrics originates from the displacement of the B ions along one of three high symmetric axes, relative to the octahedral center.

1.2.2 Phenomenological and Macroscopic theories for various ferroelectrics

Ferroelectric transformations are typical structural phase transitions, which can be described using Landau thermodynamic phenomenology, where the free energy is expanded in a Taylor series expansion in terms of an order parameter. Landau theory originally was applied to continuous (or 2nd order) phase transitions; however, it was later applied to 1st order phase (discontinuous) transitions by making some appropriate modifications. In a classic 1949 paper [6], Devonshire was able to explain the observed paraelectric phases and

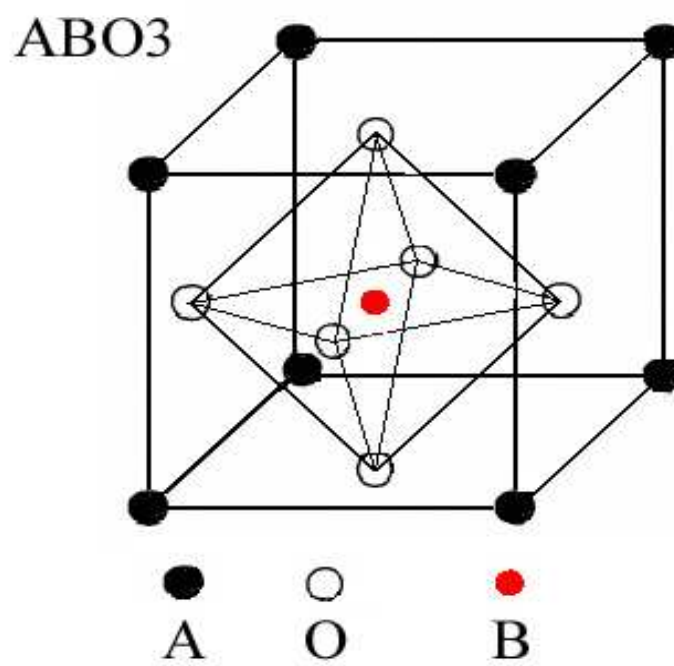


Figure 1.2 Sketch of the unit cell of perovskite structure ABO₃ in ferroelectrics.

phase transition sequences of BaTiO₃ using a phenomenological Landau-type expansion of the free energy in terms of a ferroelectric order parameter \mathbf{P} . Making use of cubic symmetry and truncating the expansion to sixth rank in \mathbf{P} , Devonshire arrived at a simple model with only a single temperature-dependent second-order coefficient, and only three temperature-independent higher-rank coefficients. This model successfully predicted the phase transition sequence and the piezoelectric, dielectric and other properties of BaTiO₃ [7]. With a simple modification of the anharmonic coefficients (i.e. higher rank), the behavior of PbTiO₃ could also be qualitatively reproduced. Later, investigations have made advancements in understanding more complex behavior in ferroelectric solutions, such as Pb(Zr_xTi_{1-x})O₃.

Following a basic Landau-Devonshire theory [8], one assumes that the free energy (in one dimension) can be expanded in a power series of the order parameter \mathbf{P} , given as:

$$G(P, T, E) = -EP + G_0 + \frac{1}{2} \alpha P^2 + \frac{1}{4} \beta P^4 + \frac{1}{6} \gamma P^6 + \dots, \quad (1.1)$$

where the coefficients α , β , γ are the 2nd, 4th, and 6th dielectric stiffnesses. For BaTiO₃, only the 2nd rank stiffness is temperature dependent, but this restriction can be relaxed for more complex behaviors. This series expansion does not contain terms in odd powers of \mathbf{P} : this restriction is based on the assumption that the high temperature prototype (paraelectric) phase has a center of symmetry, which is generally true for most perovskite ferroelectrics. One can obtain an expression for the spontaneous polarization \mathbf{P} in thermal equilibrium, by minimizing the free energy as a function of \mathbf{P} ; i.e., by differentiating Eq. 1.1 with respect to \mathbf{P} given as:

$$\frac{\partial G}{\partial P} = -E + \alpha P + \beta P^3 + \gamma P^5 + \dots \quad (1.2)$$

The temperature dependence of the coefficient α is known to take the form $\alpha = a_0(T - T_0)$, where α_0 is zero or positive, and T_0 is called Curie-Weiss temperature, and may be equal to or smaller than the phase transition temperature, T_C (or Curie temperature). The form of α is a necessary result of mean field theory, and its validity is supported by the experimentally observed Curie-Weiss law. The 2nd rank stiffness can be obtained from $\frac{\partial^2 G}{\partial P^2}$ in (1.1) and

under the condition of $P=0$, given as:

$$\frac{\partial^2 G}{\partial P^2} = \frac{\partial E}{\partial P} \Big|_{P=0} = \frac{1}{\varepsilon} = \alpha = \alpha_0(T - T_0). \quad (1.3)$$

The relation given in (1.3) is the Curie-Weiss law, i.e., $\varepsilon_r \approx \frac{C}{(T - T_0)}$. A negative value of

α would mean that the unpolarized state is unstable, i.e., the system is ferroelectric.

Following (1.3), the polarization under zero electric field can then be obtained as:

$$0 = \alpha P + \beta P^3 + \gamma P^5. \quad (1.4)$$

From this relation, the value of polarization is either $P=0$ or $P^2 = -\frac{\beta}{2r} \{1 \pm [1 - 4\alpha_0\gamma\beta^{-2}(T - T_0)]^{1/2}\}$. Since P can not be negative, the non-zero solution of P^2 in Eq. (1.4) is $-\frac{\beta}{2r} \{1 + [1 - 4\alpha_0\gamma\beta^{-2}(T - T_0)]^{1/2}\}$ with $\beta < 0$ (1st order phase transition); or $-\frac{\beta}{2r} \{1 - [1 - 4\alpha_0\gamma\beta^{-2}(T - T_0)]^{1/2}\}$ with $\beta > 0$ (2nd order phase transition). From (1.2), the dielectric impermeability can also be derived as:

$$\lambda = \frac{1}{\varepsilon} = \frac{\partial E}{\partial P} = \frac{\partial^2 G}{\partial P^2} = \alpha_0(T - T_0) + 3\beta P^2 + 5\gamma P^4. \quad (1.5)$$

In the paraelectric phase, there is no spontaneous polarization. Accordingly, (1.5) simplifies into (1.3). However, in the ferroelectric phase, (1.5) after substituting P^2 is:

$$\lambda = -4\alpha_0(T - T_0) + \beta^2\gamma^{-1} \{1 \pm [1 - 4\alpha_0\gamma\beta^{-2}(T - T_0)]^{1/2}\} \quad (1.6)$$

1.2.3 Microscopic Theories for Ferroelectrics – Soft Modes

Thermal dynamical theory for ferroelectric transformations provides a macroscopic theory, which was 1st reported in the late 1940's and early 1950's for BaTiO₃. However, a microscopic theory was lacking until the 1960's. It was only then that Cochran and Anderson [9] advanced the proposition that the ferroelectric phase transition possessed a unique lattice dynamics, where there was a “softening” of a transverse optical phonon mode (TO) in the Brillouin zone center. An optical mode has positive and negative ions that vibrate in opposing motions. A “softening” of the phonon mode here means that the vibration frequency decreases with decreasing temperature. At the Curie temperature (T_C), the soft mode

condenses causing a static displacement of ions in the lattice. This static displacement of ions occurs away from centric positions, resulting in spontaneous polarization that is directed along particular crystallographic directions. Please note that this transition is displacive, rather than reconstructive, as bonds do not need to be broken. Rather the low temperature low symmetric phase is structurally related to the high temperature high symmetry one.

Softening of a phonon mode is illustrating in Figure 1.3. In prototypical ferroelectrics, such as PbTiO_3 (PT), it is well known that the condensation or softening of a zone-center, transverse optic (TO) phonon mode is responsible for the cubic to tetragonal (C \rightarrow T) ferroelectric transition [10]. This softening is typically characterized by measuring energy profiles of inelastically scattered neutrons. The square of the soft mode frequency $(\hbar\omega_0)^2$ varies linearly with temperature both below and above the Curie point (T_C), following the Lyddane-Sachs-Teller (LST) relationship [11], given as:

$$\omega^2 = \alpha_0(T - T_0), \quad (1.7)$$

where α_0 is a temperature independent constant. For PbTiO_3 as shown in Figure 1.3, the value of $T_0 \approx 440^\circ\text{C}$ can be obtained by extrapolation of $\omega^2 \rightarrow 0$. This value of T_0 is smaller than that of T_C (490°C). The difference between T_C and T_0 is a measure of the degree of first-order character for the phase transition. The prediction of (1.7) and the results of Figure 1.3 show microscopically that ferroelectricity results from a collective behavior of lattice vibrations, i.e., a phonon mode. This mode possesses a unique dynamics and results in non-centre-symmetric static lattice distortion on cooling into the low temperature phase. This microscopic theory successfully accounts for the nonlinear, polarizable, deformable nature of a ferroelectric state.

1.2.4 PMNT and PZNT single crystals

Ferroelectric materials that have large piezoelectric and electrostrictive properties are widely used in actuators, sensor and transducers. These electromechanical applications require high forces, high drive frequencies, accurate displacement resolutions, and fast response times. The perovskite ferroelectric BaTiO_3 was initially used after its discover in these times.

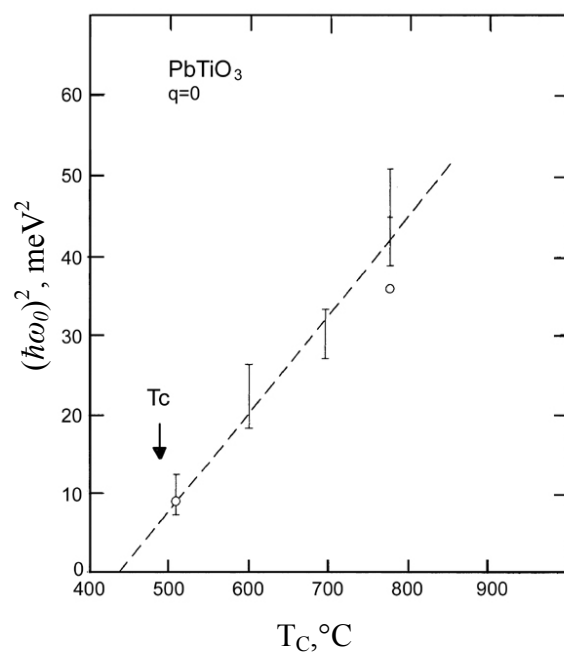


Figure 1.3 Soft-mode energy $\hbar\omega_0$ as a function of temperature. Reprinted with permission from [10]. Copyright [1970], American Physical Society.

The perovskite ferroelectric BaTiO₃ was initially used after its discover in these applications, but was found to have insufficient magnitudes of the longitudinal piezoelectric (d_{33}) and electromechanical coupling (k_{33}) coefficients. Subsequent research revealed that Pb(Zr,Ti)O₃ (PZT) ceramics had much higher value of d_{33} and k_{33} , and have since served as the foundation of the transducer industry for the last 40 years. Compositionally, PZT lies near a morphotropic phase boundary (MPB), which is a nearly vertical boundary in composition spectrum between tetragonal and rhombohedral ferroelectric phases. Near this boundary, anomalous dielectric and piezoelectric properties ($d_{33} \leq 500$ pC/N with strains of \leq up to 0.15%) have been found [12]. Originally, the large electromechanical effects near the MPB, was rationalized by two equivalent energy states, i.e., tetragonal and rhombohedral ones. Alternative electromechanical materials are electrostrictive ceramics, such as Pb(Mg_{1/3}Nb_{2/3})O₃ [13], which were developed in the late 1980's. They offer higher piezoelectric constant of $d_{33} > 800$ pC/N; large induced strains are possible, but in practice are often limited by dielectric breakdown strength before polarization saturation is achieved.

The most exciting breakthrough in high performance piezoelectric materials was the development of large Pb(Mg_{1/3}Nb_{2/3})-xPbTiO₃ (PMN-PT) and Pb(Zn_{1/3}Nb_{2/3})-xPbTiO₃ (PZN-PT) single crystals [1]. In March 1997, it was reported in the magazine Science that single crystals of PMN-PT and PZN-PT (for the compositions in the vicinity of MPB) had extreme piezoelectric properties [15], much higher than that of conventional PZT ceramics. For example, ultrahigh piezoelectric ($d_{33} > 2500$ pC/N, $d_{15} > 5000$ pC/N [2]) and electromechanical coupling ($k_{33} > 94\%$) coefficients have been reported in PMN-xPT ($0.30 \leq x \leq 0.33$) for crystals that were domain engineered [1]. Figure 1.4 illustrates the strain vs. electric field (E) behavior for PZN-xPT and PMN-xPT crystals, and for various conventional electromechanical ceramics [1].

1.2.5 Structural origin of ultra-high electro-mechanical properties in PMNT and PZNT

Ultrahigh piezoelectric constants and field-induced strains – an order of magnitude larger than those of conventional piezoelectric ceramics – have been reported for ‘*domain-engineered*’ (001)-oriented PMN-xPT and PZN-xPT crystals for compositions close to the MPB. Early investigations attributed the high electromechanical properties of Pb(Zr_{1-x}Ti_x)O₃

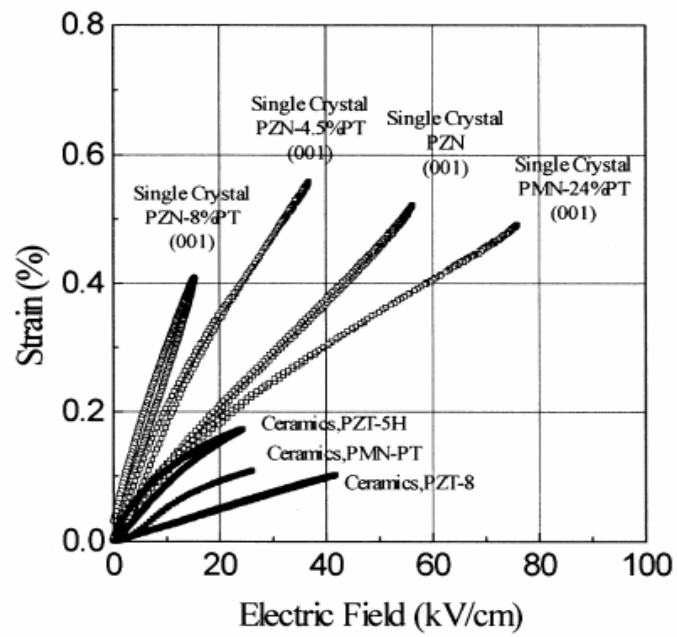


Figure 1.4 Comparison of strain behaviors under an external electric field below PMN-xPT and PZN-xPT single crystals and various PZT ceramics. Reprinted with permission from [1]. Copyright [1997], American Institute of Physics.

ceramics to domain (or ‘*extrinsic*’) contributions due to the nearly-vertical MPB between rhombohedral (R) and tetragonal (T) ferroelectric phases, resulting in phase coexistence [15]. This coexistence of two phases results in an enhanced probability of the redistribution of spontaneously polarized domains under electric field, i.e. a reduced anisotropy. For an example, the polarization in the tetragonal or orthorhombic (O) phase has six or eight possible orientations, respectively: therefore, in a region of two phase coexistence, there could be 14 possible orientations.

Understanding of the structural origin of the high electromechanical properties of the MPB compositions has undergone an evolution in thought, including (i) the electric-induced ferroelectric phase transition from tetragonal (T) to rhombohedral (R) or T→R proposed by Park and Shrout [1, 16]; (ii) to the discovery of various bridging monoclinic phases [17]; (iii) to the polarization rotation theory emphasized by Fu and Cohen [18]; and (iv) to a theory of adaptive ferroelectric nanotwins [19, 20].

E-field induced ferroelectric phase transition

Coincidental with their discovery of the high electromechanical properties in oriented PMN-xPT and PZN-xPT crystals, Park and Shrout conjectured that the ultrahigh strain under applied electric fields was due to a R→T phase transition induced by E. Figure 1-5 shows the high-field strain behavior for (001)-oriented PZN-0.08PT crystal [1].

Three regions designed as A, B and C are illustrated in this figure, indicating three different strain behavior regions distinguished by external electric field. The two insets show the R and T domain states for E//[001], which correspond to regions A and region C. However, Park and Shrout considered region B to be associated with T and R phase coexistence. Under zero field, the R phase has eight possible polarization orientations along the <111>. When a modest electric field applied along the [001] direction, the four top polar vectors are energetically favored over that of the bottom ones, as shown in the left inset. In this case, a strain is induced and the polarization slightly inclined towards that of the applied field, in a matter equivalently for the four top polar vectors. Thus, for region A, the

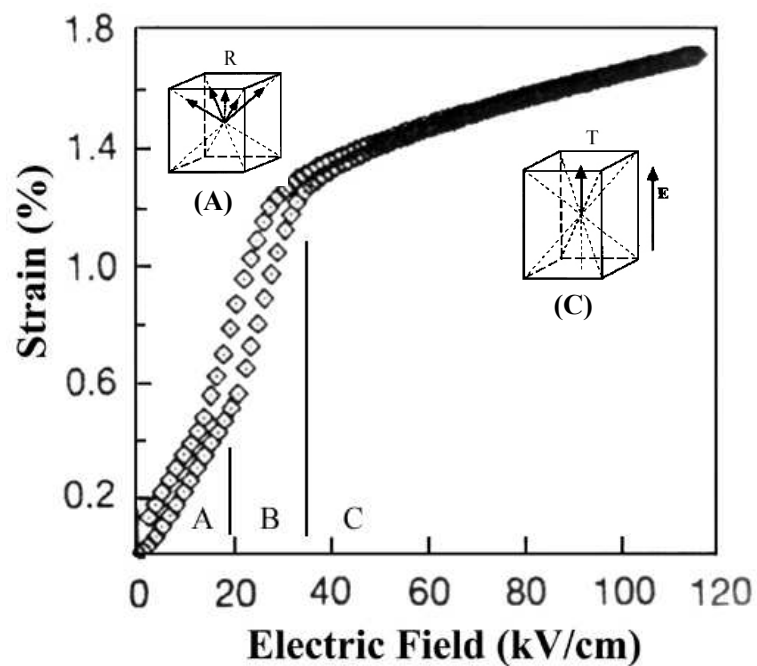


Figure 1.5 Strain response under an external electric field for (001) oriented PMN-0.8PT crystal [1]. The low electric field region A has a rhombohedral phase with four upward polar vectors along the direction of electric field; the high electric field region C has a single-domain like tetragonal phase; whereas the medium field region B connect the region A and C, indicating a $R \rightarrow T$ phase transition. Reprinted with permission from [1]. Copyright [1997], American Institute of Physics.

electrically induced strain was expected to result in an enhanced R lattice distortion. Likewise, enhanced d_{33} values (i.e., $\partial\epsilon_3/\partial E_3$) would occur in this region A. However, with increasing E, there is an abrupt change in slope for the ϵ -E curve, as region B is entered. Park and Shrout attributed this change to an electric-field induced R→T two phase region. A larger value of d_{33} was expected in region B, due to the larger c/a ratio of the T phase regions. Upon further increase of E, the ϵ -E curve becomes flat and tends towards saturation. In this region C, the T phase field is near fully stabilized, with their polar vectors fixed along the [001] direction, i.e., a single-domain T phase is induced. Furthermore, the region C has been shown by x-ray diffraction (XRD) to have tetragonal symmetry.

Please note that the slim-loop nature of the ϵ -E curves is not conventional of an induced transition, which is generally expected to be strongly hysteretic. Actually, much more complicated but very interesting structural information was covered up in the elegant reversible electric-field-induced strain behavior, as will be illustrated in the following.

Discovery of Various Monoclinic Phases

Subsequently, x-ray diffraction and neutron diffraction experiments have shown the existence of various monoclinic (M) bridging phases in PZT [17] and PMN-xPT [21] ceramics and in oriented PZN-xPT [22-25] and PMN-xPT [26-29] crystals. Two types of monoclinic distortions M_A and M_C have been reported, which correspond to space groups Cm and Pm , respectively. The M_A and M_C notations are adopted following Vanderbilt and Cohen [30]. The M_A unit cell has a unique b_m axis along the [110] direction, and is doubled and rotated 45° about the c -axis, with respect to the pseudocubic cell; whereas, the M_C unit cell is primitive having a unique b_m axis that is oriented along the pseudocubic [010]. A third monoclinic M_B phase has also been predicted by Vanderbilt and Cohen [30]: although both the M_A and M_B phases belong to the Cm space group, the difference lies in the magnitudes of the components of the polarization corresponding to the pseudocubic cell: for the M_A phase, $P_x=P_y<P_z$, whereas for the M_B phase, $P_x=P_y>P_z$. In addition, an O ferroelectric phase has been reported to be induced by E in (001) PZN-0.08PT [22] crystals. This O phase is the limiting case of a M_C phase, which can be considered as $a_m=c_m$, similar to that of BaTiO₃ [31]. The polarization vectors for various ferroelectric phases, including T and R phases

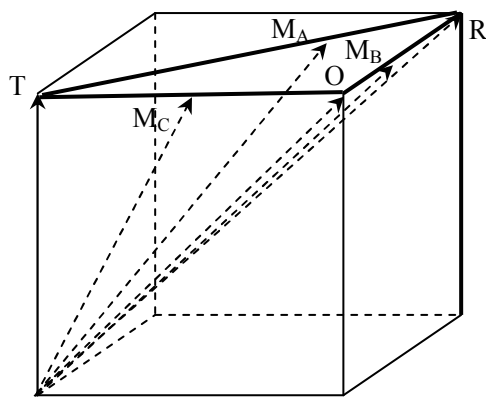


Figure 1.6 Illustration of rotation of polarization vectors in perovskite unit cells. The thick lines represent the paths followed by the end of the polarization vector of rhombohedral (R) and tetragonal (T), orthorhombic (O) and monoclinic M_C , M_A M_B phases. The M_A , M_B and M_C notation is adopted following Vanderbilt and Cohen [30].

within a perovskite unit cell are shown in Figure 1.6. Recent neutron diffraction studies of the effect of an electric field on PZN-0.08PT by Ohwada *et al.* [25] have shown that a $C \rightarrow T \rightarrow M_C$ transformational sequence occurs when field cooled (FC), and that a $R \rightarrow M_A \rightarrow M_C \rightarrow T$ sequence takes place with increasing E at 350 K beginning from the zero-field-cooled (ZFC) condition. A recent study by Bai *et al.* [29] established that PMN-0.30PT has a $C \rightarrow T \rightarrow M_C \rightarrow M_A$ sequence in the FC condition, and a $R \rightarrow M_A \rightarrow M_C \rightarrow T$ one with increasing E beginning from the ZFC. Optical domain studies also have shown the existence of M phases in PMN-0.33PT crystal by Xu *et al.* [32]. Dielectric property studies of PMN-0.33PT [33] crystals with $E // [110]$ have reported a metastable O (or limiting M_C) phase, bridging T and R ones over a narrow temperature range in the FC condition. Polarized light microscopy (PLM) indicated that this O phase was a single domain one. These prior studies clearly evidence that the phase stability of PMN-xPT crystals is altered by electrical history and by crystallographic direction along which that E is applied. However, a systematic investigation of the phase stability has not yet been performed over a wide compositional range of x .

Polarization Rotation Theory

Monoclinicity may be important in that it allows the polarization vector to be unconstrained within a plane [18], rather than constricted to a particular crystallographic axis as for the higher symmetry R, T, or O phases. According to the polarization rotation theory, the high electromechanical properties of ferroelectric monoclinic phases are due to the rotation of the polarization vector within a symmetry-allowed plane.

BaTiO₃ has R and T ferroelectric phases in a perovskite cell, and can serve as a prototypical model for other perovskite system. Based on the study of the R phase of BaTiO₃ single crystals as a E function applied along [001], Fu and Cohen proposed a polarization rotation theory [18]. Subsequently, they conjectured that the large piezoelectric response of the M phases of PMN-xPT and PZN-xPT crystals was due to changes in unit cell parameters due to a rotation of the polarization direction induced by electric field. Its piezoelectric properties have been reported to be enhanced in the R phase. These authors selected different polarization directions and calculated their internal energies using a 1st principle linearized

augmented plane wave (LAPW) method, with a local density-functional approximation (LDA).

Figure 1-6 illustrates a schematic of possible polarization rotation paths from $P//[111]$ to $P//[001]$ under an external electric field beginning from a rhombohedral phase of perovskite. The thick lines represent the paths followed by the end of the polarization vectors of the R and T, O, M_A , M_B and M_C phases. Fu and Cohen found that the $R \rightarrow M_A \rightarrow T$ pathway was energetically easier to access than the $R \rightarrow M_A \rightarrow M_C \rightarrow T$ as $E//[001]$, where “easier” means that lower applied electric fields are required. Although the polarization rotation mechanism was first based on ab-initio calculations of the R phase of $BaTiO_3$, it is reasonable to conceptually extend its application to other more complex ferroelectric systems: such as PZT, PMN-PT or PZN-PT. Different systems could be expected to have different polarization rotation paths. For example, in PZN-0.045PT [24], $E//[001]$ would induce polarization rotation in the (110) plane following the $R \rightarrow M_A \rightarrow T$ path, similar to that predicted by ab-initio calculations in the R phase of $BaTiO_3$. The same rotation path can also be expected for PMN-PT under $E//[001]$ for compositions of at the left side of the MPB (i.e. $x < 0.30$). Experimentally, a $M_A \rightarrow M_C$ transition has been reported by XRD in PZN-0.08PT [25] and in PMN-0.30PT [29]. Accordingly, the polarization rotation would follow a $R \rightarrow M_A \rightarrow T$ path, but then abruptly jump to a $R \rightarrow M_A \rightarrow M_C \rightarrow T$ one. Polarization rotations could also occur in the T phase: for example, $T \rightarrow M_A \rightarrow R$ under $E//[111]$ [34].

In summary, the polarization rotation theory predicts a giant piezoelectric response. This model can explain the origin of the extreme piezoelectric response observed in giant ferroelectric perovskite phases, where electric field is applied along a different orientation than that of the polarization direction of the phase. It is founded on the underlying assumption that the polarization rotation occurs in a homogeneous monoclinic phase. This is a reasonable assumption, because monoclinic phases were found by diffraction, but is valid only if the optical conditions for diffraction resolution are satisfied.

Ferroelectric Adaptive Phase Theory

The polarization rotation theory can provide an interpretation to the variously observed monoclinic phases. However, it can not explain special observed relations between the

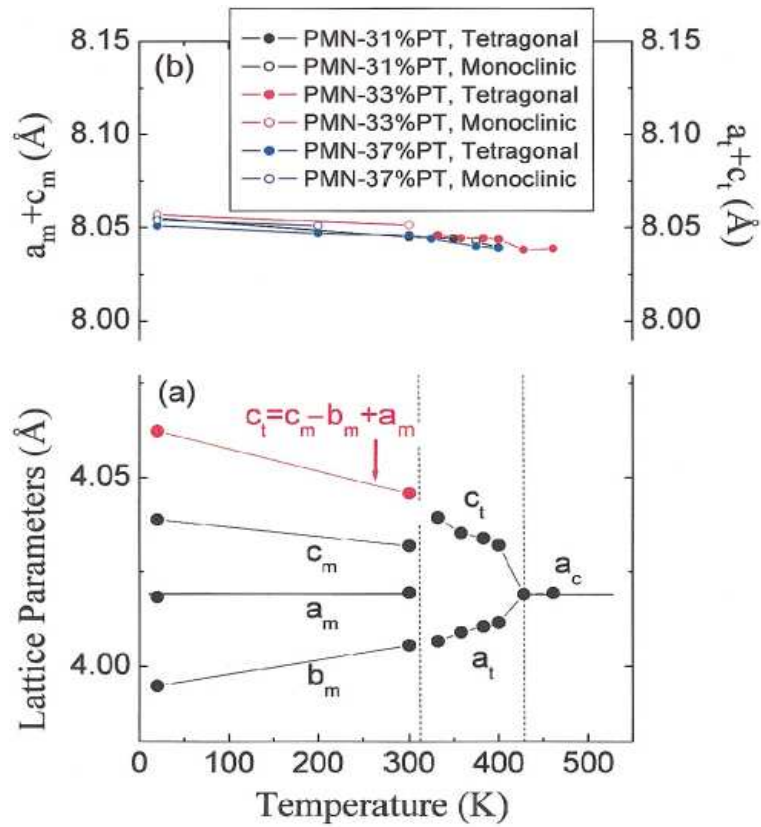


Figure 1.7 (a) Temperature dependent lattice parameters for PMN-0.33PT ceramics. (b) Temperature dependence of the general invariance condition of $a_m + c_m = a_t + c_t$ [20]. Reprinted with permission from [20]. Copyright [2003], American Physical Society.

crystal lattice parameters of the tetragonal (or rhombohedral) and monoclinic M_C (or M_A/M_B) phases with changes in electric field and applied stress [19,20]. Figure 1.7 shows the temperature dependence of the lattice parameters for PMN-xPT ceramics. Two interesting crystallographic relationships between lattice parameters can be observed in this figure at the $T \rightarrow M_C$ transition, which are

$$a_m + c_m = a_t + c_t, \quad 1.8 (a)$$

$$b_m = a_t; \quad 1.8 (b)$$

where (a_m, b_m, c_m) and (a_t, c_t) are the lattice parameters of the M_C and T phases. This figure shows that the changes in the lattice parameters are entirely invariant with the general geometric conditions of (1.8). These general conditions are geometrically similar to those for twinning, following the classic Wechsler-Lieberman-Read (WZR) [35] theory of martensite: However, the conditions in (1.8) are reduced in length scale and applied to those of the lattice parameters, rather than twin boundaries. The concept is illustrated in Figure 1.8. The underlying assumption is that the twinning of the T phase is conformally reduced to near atomic dimensions.

This is the alternate “ferroelectric adaptive phase” theory for monoclinic phases, originally proposed by Viehland [19] and subsequently expanded by Jin, and Wang [20, 36]. Following the adaptive phase model, the monoclinic phases consist of miniaturized T or R microdomains (nanotwins), whose apparent lattice parameters are determined by accommodation of misfit stress and electric field. This adaptive phase is a structurally inhomogeneous on a microscale ($\sim 10\text{nm}$), but apparently homogeneous on a macroscale. Such an adaptive phase is formed by plates containing twin-related tetragonal microdomains, and observed as a homogeneous monoclinic phase by diffraction measurements: resolution of the T or R phases from the M_C or M_A ones is limited by the optics of diffractions. In order to accommodate the elastic stress and avoid misfits along the domain boundaries, particular relationships between lattice parameters of tetragonal and monoclinic M_C phase must be satisfied, given in (1.8) above. In this case, the monoclinic angle (β) has been shown by Wang [36] to be

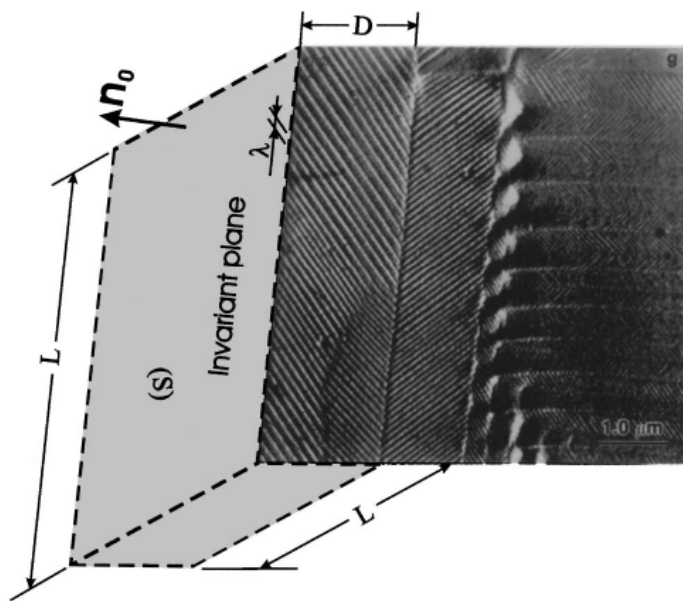


Figure 1.8 Dark field TEM image of stress accommodating polydomain structure in CuAu alloy [37]. The structure of the adaptive phase has the same morphology but is conformally miniaturized to reach nano- or subnanoscale. Then white and black stripes become microdomains that are “invisible” to the usual diffraction measurement and the macroplates become macrodomains that are perceived as domains of the “homogeneous” monoclinic phase (adaptive phase). Reprinted with permission from [37]. Copyright [1967], Wiley-VCH Verlag GmbH & Co. KGaA.

$$\beta = 90^\circ + 2A\omega(1-\omega)\left(\tan^{-1}\frac{c_t}{a_t} - 45^\circ\right), \quad 1.8 (c)$$

where $\omega = \frac{c_m - b_m}{a_m + c_m - 2b_m}$, is the volume fractions of one of two variants and A is a fitting constant, that is close to 1. Furthermore, we note that the O phase is a limiting case of M_C , where $\omega = 1/2$. A similar approach to conformal miniaturized of R domains would yield the monoclinic M_A/M_B phase, as discussed by these authors [36].

This adaptive model can successfully explain the observed characteristic transformations in the lattice parameters with temperature. It also can explain changes in the lattice parameters with E or stress (σ). In this case, the extreme piezoelectricity of PMN-xPT and PZN-xPT can be attributed to changes in the distribution of microdomains. These changes with E and σ are restricted to occur along special geometrically invariant conditions that achieve elastic accommodation. Experimentally, changes in lattice parameters with E and σ have been shown to follow these restrictions.

It is important to not that the adaptive phase model is based on an inherently structurally inhomogeneous state. This is in sharp contrast to the inherently homogeneous one of the polarization rotation theory.

1.2.6 Polar-nano regions and lattice dynamics

The dielectric properties of PMN and PZN present a broad and frequency-dispersive maximum of permittivity around $T=T_{max}$. Each compound is characterized by quenched chemical disorder on the perovskite B site which is occupied by Mg^{2+} (or Zn^{2+}) and Nb^{5+} cations. It is well known that the mixed valence and compositional fluctuations on B sites with disordered Mg^{2+} and Nb^{5+} occupations inherent to both PMN and PZN is required for the dielectric relaxation and diffuse transition in a temperature range around T_{max} . However, PMN and PZN are surprisingly different. Whereas PZN is a ferroelectric that transforms from a cubic to a rhombohedral phase at 410K, PMN remains, on average, cubic below T_{max} down to 5K. In 1983, Burns and Dacol [38] proposed the polar-nano-regions (PNR's) from measurements of the optic index of refraction in different relaxor systems, including PMN

and PZN. The most remarkable aspect of their finding was that the PNR's start forming at a temperature T_d (or Burns temperature), that is several hundred degrees higher than T_{max} . Variations of the concentrations in Mg and Nb ions in different polar micro-regions give rise to different local Curie temperatures. Polar Regions with a critical size of about 10nm, which can be temperature dependent, were suggested to be present in the paraelectric matrix and considered as nuclei of the ferroelectric phase.

Neutron inelastic scattering measurements on PMN [39] and PZN [40] in the cubic phase have revealed a heavily damped TO mode between the Burns temperature T_d (620K), below which polar nanoregions (PNRs) form [38], and a lower critical temperature ~ 213 K, below which a remnant polarization can be sustained in the FC condition [41]. This heavily damped TO soft mode occurs only for reduced wave vectors $q \leq 0.2 \text{ \AA}^{-1}$ [42]– this is the so-called ‘waterfall’ effect in which long-wavelength TO modes exhibit an anomalous q -dependent damping between T_d and T_C for wave vectors near the zone center. This provides direct evidence of the correlation between the PNR's and the anomalous phonon damping. However, recent high-temperature neutron scattering measurements on PMN [43, 44] and PMN-0.60PT [45] above the Burns temperature T_d show the presence of weak diffuse scattering elongated along the longitudinal direction, which has been interpreted in terms of a short-range ordering (SRO) of B-site cations. For PMN-0.60PT the intensity of the diffuse scattering does not vary below T_d indicating that B-site cation SRO is the dominate source of diffuse scattering: i.e., polar nanoregions do not form on cooling. Whereas, for PMN and PZN another diffuse component develops that forms rods elongated along the [1-10] directions and is highly temperature dependent. The intensity of these diffuse scattering increases on cooling below T_d , changing notably in the vicinity of T_f [46, 47], indicating that both SRO and PNR formation make important contributions.

1.3. Ferromagnetic materials

1.3.1 Ferromagnetism

Ferromagnetic materials are characterized by the spontaneous alignment of magnetic moments below a critical temperature T_C , in the absence of any external magnetic field. This results in a spontaneous magnetization $M_s(T)$. A ferromagnetic body does not have to have a net magnetization: the magnetization can average to zero, if the body has not been previously exposed to an applied magnetic field. In fact, ferromagnetic materials are divided into regions of limited spatial extent called magnetic domains. Each domain has a net spontaneous magnetization; however, these magnetic domains can be randomly oriented with respect to each other among on various symmetry equivalent directions. This minimizes the total magnetic energy, resulting in an average magnetization equal to zero. However, upon application of magnetic field, the magnetic domains can be reoriented along the direction of the magnetic field: this gives rise to a magnetic hysteresis loop, as illustrated in Figure 1.9 (a). The important parameters such as coercive magnetic field (H_c), remnant magnetization (M_r) are indicated in this figure.

Figure 1.9 (b) shows a schematic of the temperature dependence of the reciprocal susceptibility of ferromagnetic materials [48]. The reciprocal susceptibility varies linearly with decreasing temperature, becoming zero at T_C . At high temperatures above T_C , the temperature dependence of the reciprocal susceptibility follows a linear Curie-Weiss law, analogous to that of ferroelectric, given as

$$\frac{1}{\chi} = (T - \theta_p) / \xi; \quad 1.10$$

where ξ is the Curie constant, and θ_p is the paramagnetic Curie temperature which is equal to T_C in Figure 1.9 (b). Experimentally, the Curie-Weiss law is not exactly observed in the vicinity of T_C . Generally, θ_p is slightly larger than T_C . The difference $(\theta_p - T_C)$ depends on the material, and is believed to be associated with the persistence of a short range magnetic order at temperatures slightly above T_C . Below this temperature, a parallel

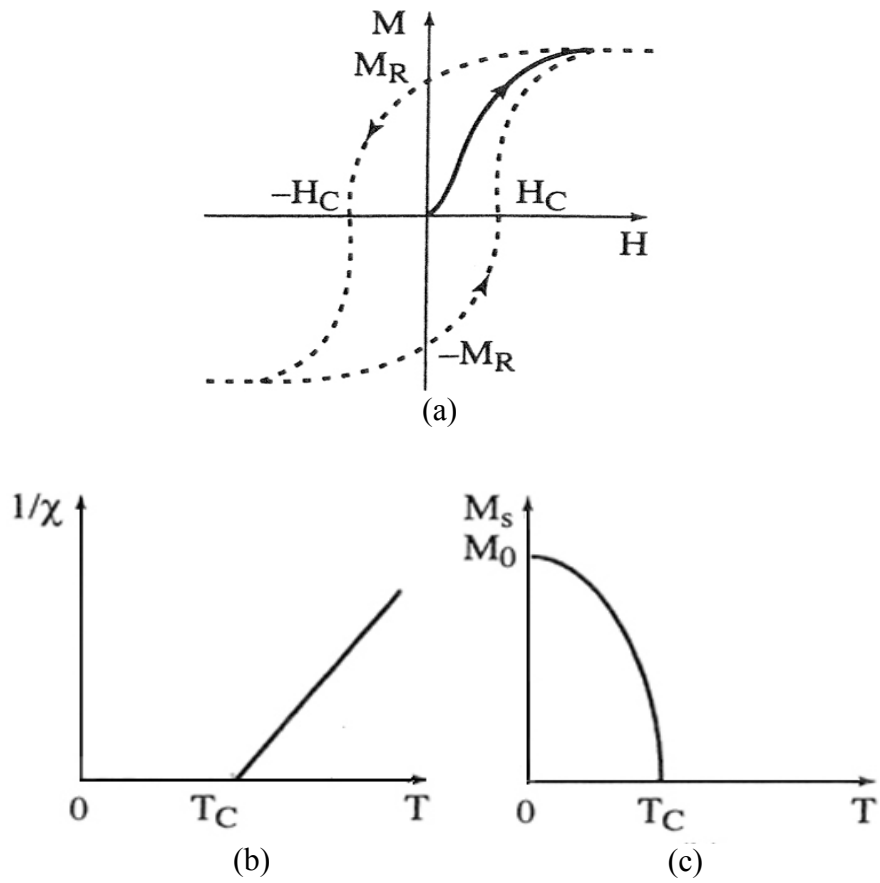


Figure 1.9 Sketch of (a) ferromagnetic hysteresis loop, illustrating the magnetic domain switching under an external magnetic field; (b) temperature dependence of reciprocal susceptibility; (c) temperature dependence of spontaneous magnetizations.

arrangement of magnetic moments results from interactions between neighboring spins. Positive exchange interactions overcome thermal agitation, and a spontaneous magnetization appears in the absence of an applied magnetic field on cooling, as show in Figure 1.9(c). This spontaneous magnetization reaches its maximum value M_0 at 0K, when all individual magnetic moments are perfectly aligned.

1.3.2 Magnetostriction and its microscopic origin

In a magnetic material, the interatomic distances can vary with the intensity and the orientation of the magnetization. Magnetostriction has it origin in a coupling between the direction of the spin moment of an atom and the orientation of its anisotropically shaped electron cloud: i.e. the spin-orbit coupling [49]. This effect can be explained by the very simple model developed by Néel [50] within the framework of localized electron ferromagnetism. Analytically, the magnetostriction of magnetic materials can be obtained by minimizing the sum of the elastic energy (E_{elas}) and the magnetoelastic coupling energy (E_{mel}) with respect to an applied magnetic field.

For a crystal with cubic symmetry, the magnetostriction can then be derived as:

$$\lambda = \frac{\partial l}{l} = \frac{1}{3} \lambda^{\alpha,0} + \lambda^{\gamma,2} \left(\frac{2}{3} (\alpha_3^2 - \frac{\alpha_1^2 + \alpha_2^2}{2}) (\beta_3^2 - \frac{\beta_1^2 + \beta_2^2}{2}) + \frac{1}{2} (\alpha_1^2 - \alpha_2^2) (\beta_1^2 - \beta_2^2) \right) ; \quad (1.11)$$

$$+ 2\lambda^{\varepsilon,2} (\alpha_2 \alpha_3 \beta_2 \beta_3 + \alpha_3 \alpha_1 \beta_3 \beta_1 + \alpha_1 \alpha_2 \beta_1 \beta_2)$$

where $\lambda^{\alpha,0} = -b^\alpha / c^\alpha$, $\lambda^{\gamma,2} = -b^{\gamma,2} / c^\gamma$, and $\lambda^{\varepsilon,2} = -b^{\varepsilon,2} / c^\varepsilon$ are the first order magnetostriction coefficients of a material with cubic symmetry; $b^\alpha, b^{\gamma,2}, b^{\varepsilon,2}$ are the anisotropic magnetoelastic coupling coefficients; c^α, c^γ are elastic stiffness coefficients with $c^\alpha = c_{11} + 2c_{12}$, $c^\gamma = c_{11} - c_{22}$, $c^\varepsilon = 2c_{44}$; and the α_i are the direction cosines of the magnetization, and the β_i coefficients are the direction cosines of the relative expansion ($\partial l/l$). Higher order terms are generally small enough to be neglected. Following the relationships between the anisotropic magnetoelastic coefficients and elasticity coefficients above, the saturation magnetostriction along [100] and [111] can be written as:

$$\lambda_{[100]} = -\frac{2b_1}{3(c_{11} - c_{22})}, \quad 1.12 \text{ (a)}$$

$$\lambda_{[111]} = -\frac{b_2}{3c_{44}}; \quad 1.12 \text{ (b)}$$

where $b_1 = -b^{\gamma,2}$, and $b_2 = -b^{\epsilon,2}$. Thus, it is possible to enhance magnetostriction by increasing b_1 (or b_2) and or decreasing $c_{11} - c_{22}$ (or c_{44}).

A more detailed discussion of magnetoelastic effects and magnetoelastic energies can be found in a book by É. du Trémolet de Lacheisserie [48].

1.3.3 High magnetostriction in Fe-xGa alloys

Mechanically strong and malleable galfenol alloys (Fe-xat.%Ga) have a large magnetostriction of $3\lambda_{<100>}/2=400\text{ppm}$ at low saturation fields [51, 52]. The saturation magnetostriction λ_{100} is over tenfold that of pure Fe (33ppm at room temperature [53]), yet the value of λ_{111} remains nearly unchanged on introduction of Ga. Compared to other high strain active materials, (i.e. Terfenol-D, PZT, and PMN-PT), Fe-xat.%Ga alloys can be machined and welded, allowing active structures to be fabricated. Large magnetostriction and a high relative permeability, coupled with robust mechanical properties make Fe-xat.%Ga attractive for potential applications as magneto-acoustic sensors, actuators and transducers.

In Fe-xat.%Ga alloys, the addition of Ga atoms into the b.c.c. α -Fe phase also results in diversity of crystal phases and structural inhomogeneity, which is likely the source of its unusual magneto-elastic properties. A positionally/chemically ordered DO_3 phase exists near a composition range of $15 < x < 27$ in the Fe-Ga phase diagram [54], where the magneto-elastic properties and phase stability can be notably altered by thermal histories. Figures 1.10 (a) and (b) show the Fe-Ga binary phase equilibrium diagram reported by Okamoto [55], and a modified metastable equilibrium phase reported by Ikeda [54], respectively. Figure 1.10 (c) illustrates different crystal structures for the various phases in these diagrams, including the pure bcc, A2, B2, DO_3 (body-centered cubic (bcc) Fe_3Ga), $L1_2$ (face-centered cubic (fcc) Fe_3Ga) and DO_{19} . In the equilibrium state, the A2 phase coexists with a $L1_2$ one in a two phase region near $15 < x < 27$. A DO_3 phase lies above the stability

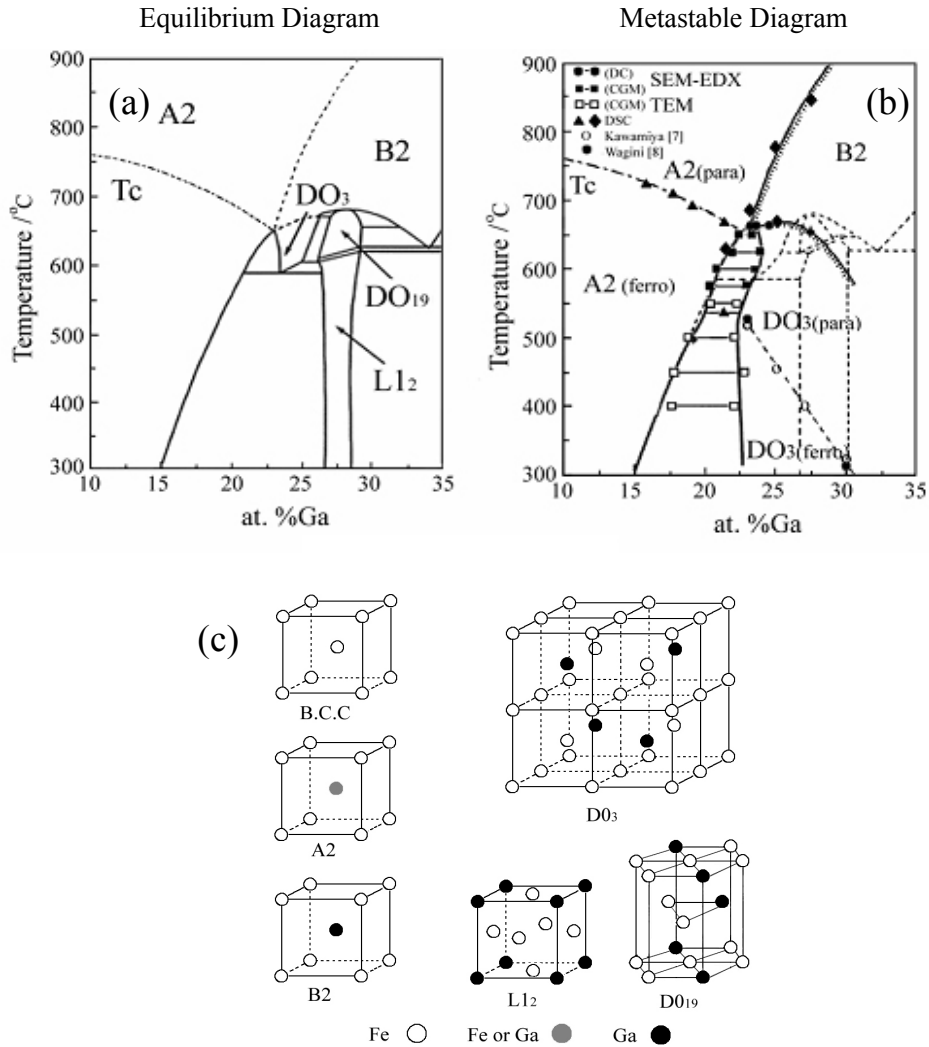


Figure 1.10 (a) a Fe-Ga binary phase equilibrium diagram reported by H. Okamoto; (b) a modified metastable equilibrium phase diagram by O. Ikeda [54]; (c) crystal structures of A₂, B₂, DO₃, DO₁₉, and L₁₂ (Reprinted with permission from [54]. Copyright [2002], Elsevier Ltd.).

range of the A2+L1₂ two phase region. However, in the metastable state, the precipitation of the thermally stable L1₂ phase is so slow that a metastable DO₃ phase can develop. This is the case even if the crystals are annealed in the A2+L1₂ two phase field of the equilibrium state, where the metastable DO₃ phase competes with the equilibrium L1₂ phase.

The significant enhancement of magnetostriction of Fe by alloying with Ga is not due to a uniform magnetization change, as Ga atoms are not magnetic. Previous magnetostriction (λ_{100}) investigations of Fe-xGa alloys have revealed the existence of two anomalous peaks with increasing of x in the quenched state near x=19 and x=27, as shown in Figure 1.11 (a). The first peak at x≈19, has been attributed to an increase in the magneto-elastic coupling, b_1 , with the formation of short-range ordering (SRO) of Ga pairs along the [100] of the bcc α -Fe crystal structure [56]. The presence of clusters of Ga atoms results in both elastic and magneto-elastic defects on alloying. The second peak at x≈27 is believed to be due to a softening of the shear modulus, $c' = (c_{11} - c_{12})/2$ [57,58], as illustrated in Figure 1.11 (b). The shear elastic constant c_{44} is nearly independent of the Ga content x; whereas the shear elastic constant $(c_{11} - c_{12})/2$ decreases near linearly with increasing x, extrapolating to zero near x=26. Wuttig *et al.*[58] conjectured that the magnetostriction enhancement by Ga substitution results from premartensitic deformations in the vicinity of SRO Ga clusters. Subsequently, magnetic force microscopy (MFM) studies of Fe-20at.%Ga [59] have revealed the presence of miniaturized magnetic domains of size ≤ 100 nm, indicating that a structurally inhomogeneous nano-domain states (i.e. SRO clusters) may induce magnetic clusters.

1.3.4 Structurally heterogeneous model: a nano-dispersion of DO₃ with confined tetragonal displacive transformation

Few nanometer large (<2nm) DO₃ phase structures have been identified in the A2 matrix of highly magnetostrictive Fe-19at.%Ga alloys by high resolution transmission electron microscopy (HRTEM) [60], as shown in Figure 1.12. In addition, it has been found that these nanostructures have a high density of {100} line defects with a Buerger's vector of $\frac{1}{2}a_{bcc} \langle 100 \rangle$. The presence of {100} line defects inside the nano-precipitate can be attributed to the appearance of vacancy loops to compensate the Ga enrichment of the Fe₃Ga

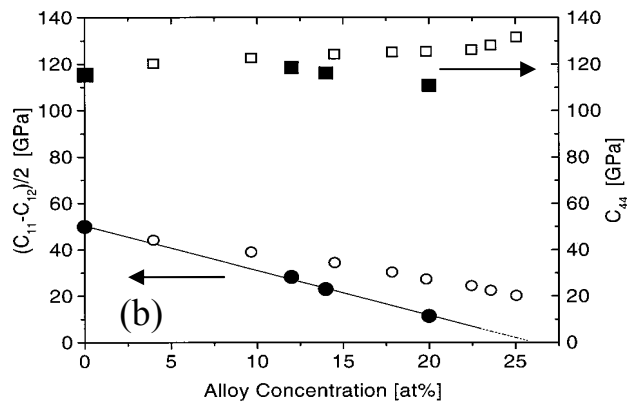
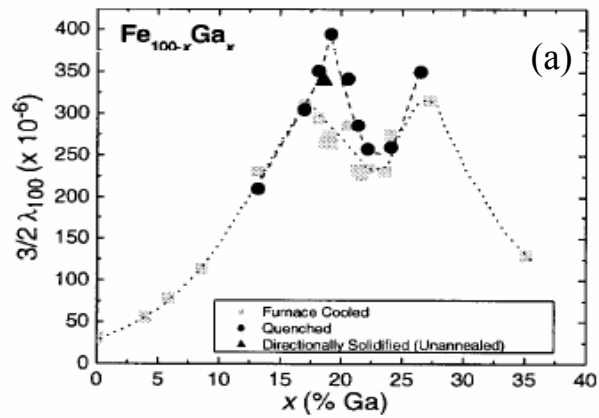


Figure 1.11 (a) Saturation magnetostriction measured at room temperature for Fe-xGa alloys [57] (Reprinted with permission from [57]. Copyright [2003], American Institute of Physics); (b) shear elastic constant $(c_{11}-c_{12})/2$ (circle) and c_{44} (square) of Fe-xGa (solid symbols) and Fe-xAl (open symbols) [58] (Reprinted with permission from [58]. Copyright [2002], American Institute of Physics).

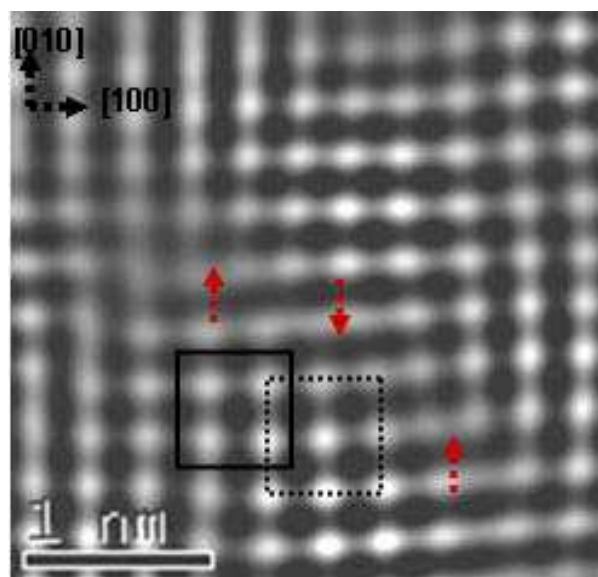


Figure 1.12 Inverse Fourier transform of the $\{010\}$ reflections of Fe-19at.%Ga by HRTEM, which showing that the D0_3 nanostructure contains many line defects along the $\{100\}$ [60 (Reprinted with permission from [60]. Copyright [2008], American Physical Society).

of DO₃ in comparison to the nominal 19at.%Ga content of the Galfenol solid solution. The appearance of vacancy loops would lift the coherency of the DO₃ phase precipitates and reduce strains, possibly providing the thermodynamics conditions required for DO₃ phase precipitates with this Fe-Ga compositional range.

To explain these results, Khachaturyan and Viehland have proposed a structural heterogamous model for Fe-Ga and similar magnetic alloys [61]. This heterogeneous model conjectures that the Fe-xGa (15<x<27) undergoes a C→T displacive transformation on cooling from a bcc-based DO₃ structure to a face-centered tetragonal (fct) based DO₂₂ one, which is close to an equilibrium fcc-based L1₂ ordered phase. Figure 1.13 shows the orientation relations between the DO₃, DO₂₂ and L1₂ lattice cells in Fe-xGa alloy. Part (a) shows the unit cell of the DO₃ structure, which is based on eight ordered bcc unit cells with Ga-Ga atom pairing along the <110>. Part (b) shows the unit cell of the DO₂₂ structure after application of the homogeneous Bain strain, which is exactly equivalent to the DO₃ structure before the displacive transformation: this Bain strain transforms the underlying bcc host lattice of the DO₃ to a new fct-based DO₂₂ without atomic interchanges between these atomic sites. This new fct DO₂₂ has a *c*-axis along the [001], and *a*- and *b*- axes along the [110] and $\bar{1}\bar{1}0$. Parts (c) and (d) show the unit cell of the fcc L1₂ structure and a modified unit cell after translation by (1/2, 1/2, 0) along the [110] in the L1₂ unit cell, respectively. This new unit cell is designated as a “fcc DO₂₂”, because it has exactly half the unit cell of the fct DO₂₂ structure. It is important to note that an appropriate compression applied along the [110], together with a uniform expansion along the $\bar{1}\bar{1}0$ and [001], would convert the fct cell of DO₂₂ into the fcc cell of L1₂.

The L1₂ and DO₃ phases of Fe-Ga alloys both have the Fe₃Ga stoichiometry. The equilibrium phase is the L1₂ phase, rather than the DO₃ phase; whereas, in the metastable state, nanosized DO₃ precipitates decompose out of the A2 matrix (as shown in Figure 1.12 above). Further equilibration of the DO₃ precipitates leads to a DO₃→L1₂ transformation. However, the DO₃→L1₂ transition, unlike the bcc→DO₃ or fcc→L1₂ ones, can not be completed by atomic exchanges between sites of the same underlying bcc or fcc lattice.

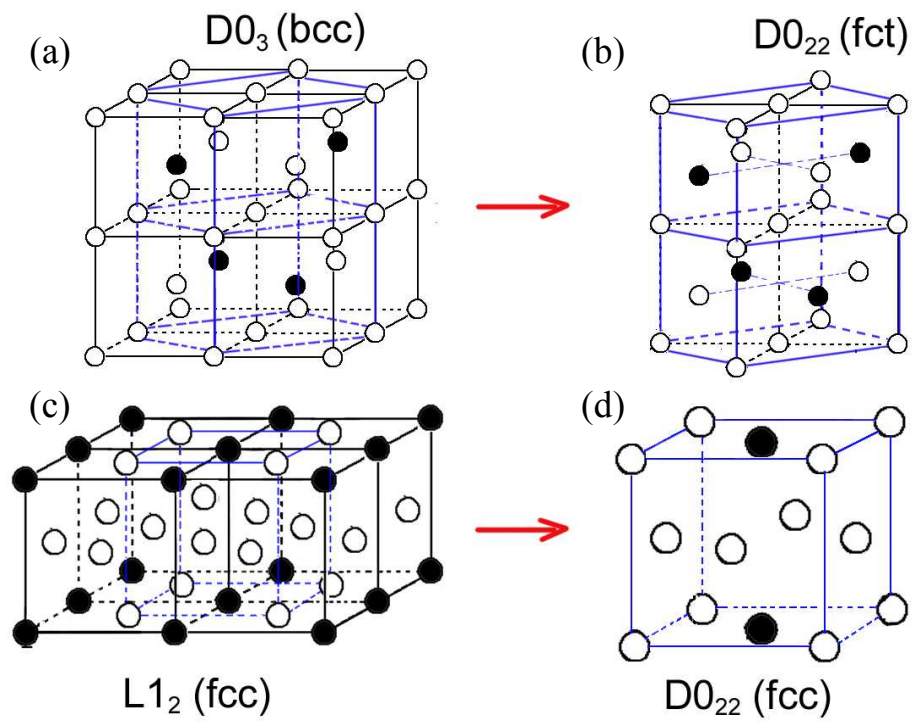


Figure 1.13 the orientation relations between bcc-based DO_3 (a), fct-based DO_{22} (b), fcc-based $L1_2$ (c), and fcc $1/2DO_{22}$ (d) lattice cells, which visually showing a C→T displacive transformation from DO_3 to $L1_2$ (or DO_{22}).

Therefore, an intermediate step of $\text{DO}_3 \rightarrow \text{DO}_{22}$ (fct) is necessary for the formation of an equilibrium fcc L_{12} from the bcc DO_3 structures, can be seen in Figures 1.13 (c) and (d). Since the kinetics of the precipitation of L_{12} is extremely slow, the transition DO_{22} (fct) \rightarrow L_{12} may (in annealed state) or may not (in quenched state) occur on cooling depending on thermal treatments.

Khachatryan and Viehland conjectured that the $\text{DO}_3 \rightarrow \text{DO}_{22}$ phase transformation is martensitic. In this case, the DO_{22} structure is tetragonally distorted from the cubic DO_3 one. Although the tetragonality of DO_{22} is unknown, the maximum extrinsic magnetostriction was estimated by considering DO_3 and L_{12} as the initial and terminal phases in the $\text{DO}_3 \rightarrow \text{L}_{12}$ transformational sequence, respectively, given as

$$a_{L_{12}} = \frac{1}{2} a_{D_{03}} (1 + \varepsilon_c), \quad 1.13 \text{ (a)}$$

$$a_{L_{12}} = \frac{1}{\sqrt{2}} a_{D_{03}} (1 + \varepsilon_a); \quad 1.13 \text{ (b)}$$

where ε_a and ε_c are the Bain strain components for the $\text{DO}_3 \rightarrow \text{L}_{12}$ transformation [61] and $a_{L_{12}} = 3.678 \text{ \AA}$, $a_{D_{03}} = 5.100 \text{ \AA}$ [63]. Therefore, the estimations of the extrinsic magnetostriction are

$$\varepsilon_c \approx 0.265, \quad \varepsilon_a \approx -0.105. \quad 1.13 \text{ (c)}$$

In reality, the tetragonality distortion may be commensurate with Bain strain in the $\text{DO}_3 \rightarrow \text{L}_{12}$ transformation, or may be significantly less. Such a large transformational strain would raise the elastic energy too much in the A2 matrix, preventing the growth of large DO_{22} precipitates. Thus, only SRO tetragonal DO_{22} nanoclusters would form within the A2 matrix. This is one of the main predictions of the Khachatryan-Viehland theory: i.e., the “ DO_3 clusters” in the A2 matrix are in fact tetragonally distorted with a large c/a ratio of ≈ 1.1 – 1.2 . However, this prediction has yet to be experimentally validated. Giant magnetostriction would then result from a redistribution of tetragonal nanotwins under applied magnetic field and /or stress.

CHAPTER 2 EXPERIMENT PROCEDURES

2.1. Sample preparation

2.1.1 PMN-PT single crystals

PMN-PT single crystals were grown by top-seeded modified Bridgman techniques, using a sealed platinum crucible [63]. Experimental crystals were obtained commercially from HC Materials (Urbana, IL) and Professor Prof. Haosu Luo's group, (Shanghai Institute of Ceramics, Chinese Academy of Sciences). Single crystals of PMN-xPT with different compositions ($x=0.38, 0.35, 0.32, 0.30, 0.28, 0.27, 0.24, 0.15$) across the MPB were prepared. In order to investigate the effect of electric field along different crystallographic directions on physical properties and crystal structures, the crystals were cut along different orientations, including (001), (110), (111) and (211). Gold electrodes were deposited by sputtering (SPI-Module Sputter Coater). The correct compositions of experimental specimens were double-checked by measuring T_{max} through the temperature dependent dielectric constant by a multifrequency LCR meter (HP 4284A). For dielectric, polarization hysteresis loop and strain measurements, plate specimens were prepared with the size $3 \times 3 \times 0.5 \text{ mm}^3$. For x-ray and neutron scattering, two kinds of cubes were prepared along the pseudocubic (001)/(100)/(010) and (110)/($\bar{1}\bar{1}\bar{1}$)/($\bar{1}\bar{1}\bar{2}$) planes, and were polished to $0.25 \mu\text{m}$.

2.1.2 Fe-xGa alloys

The Fe-xat%Ga ($x=12, 14, 19, 20, 23, 25, 30$) samples used in this investigation were grown at Ames Lab by the Bridgman method [64]. Two kinds of oriented samples were used, (100)/(010)/(001) and (110)/($1\bar{1}\bar{0}$)/(001). Different thermal treatments were applied to these samples, including as-grown ($10^\circ\text{C}/\text{min}$. cooling), furnace cooled (thermally re-processing as $10^\circ\text{C}/\text{min}$. cooling), slow cooled ($2^\circ\text{C}/\text{min}$. cooling), and quenching in ice water. Except for the as-grown condition, the other thermal treatments use the same heating rate ($10^\circ\text{C}/\text{min}$.), annealing temperature (1100°C) and time (2 hours) under an argon atmosphere. Measurements of the magnetostriction were performed on plate-shaped samples ((100)/(010)/(001), $10 \times 10 \times 1 \text{ mm}^3$) glued with Micro-Measurement CEA-06-062UT-350

dual-stain gages. For x-ray diffraction, the sample was polished using a 0.25 μm diamond suspension. In order to study the texture and grain morphology, we also polished and then etched the (110)/(1 $\bar{1}$ 0)/(001) oriented Fe-xat%Ga (x=12, 20, 25) using 5% nital (5 vol.% nitric acid and 95 vol.% methyl alcohol) for 3 minutes, in both the quenched and slow cooled states.

TEM specimens ($1.5 \times 1 \times 0.5 \text{mm}^3$, (100/(010)/(001)) were cut from one Fe-19at.%Ga plate, and then clamped and glued using a titanium alloy sample holder with a diameter of 3mm. Standard techniques of sample preparation were performed on these specimens, including grinding and polishing down to 60-80 μm thickness, dimpling a tiny hole and argon ion-beam thinning (Model 1010 ion mill, E.A. Fischione Instrument Inc., PA, USA). Ion-beam thinning was carried out on both sides of the sample at an inclination angle of 8° of the ion beam with respect to the sample. Conventional dark-field electron microimages and selected area electron diffraction (SAED) patterns were obtained using a high resolution FEI TITANTM 300 operating at 200kV. This instrument is located in the Nanoscale Characterization and Fabrication Laboratory at Virginia Tech. Care was taken to orient the [001] zone axis of the specimen parallel to the incident electron beam before imaging.

2.2. Structural Analysis Tools

2.2.1 X-ray diffraction

The XRD studies were performed using a Philips MPD high-resolution system equipped with a two bounce hybrid monochromator, an open 3-circle Eulerian cradle, and a doomed hot-stage, as shown in Figure 2-2(a). A Ge (220)-cut crystal was used as an analyzer, which had an angular resolution of 0.0068°. The x-ray wavelength was that of $\text{Cu}_{K\alpha} = 1.5406 \text{\AA}$, and the x-ray generator was operated at 45kV and 40mA. The penetration depth in the samples was on the order of 10 microns for PMN-xPT crystals and about 3 microns for Fe-xGa alloys.

For (001)-oriented PMN-xPT crystals and Fe-xGa alloys, we performed mesh scans around the (002) and (200) Bragg reflections in the (H,0,L) zone, defined by the [001] and [100] vectors; and about the (220) reflection in the scattering (H,H,L) zone, defined by the

[110] and [001] vectors. For (110)-oriented crystals, we performed mesh scans around the (002) reflection in the (H,H,L), defined by the [001] and [110] vectors; the (220) and $(2\bar{2}0)$ reflections in the scattering zone defined by the [110] and $[\bar{1}\bar{1}0]$ vectors; and the (200) in the (H0L) zone, defined by the [100] and [001] vectors. Two scan techniques were performed: (i) linear $2\theta-\omega$ (single scan) to measure the lattice parameters; and (ii) $\omega/2\theta-\omega$ mesh scans (area scan) to determine the crystal symmetry and domain distribution.

Figure 2.1 (a) shows a sketch of high resolution x-ray diffractometer. Figure 2.1 (b) shows the schematic of single scans and area scans in reciprocal space. The ω scan is in the direction of an arc centered on the origin. The scan subtends an angle equal to the scan range at the origin; where the 2θ scan appears as an arc along the Ewald sphere circumference. The scan subtends an angle equal to the scan range at the center of the Ewald sphere, where the $2\theta-\omega$ or $\omega-2\theta$ scan is a straight line pointing away from the origin of reciprocal space. Area scans are referred to as 2-axes measurements within the X-pert Data Collector. Generally, $\omega/2\theta-\omega$ was chosen to perform the mesh scans around the diffraction zone.

For PMN-PT crystals, each measurement cycle was begun by heating up to 550K to depole the crystal, and measurements subsequently taken on cooling. In this study we fixed the reciprocal lattice unit (or 1 rlu) $a^*=2\pi/a=1.560\text{\AA}^{-1}$. All mesh scans shown in this study were plotted in reference to this reciprocal unit. For Fe-Ga alloys, we fixed the reciprocal lattice unit (or 1 rlu) $a^*=2\pi/a=2.160\text{\AA}^{-1}$, and all mesh scans shown in this study were plotted in reference to this reciprocal unit.

2.2.2 Neutron Triple Axis Spectrometer

The laws of momentum and energy conservation governing all diffraction and scattering experiments are well known:

$$Q = k_f - k_i, \quad (3-1)$$

$$h\omega = E_i - E_f, \quad (3-2)$$

where the first equation represents the momentum conservation and the second equation represents the energy conservation. In these equations, the wave-vector magnitude is $k=2\pi/\lambda$,

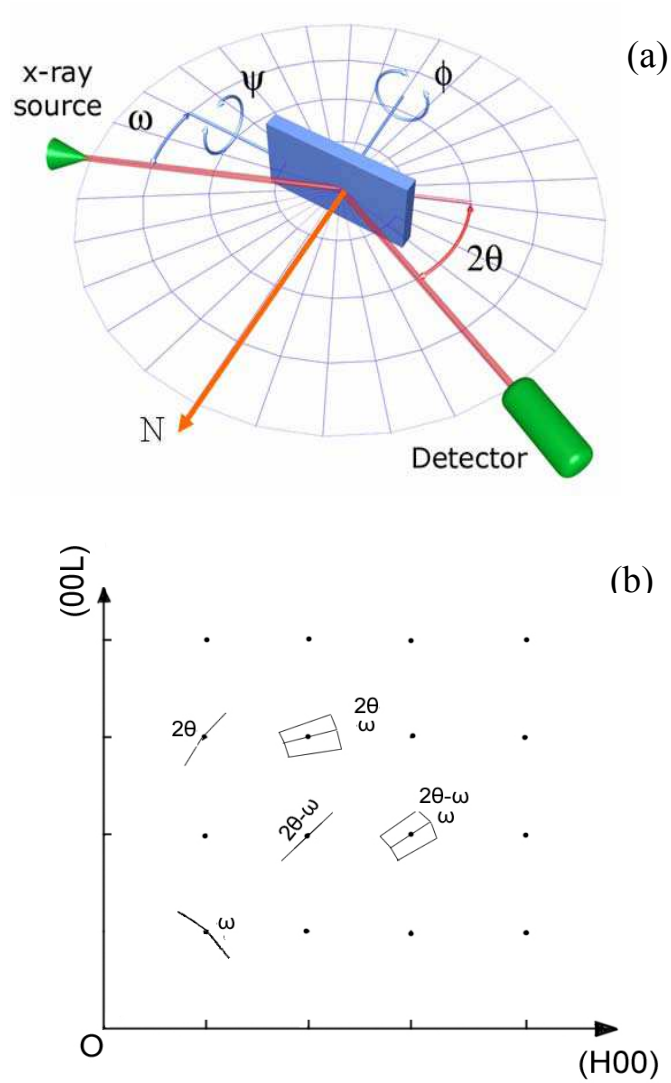


Figure 2.1 Schematic illustrations of (a) Philips MPD high resolution x-ray diffractometer and (b) single scans and area scans in reciprocal (HOL) zone.

where λ is the neutron wavelength. The subscript i refers to the incident beam and the f refers to the final beam or diffracted beam. The energy transferred to the sample is $h\omega$. In any scattering experiments, one always measures the properties of the incident and final beams and then calculates the momentum or energy transferred to samples. In my investigation, two kinds of neutron scattering were performed: elastic and inelastic. Both types of scattering were performed on the neutron triple axis spectrometers designated as BT-7 and BT-9, at the Neutron Research Center of the National Institute of Science and Technology (NIST).

The triple axis spectrometer is the most versatile and useful instrument both for elastic and inelastic scattering studies. The triple axis (or three axes) corresponds to the axes of rotation of the monochromator crystal, the sample, and the analyzer crystal. The monochromator defines the direction and magnitude of the momentum of the incident beam. The neutron diffracted by the monochromator hits the sample. These neutrons are then scattered from the sample following Bragg's law, and reflected by the analyzer, which performs a similar function for the diffracted beam as the monochromator. Since the scattering plane is horizontal, the scattering observed at the detector is a function of only three variables: the energy transfer ($h\omega$) and the two components (k_i , k_f) of momentum transfer in the plane.

Elastic scattering

In the elastic scattering from a crystalline solid, (i.e., $|k_i|=|k_f|=k$), the diffraction and scattering measurements have to follow Bragg's law:

$$Q = G = k_f - k_i \quad (3-3)$$

$$|G| = 2k \sin \theta_s \quad (3-4)$$

where \mathbf{G} is the a reciprocal lattice vector and $2\theta_s$ is the angel between the incident beam and diffracted beam. Eq. 3-4 can also be written in the more familiar form

$$\lambda = 2d \sin \theta_s$$

by noting that the magnitude of the reciprocal lattice is $|\mathbf{G}| = 2\pi/d$, where d refers to the interplanar spacing. Neutron elastic scattering and diffuse scattering on Fe-xGa alloys were performed on BT-7 and BT-9 at NIST. Measurements were made using a fixed incident

neutron energy $E_i=14.7$ meV, obtained from the (002) reflection of a highly oriented pyrolytic graphite (HOPG) monochromator. Horizontal beam collimations of $10^\circ-44^\circ-20^\circ-40^\circ$ (for BT9) and $10^\circ-50^\circ-20^\circ-40^\circ$ (for BT7) were used for neutron elastic scattering, and of open- $50^\circ-60^\circ-180^\circ$ for both of BT-7 and BT-9 for neutron diffuse scattering. On BT-9 we used the (004) reflection of a perfect Ge crystal as analyzer to achieve unusually fine wavevector-resolution near the (400) Bragg peak, which provides a near perfect matching of the sample and analyzer d-spacing. Close to the (200) Bragg peak, the radial-resolution (i.e. the resolution measured along the wave vector direction) is about 0.0012\AA^{-1} ($\Delta q/q \approx 2 \times 10^{-4}$). Line scans through the (400) Bragg peak were performed while cooling from 800°C to room temperature in a high temperature vacuum furnace.

Inelastic scattering

For inelastic scattering, $|\mathbf{k}_i|$ is not equal to $|\mathbf{k}_f|$. This is because part of the energy has to be transferred to the sample. There are two cases, where k_i is fixed and k_f varies, or vice versa, where k_f is fixed and k_i varies. If $|\mathbf{k}_i| > |\mathbf{k}_f|$, then $h\omega > 0$. In this case, energy is transferred to the sample from the incident neutron and an excitation is created. If $|\mathbf{k}_i| < |\mathbf{k}_f|$, then $h\omega < 0$. In this case, the sample has to give up a quantum of energy to the neutron beam and an excitation is annihilated.

In experiments, one typically holds one wave vector constant while varying the other. For a single crystal sample, the energies depend only on the relative momentum $h\mathbf{q}$ defined within a Brillouin zone. Hence, it is convenient to refer the momentum transfer to the nearest reciprocal lattice vector, i.e.,

$$\mathbf{Q} = \mathbf{G} + \mathbf{q}, \quad (3-5)$$

There are two types of scans used in neutron inelastic scattering: constant- E scan and constant- \mathbf{Q} scan. Constant- E energy scans are performed by keeping the energy transfer $h\omega$ fixed while varying the momentum transfer \mathbf{Q} : Constant- \mathbf{Q} scans are performed by holding the momentum transfer \mathbf{Q} , while varying the energy transfer $h\omega$. Using these scans, the dispersion of both the transverse acoustic (TA) and the lowest-energy transverse optic (TO) phonon modes can be mapped.

Neutron inelastic scattering were performed on PMN-0.32PT at BT7 using a

double-focusing spectrometer. Three pieces of crystals were glued together with a misalignment of $<1^\circ$. The (002) reflection of highly oriented pyrolytic graphite (HOPG) crystals was used to monochromator the incident neutron energy E_i and to analyze final neutron energy E_f . Data was taken with a fixed final neutron energy of $E_f=14.7\text{meV}$ ($\lambda=2.36\text{\AA}$), and horizontal collimations of open-50'-S-40'-120' between the source and detector. An HPOG transmission filter was used after the analyzer to eliminate high-order neutron wavelengths. The glued crystals were mounted onto an aluminum holder and oriented with either the cubic [001] or [110] axis horizontal. The room temperature lattice constant was set as $a=4.004\text{\AA}$; therefore, one reciprocal lattice unit (r.l.u.) equals to 1.5692\AA^{-1} . It was then placed inside a vacuum furnace capable of reaching temperature up to 600K. An electric field was applied along [001] below 450K.

Constant-Q scans were performed on the (220) Brillouin zone along the symmetry direction [001] by holding the momentum transfer $\mathbf{Q}=\mathbf{k}_i-\mathbf{k}_f$ fixed while varying the energy transfer ΔE . Using these scans the dispersion of both the transverse acoustic and the lowest-energy transverse optic phonon modes were mapped out at several temperature points. The original data was corrected using higher-order contamination of the monitor [65]. To investigate the effect of mode coupling model cross section, we carried out a detailed lineshape analysis, details of which can be found elsewhere [66, 67]. The linewidth, amplitude, and frequency of phonons were obtained from fitting to a Lorentzian lineshape: Gaussian was used to describe the intensity at $\hbar\omega=0$; and a constant was used to describe the overall background.

CHAPTER 3

Fragile phase stability of $(1-x)\text{Pb}(\text{Mg}_{1/3}\text{Nb}_{2/3}\text{O}_3)\text{-xPbTiO}_3$ crystals

In the solid solution PMN-xPbTiO_3 (PMN-xPT), a spectrum of structures and a variety of macroscopic properties can be “tuned” by Ti^{4+} substitution, ranging from pseudo-cubic in the relaxor state to ferroelectric rhombohedral (R), monoclinic (M) and tetragonal (T) phases near the morphotropic phase boundary (MPB). Recently, a new revised MPB phase diagram for PMN-xPT ceramics in the zero-field cooling (ZFC) condition was reported by Noheda *et al.* [22] based on high-resolution synchrotron x-ray-diffraction data. It revealed the presence of an intermediate M_C phase ($0.31 < x < 0.37$), sandwiched between the R and T phases.

In this thesis, two new phase diagrams for [001] and [110] electric field (E) cooled PMN-xPT crystals, for compositions both near and away from the MPB, have been constructed. Our findings are summarized in Figure 3.1 (a) and (b), respectively. Comparisons of the [001] and [110] FC phase diagrams for PMN-xPT will reveal:

- (i) a region (C') of abnormal thermal expansion ($c \neq a$) above the dielectric maximum, which exhibits a relaxor-to-normal phase transition on cooling, but only if there is an intermediate T phase sandwiched between the C' and R phases (see Section 3.1),
- (ii) that the M_C phase in the [001] FC diagram is replaced by an O phase in the [110] FC diagram (see Section 3.2),
- (iii) that the R phase of the ZFC state is replaced by a M_A one in the [001] FC diagram, but with a M_B one in the [110] FC one (see Section 3.3).

These differences in [001] and [110] phase diagrams under moderate electric fields ($0.25\text{kV/cm} \leq E \leq 1\text{kV/cm}$) demonstrate that the phase stability of PMN-xPT crystals is quite fragile, or simply put many phases are apparently very close to being energetically degenerate.

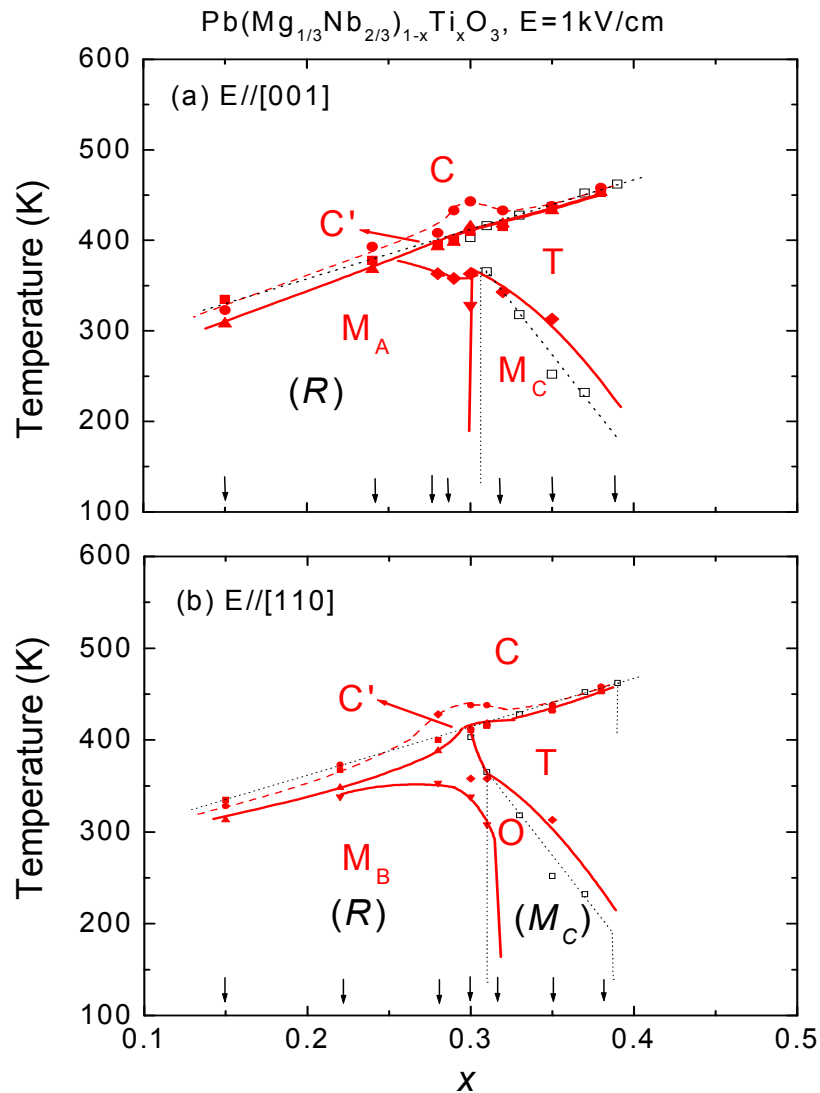


Figure 3.1 Modified phase diagrams of (a) [001] and (b) [110] electric field cooled PMN-xPT crystals. The dotted lines and open square signs were based on prior studies by Noheda *et al.* [21] (Reprinted with permission from [21]. Copyright [2002], American Physical Society). The bracketed italic R and M_C represents the rhombohedral and monoclinic phases of the zero-field-cooled condition. The solid square signs represent the temperature of the dielectric maximum (T_m). The solid circle signs represent the temperature of phase transition in FC condition. The C' phase below the upper dashed curve was determined by a region of abnormal thermal expansion. Solid curves drawn through these data point are only for guide of eyes.

Domain configurations of various phases under electric field in reciprocal space

Now let us consider the domain configurations of various phases in the phase diagram of Fig. 3.1. We do this so we can upfront identify what the mesh scans of these various domain states must look like, with regards to a reciprocal space representation.

For high symmetric ferroelectric phases such as T, O and R ones, the polarization is constricted to a particular crystallographic axis. This results in relatively simple domain configurations. For examples, the T phase has six equivalent polar vectors distributed along the $\langle 100 \rangle$ direction; the R phase has eight ones along the $\langle 111 \rangle$ direction; and the O phase has twelve along the $\langle 110 \rangle$. Whereas, the lower monoclinic symmetry has twenty-four domain states, where the monoclinic polar vectors are constrained within crystallographic planes, rather than along some a particular crystallographic axis. This results in very complicated domain configurations. However, once an electric field is applied to a monoclinic structure, a much simpler situation prevails. For example, the domain configuration of the monoclinic M_C phase in a reciprocal space is illustrated in Figure 3.2. Under application of $E//[001]$, the c axis is now fixed along the direction of E . As shown in the $HK0$ plane in Figure 3.2 (a), there are only two b domains related by a 90° rotation about the c axis. Each of these b domains contains two a domains in which a_m forms angles of either β or $180^\circ - \beta$ with c_m (see Figure 3.2(b)). The four polarization vectors, which rotate under the electric field within the ac plane, form identical angles with the $[001]$ direction.

Figure 3.3 summarizes the domain configurations in reciprocal space for T, M_C and M_A phases with $E//[001]$ and for T, O and M_B phases with $E//[110]$. In the case of $E//[001]$, the T phase has a single domain state (Figure 3.3(a)); M_C and M_A phases have similar domain configurations except for an exchange between the $(HH0)$ and $(H00)$ zones, as shown in Figure 3.3(b) and 3.3(c). This exchange occurs due to the fact that the M_A unit cell is doubled, having a unique b_m axis along the $[110]$; whereas, the M_C unit cell is primitive, having a unique b_m along $[010]$. In the case of $E//[110]$, the electric field fixes the $[110]$ axis. In this T phase, only two polar vectors exist ($P//[100]$ and $P//[010]$), which are both constrained to the (001) plane. Twinning results in a very simple domain

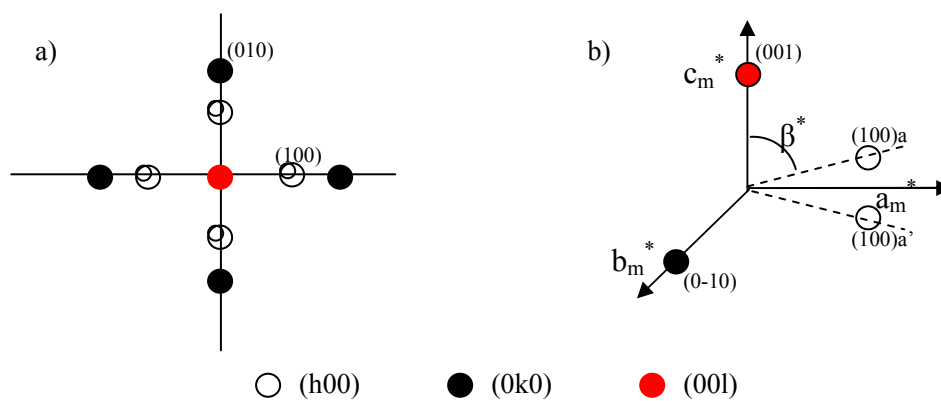


Figure 3.2 (a) $HK0$ plane in reciprocal space for monoclinic PZN-0.08PT showing the two b domains at $90^\circ \pm$, shaded and unshaded, in which H and K are interchanged with respect to each other [22]. The double circles represent the two a domains, illustrated in b. (b) Scheme of the reciprocal unit cell of one of the b domains showing the two a domains, a and a' , respectively. (Reprinted with permission from [22]. Copyright [2001], American Physical Society).

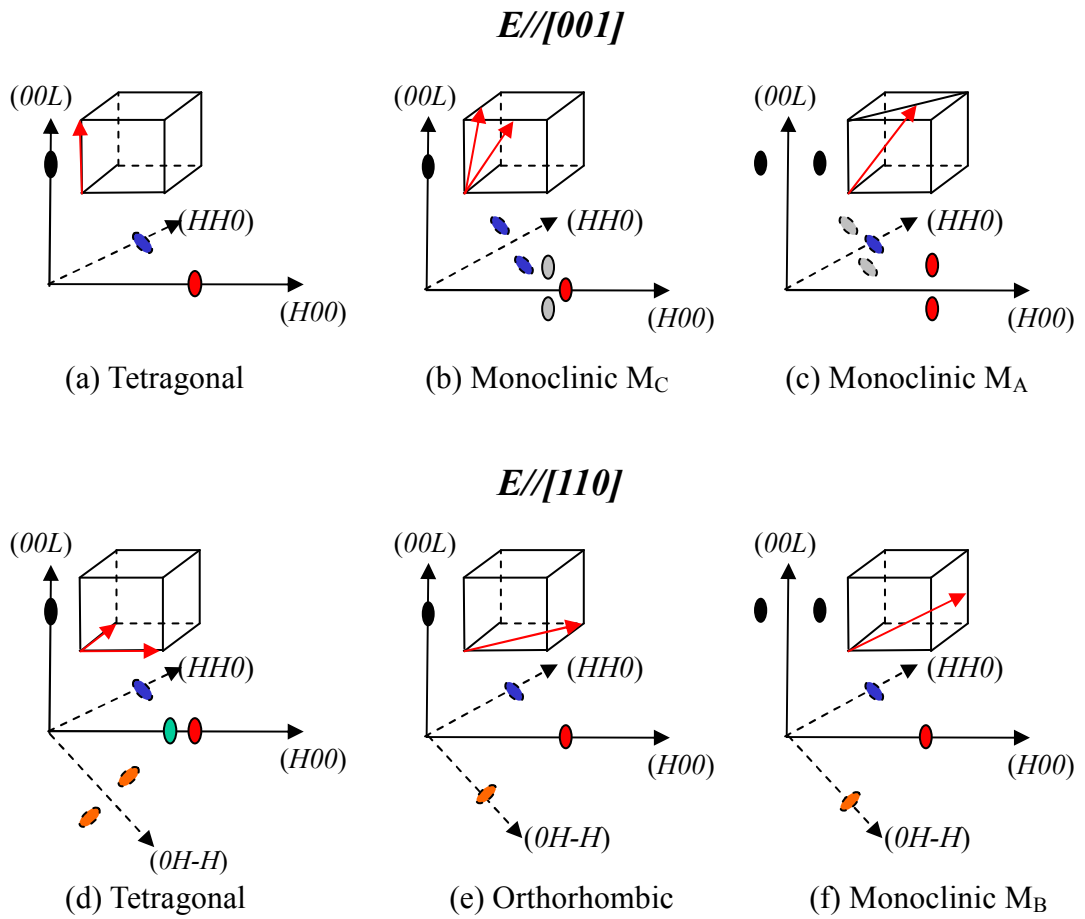


Figure 3.3 Domain configurations in reciprocal space as the application of electric field along $[001]$ for (a), (b) and (c); and along $[110]$ for (d), (e) and (f).

configuration, as shown in Figure 3.3(d); in the (H0L) zone, a two-domain splitting (with the same wavevector) occurs along the longitudinal (H00) direction. The right domain (having a larger lattice parameter) corresponds to the a domain, and the left one (having a shorter lattice parameter) to the c domain; whereas, in the (HHL) zone, a two-domain splitting (with the same wavelength vector) is seen along the [HH0] direction. For the O phase, $E//[110]$ fixes the domain orientations to the [110] direction. In this case, mesh scans performed in every zone exhibit only a single domain, as shown in Figure 3.3(f). In the M_B phase, two polar vectors are constrained within the (110) plane. This twinning also results in a very simple domain configuration, which is given in Figure 3.3(g): only the (00L) reflection shows a domain-splitting, while the other three reflections exhibit only a single domain.

3.1 Structural phase transition and phase boundary/stability studies of [001] field-cooled PMN-xPT

A recent study by Bai *et al.* [29] established that PMN-0.30PT has a $C \rightarrow T \rightarrow M_C \rightarrow M_A$ sequence in the FC condition, and a $R \rightarrow M_A \rightarrow M_C \rightarrow T$ one with increasing E beginning from the ZFC. Interestingly, an anomalous shift of T_C towards higher temperatures under electric fields was previously reported for PMN-0.30PT [29]. However, it is not yet known if this shift occurs only in a limited phase field in which the transformational sequence in the FC condition is $C \rightarrow T \rightarrow M_C \rightarrow M_A$, where there is limited ranges of T and M_C phase stability; or whether, the increase of the $C \rightarrow T$ boundary with increasing E may be characteristic of a wider phase field, in which the T and M_C phase stabilities are favored.

In this section, I have carefully performed XRD studies to characterize the structure of the composition PMN-xPT ($x < 0.33$) that is located on the PMN-rich side of the MPB as a function of temperature under various electric fields. Here, I report that the shift of the $C \rightarrow T$ phase boundary to higher temperatures with increasing E is a common characteristic of crystals whose compositions are in the vicinity of the MPB, irrespective of the width of the T and M_C phase regions (see Figure 3.1 (a) and (b)). Furthermore, the intermediate T phase is found to be very critical to trigger the sharpness of a relaxor-to-normal transition in electric field cooled PMN-xPT.

3.1.1 The C' phase region and an abnormal thermal expansion

Figure 3.4 shows mesh scans taken on cooling under $E=1\text{kV/cm}$. Scans taken at 430K, which is close to the $C \rightarrow T$ transition, revealed somewhat broadened contours. However, the lattice parameters extracted from these (002) and (200) scans were nearly identical. Possibly, over a narrow temperature range near T_C , there is a small degree of C and T phase coexistence. With decrease of temperature, the (002) peak shifted towards lower L values, and the (200) peak towards higher H values. This demonstrates a $C \rightarrow T$ transition on cooling. However, as shown in the (200) mesh scan at 375K, an additional weak peak is present, indicating some 90° -domain formation along the $\langle 101 \rangle$. This is possibly due to a limited penetration depth of our x-ray probe, but either way we did not observe a fully-aligned single domain configuration. Upon further cooling to 300K, the (200) reflection was found to split into three peaks – two (200) peaks, and a single (020) one; whereas, the (002) reflection remained as a single peak. Clearly, the (200) and (002) mesh scans at 300K have the signature features of the M_C phase (see Figure 3.3(b)). The lattice parameters as a function of temperature on cooling under $E=1\text{kV/cm}$ are plotted in Figure 3.5. At 430K, a decrease in the a -parameter was found at the $C \rightarrow T$ transition. Near the $T \rightarrow M_C$ transition at $\sim 350\text{K}$, c_m decreased with respect to c_t , a_m increased with respect to a_t , and b_m was nearly equal to a_t . In general, we found the temperature dependent lattice parameters for PMN-0.32PT cooled under $E=1\text{kV/cm}$ to be nearly identical to corresponding ones for ceramics in the ZFC condition [22]- both exhibited stable M_C phases at 300K, with similar values of the lattice parameters.

Figure 3.6(a) shows the dielectric constant as a function of temperature for $350 < T < 460\text{K}$ taken under different electric fields in the FC condition. This data was taken on cooling using a measurement frequency of 1 kHz. A single transition can clearly be seen in ZFC condition near 410K. According to the ZFC phase diagram (redrawn in Figure 3.1(a)), this transition is the $C \rightarrow T$ one. Unlike prior results for PMN-0.30PT, our dielectric peaks for PMN-0.32PT were relative sharp near T_c , and only weakly frequency dependent (data not shown). Here, we defined T_c as the temperature at which the lattice constant c begins to increase in magnitude upon cooling. In this regard, PMN-0.32PT in the ZFC condition exhibits transition characteristics similar to those of a normal ferroelectric, rather than those of a relaxor.

PMN-32%PT, E//(001), E=1kV/cm, Cooling

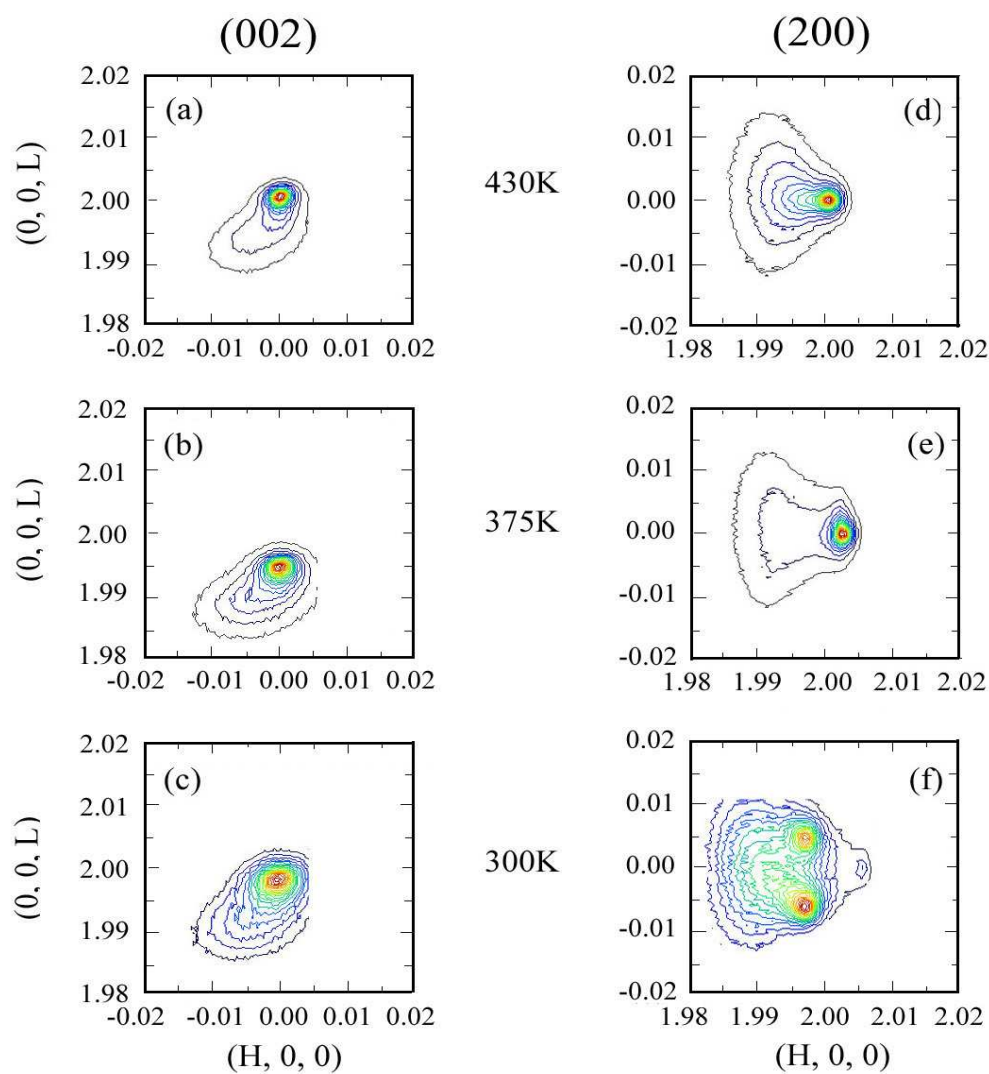


Figure 3.4 Mesh scans around the (002) and (200) profiles for PMN-32%PT at 430K, 375K, and 300K under as E=1kV/cm on cooling.

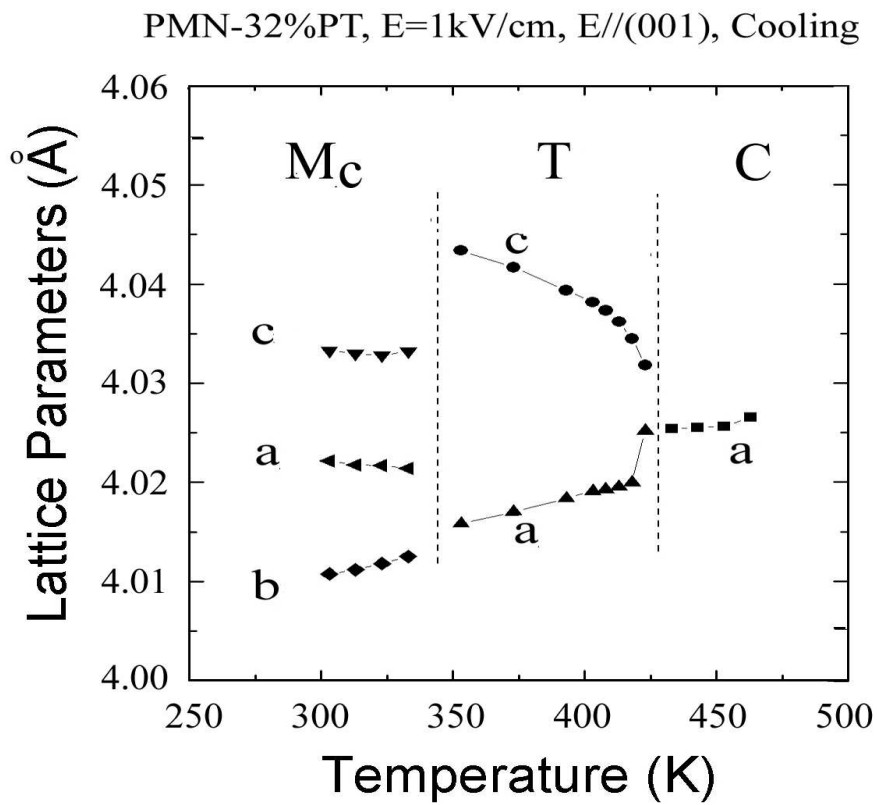


Figure 3.5 Evolution of lattice *c*-parameters as a function of temperature for PMN-32%PT under E=1kV/cm on cooling.

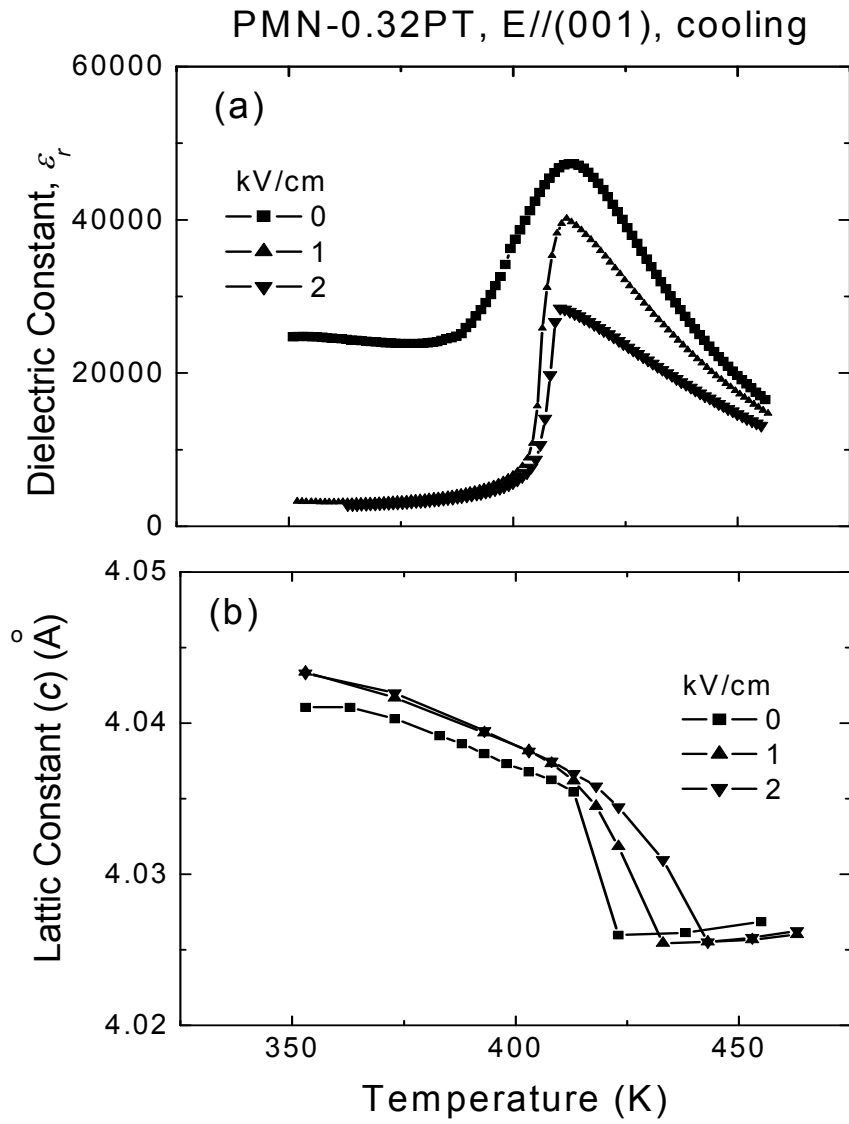


Figure 3.6 Temperature dependence of (a) the dielectric constants at 1 KHz and (b) lattice constants derived from (002) reflection under different levels of electric fields.

However, the C→T phase transition temperature, as determined by field dependent dielectric constant measurements, was not altered with increasing E. Although, in the FC condition, the magnitude of the dielectric constant was dramatically decreased in the T-phase region by field-cooling, even under a small field of E=0.5kV/cm.

Figure 3.6(b) shows the evolution of the lattice parameter *c* as a function of temperature at different electric fields. In this figure, it can clearly be seen that the C→T transition shifts towards higher temperature with increasing E. We determined the rate of increase in T_c for PMN-0.32PT to be $\sim 10\text{K}\cdot\text{cm}/\text{kV}$. In addition, no abnormal changes in the lattice parameter values or its slope can be seen in Fig. 3.6(b) for temperatures below 410K. This indicates that there is a region where the T and C phases coexist, which is also consistent with our above observations in Figure 3.4 concerning the mesh scans at 430K.

An important observation from this work for PMN-0.32PT is an apparent difference between T_c as determined by comparisons of dielectric and structural measurements in the FC condition. I summarized in the PMN-xPT phase diagram given in figure 3.1 the shift in the C→T boundary upon the application of E=1kV/cm (shown in red dash line), as determined by XRD. Also summarized in this phase diagram is the relative magnitude of the shift in the C→T phase boundary over a wide composition field (note: all XRD data). It is relevant to notice that the C→T boundary shift-rate was reduced as the MPB was approached, with increasing x. For example, we observed a shift-rate of $\Delta T_c/\Delta E \sim 10\text{K}\cdot\text{cm}/\text{kV}$ for PMN-0.32PT; whereas, the shift-rate for PMN-0.30PT was previously reported to be $\sim 25\text{K}\cdot\text{cm}/\text{kV}$. Furthermore, in this investigation, we found PMN-0.25PT (which has relaxor characteristics) to have an identical rate to that for PMN-0.30PT with $\Delta T_c/\Delta E \sim 25\text{K}\cdot\text{cm}/\text{kV}$ (data not shown, but summarized in the phase diagram). Our summary of results demonstrates that the increase of the C→T boundary with increasing E is not limited to a phase field with narrow ranges of T and M_C stability; but, rather is seemingly a common characteristic of crystals whose compositions are in the vicinity of the left-hand side of the MPB, irrespective of the width of the T and M_C phase regions. Although, the value of $\Delta T_c/\Delta E$ is reduced as one approaches the MPB, and crosses over into the T-phase region on the right-hand side of the MPB.

One possible explanation for the dependence of the C→T phase boundary on E is that polar nanoregions (PNRs) exist near T_c , for compositions on the left-hand side of the MPB. Application of E along [001] might then readily favor an alignment of PNRs whose polarization is oriented along the *c*-axis. The observed shift in the C→T phase boundary could then simply reflect a change in the relative population of tetragonal PNR variants under E. Due to the diffuse nature of the transition, the volume fraction of tetragonal PNRs would gradually increase on cooling over a relatively broad temperature range, allowing for gradual lattice parameter changes. However, for PMN-0.32PT whose *c/a* ratio is larger in the T phase than PMN-0.30PT, the coexistence of tetragonal domains with the cubic phase would be suppressed by a significantly higher elastic energy density, i.e., $\sim(c/a)^2$. Thus, the C→T phase transformation near and above the MPB would be sharper, and its phase boundary more difficult to shift under E.

3.1.2 Role of intermediate T phase in relaxor-to-normal ferroelectric transition

Interestingly, in the PMN-xPT diagram, the stability of an intermediate T phase field can be seen to be shifted to lower PT contents by application of E//(001). In the FC condition for $0.25 < x < 0.30$, this intermediate T phase is stable over a narrow temperature, bridging the C and M phases. This is notably different from the ZFC condition, where the transitional sequence is C→R. In this section, we will show the importance of this intermediate T phase on triggering the sharpness of a relaxor-to-normal transition in field-cooled (001)_C PMN-xPT crystals for $0.25 < x < 0.30$.

Figure 3.7 shows the lattice parameters as a function of temperature under E=0.5kV/cm for (a) PMN-0.24PT and (b) PMN-0.28PT. For both crystals, the (002) and (200) reflections did not exhibit any splitting at temperatures greater than T_m . Thus, it is clear both are cubic in this temperature range, with $a \approx c$. On cooling in the C phase, the a_c lattice parameter, as derived from the (002) reflection, decreased linearly with decreasing temperature. In the vicinity of T_m of the respective crystals, an abnormal positive thermal expansion was observed in the lattice parameter with decreasing temperature. No other peak splitting was observed. For PMN-0.24PT, with further decreasing temperature, a C→M_A transition

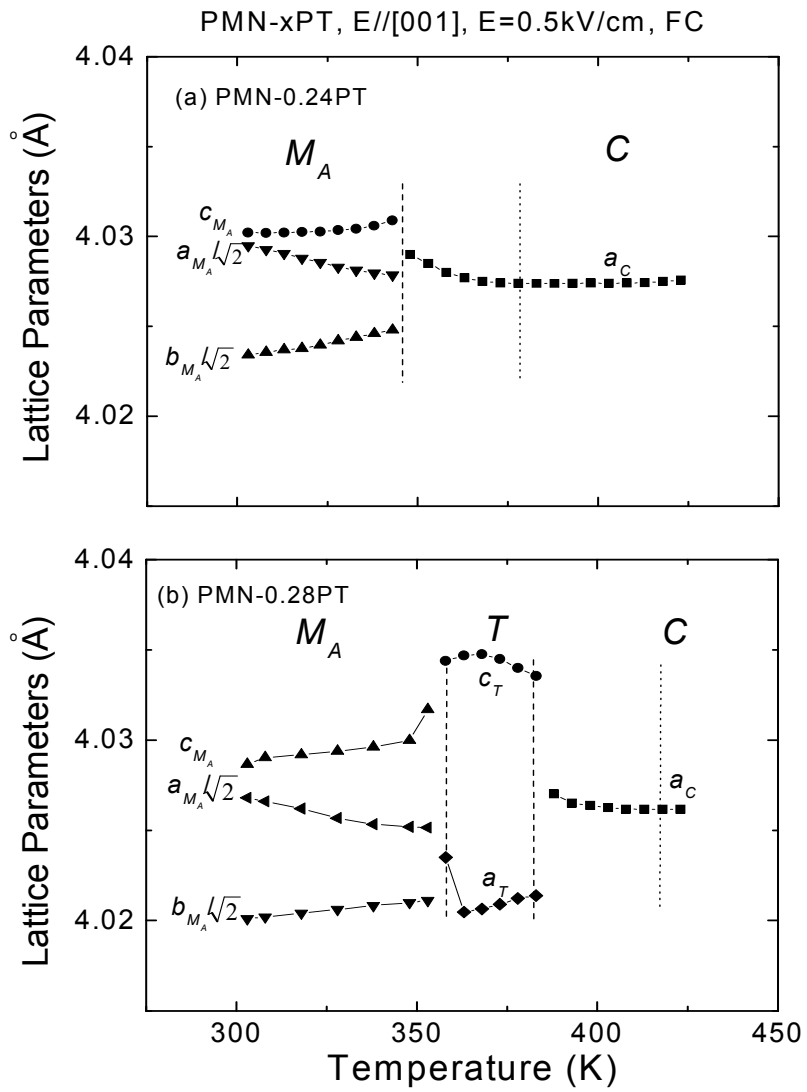


Figure 3.7 Temperature dependence of the lattice parameters under $E=0.5\text{kV/cm}$ applied along $[001]$ for (a) PMN-0.24PT and (b) PMN-0.28PT.

occurred at 346K; where the value of c_m exhibited a sharp increase, and that of $a_m/\sqrt{2}$ and $b_m/\sqrt{2}$ a sharp decrease. For PMN-0.28PT an intermediate T phase was found between 382K and 358K, which subsequently transformed to M_A at 358K.

Figure 3.8 shows the dielectric constant ($f=1\text{kHz}$) as a function of temperature under $E//[001]$ for (a) PMN-0.24PT and (b) PMN-0.28PT. The ZFC dielectric behavior of both crystals exhibited a broad peak, typical of relaxor ferroelectrics. However, the FC dielectric behaviors were quite different. For PMN-0.24PT ($T_m=378\text{K}$), the dielectric constant decreased upon application of $E=0.5\text{kV/cm}$ for $T<342\text{K}$. X-ray mesh scans (not shown) revealed that PMN-0.24PT had a cubic structure between 378K and 342K, and a M_A one at temperatures lower than 342K. With increasing E , the $C\rightarrow M_A$ boundary shifted to higher temperature, reaching T_m under $E=2\text{kV/cm}$. Whereas, for PMN-0.28PT ($T_m=400\text{K}$), the dielectric behavior under $E=0.5\text{kV/cm}$ exhibited a sharp decrease near 376K, indicating a relaxor-to-normal ferroelectric transition. With decreasing temperature, a secondary phase transition was found at $\sim 350\text{K}$. Mesh scans revealed that PMN-0.28PT had a T structure below 376K, and a M_A one below the secondary dielectric maximum of 350K. With increasing E , the temperature for the relaxor-to-normal (or $C\rightarrow T$ boundary) ferroelectric transition shifted to higher temperature. Comparisons of the results in Figures 3.7 and 3.8 for $E=0.5\text{kV/cm}$ will show a correspondence of (i) the relaxor-to-normal transition of PMN-0.28PT with an intermediate T phase; and (ii) the secondary transition on PMN-0.28PT, and the sharp decrease of the dielectric constant of PMN-0.24PT, with a transition to the M_A phase.

The relaxor-to-normal ferroelectric phase transition has previously been explained by interactions between PNR's, which are strong enough to provoke ferroelectric-type ordering below T_m . Structural evolution can be considered in three steps. First, near T_B (Burns temperature), clusters of short-range polar order (i.e. PNR's) gradually increase in number and grow on cooling. Second, with decreasing temperature, the ensemble of PNR's become percolating, resulting in abnormal thermal expansion near T_m , as can be seen in Figure 3.7(a); application of E then aligns these PNR's. Third, below T_m , a field-forced structural phase

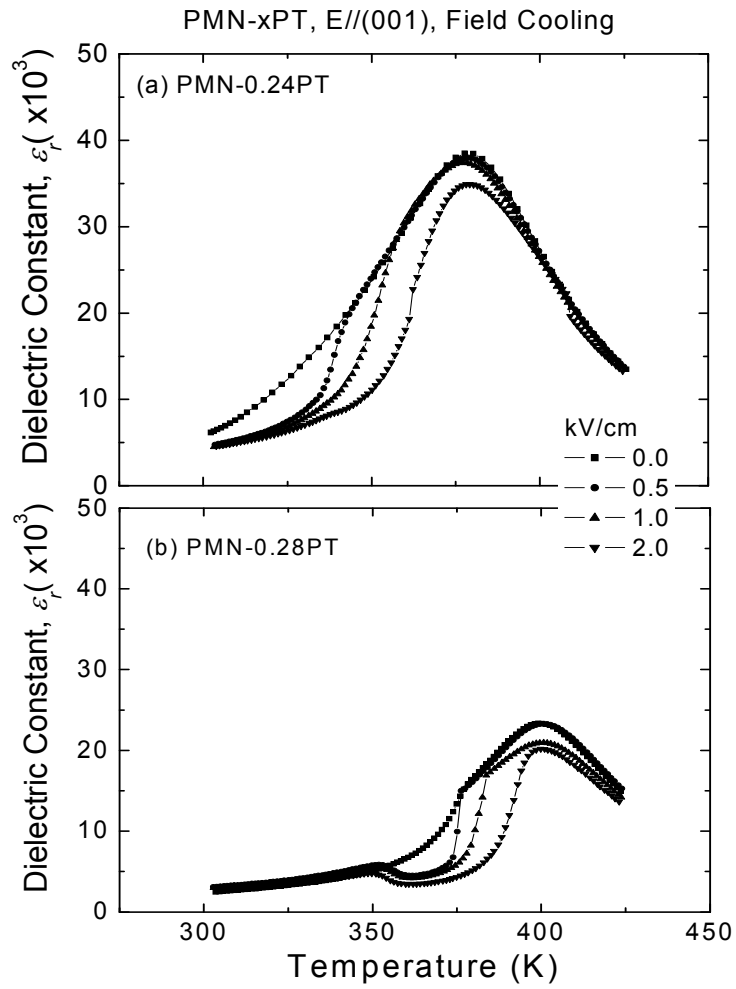


Figure 3.8 Temperature dependence of the dielectric constant (1kHz) under various electric fields for (a) PMN-0.24PT, and (b) PMN-0.28PT

transition occurs from the PNR ensemble condition to abnormal ferroelectric state-this transition is first order-like, and once induced is stable on further cooling. Previous investigations reported that the relaxor-to-normal transition was spontaneous in tetragonal relaxor systems, whereas rhombohedral ones possessed such abrupt changes only in the FC condition. It was argued that the large c/a ratio of the tetragonal structure was the driving force triggering the spontaneity, whereas systems with smaller c/a ratios (such as rhombohedral) could only undergo a field-forced transition. However, our findings here provide a better unifying structural basis for a relaxor-to-normal transition--a tetragonal structure is required in all cases. For PMN-xPT, the lack of a spontaneous transition in the ZFC condition is due to the fact that the phase transitions sequence does not proceed through a tetragonal phase; however, on field-cooling the transformational sequence is altered, and an intermediate tetragonal structure is present over a narrow temperature range. The expression of a fully formed tetragonal phase is critical to the sharpness of the relaxor-to-normal transition.

3.2 Orthorhombic VS monoclinic M_C in [110] and [001] electric field cooled PMN-xPT

In this section, I have studied the phase stability of PMN-0.35PT crystals for both $E//[001]$ and $E//[110]$ by high resolution XRD. My findings establish a M_C phase on [001] field cooling, but an O phase (or limiting M_C) on [110] field cooling.

Figure 3.9 shows mesh scans taken around the (002) and (200) reflections for [001] FC PMN-0.35PT at various temperatures for $E=2\text{kV/cm}$. At 475K (data not shown), the (002) and (200) mesh scans did not exhibit splitting, and it was found that $c=a$. Thus, it is clear that the lattice has cubic symmetry. As the temperature was decreased, the (002) and (200) mesh scans both exhibited one peak; but an elongation of the lattice constant c , and a contraction of a , were clearly observed, as shown in Figure 3.9(a) and 3.9(b) at $T=393\text{K}$. This indicates that the crystal transforms into a T structure. Upon further decreasing temperature, a second transition to a M_C phase was found, as shown in the Figure 3.9(c) and 3.9(d) at 300K. The (200) peak split into three reflections, (200) twin peaks and one (020) single peak; whereas, the (002) remained as a single reflection. We also studied the temperature dependence of the lattice parameters for a PMN-0.35PT crystal in the [110] field cooled condition. Relative to

PMN-35%PT, E//[001], E=2kV/cm, Field Cooling

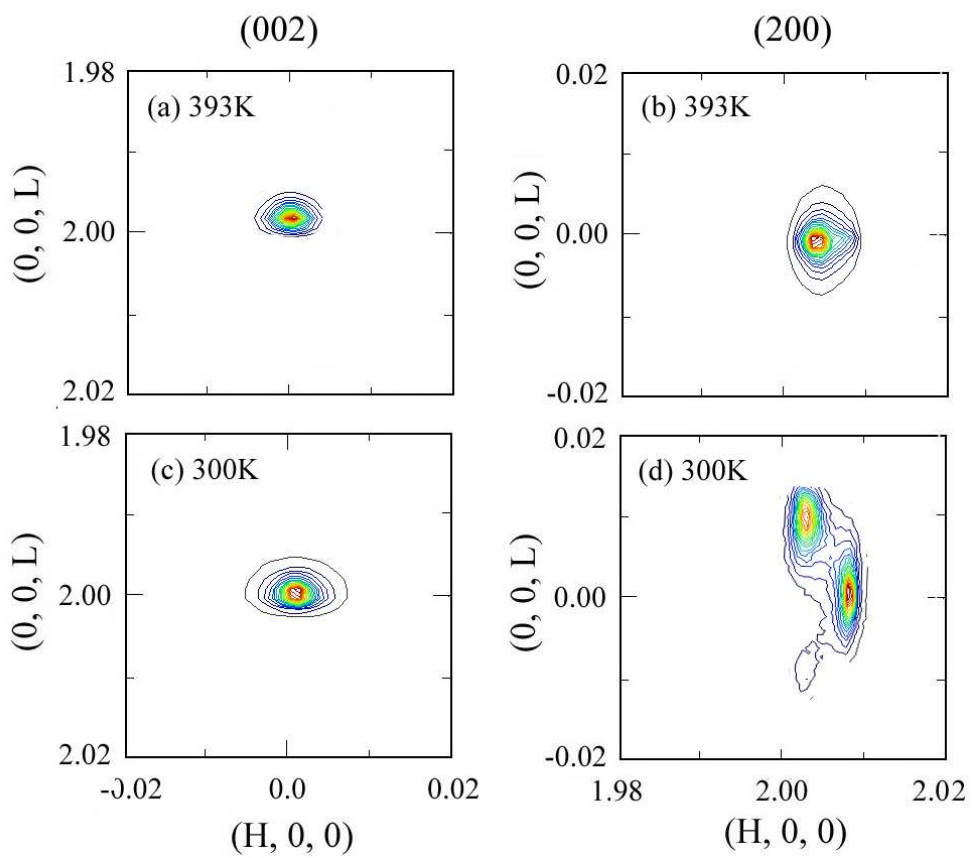


Figure 3.9 Mesh scans taken around (002) and (200) reflections of PMN-0.35PT with E=2kV/cm applied along [001] at 393K and 300K in the FC condition.

[001] FC PMN-0.35PT, [110] field cooling results in a more complicated domain configuration. This is because [001] field cooling fixes the prototype c -axis, whereas [110] field cooling only fixes the crystallographic [110] direction. To obtain a more comprehensive understanding, we then measured field cooling mesh scans about the (002), (200), (220) and $(\bar{2}\bar{2}0)$ reflections for a $E//[110]$ of 2kV/cm.

Figure 3.10(a)-(d) show mesh scans at 400K taken around these four directions, respectively. The (002) reflection (see Figure 3.10(a)) only has a single sharp peak. The lattice constant extracted from it was 4.0119Å. However, the (200) reflection (see Figure 3.10(b)) was split into two peaks along the longitudinal direction, with the lattice parameters of $a=4.0122\text{Å}$ and $c=4.0361\text{Å}$. [110] field cooling constrains the polarization in the T phase to the (001) plane. The a_T lattice parameter is then derived from the (002), whereas c_T is obtained from the (200) reflection. Since [110] field cooling fixes the [110] crystallographic orientations, the $(\bar{2}\bar{2}0)$ mesh scan (see Figure 3.10(c)) splits into two peaks along the transverse direction, but remains as a single peak for the (220) scan (see Figure 3.10(d)). Accordingly, for $(\bar{2}\bar{2}0)$ mesh scan, a- and b- twinning in the (001) plane is only seen along the transverse (220) direction. Our results in Figure 3.10 evidence a tetragonal lattice, with 90° domain formation only in the (001) plane, whose polarization is constrained along the [100] and [010] direction.

As the temperature was further decreased on [110] field cooling, the longitudinal splitting in the (200) mesh scan disappeared near 308K, indicating another phase transformation. Figures 3.11 (a)-(d) show mesh scans at 303K within this phase field that were taken about the (002), (200), $(\bar{2}\bar{2}0)$, and (220) reflections, respectively. Only a single domain was observed in each of these scans, indicating the presence of a well-developed single domain state throughout the entire crystal. The structure of this phase was determined to be orthorhombic, where the polarization is fixed to the [110]. The lattice parameters of this orthorhombic phase were determined from these mesh scans to be $a_o=5.7055\text{Å}$, $c_o=5.6870\text{Å}$, and $b_o=4.0050\text{Å}$, where a_o was extracted from the (220) reflection, c_o from the $(\bar{2}\bar{2}0)$, and b_o

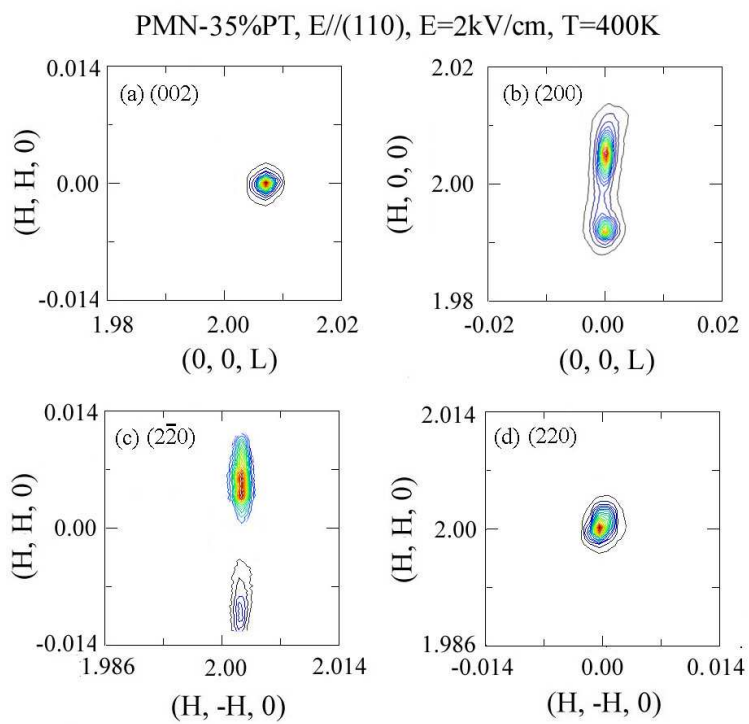


Figure 3.10 Mesh scans taken around (002), (200), $(2\bar{2}0)$, and (220) reflections of PMN-0.35PT with E=2kV/cm applied along [110] at 400K in the FC condition.

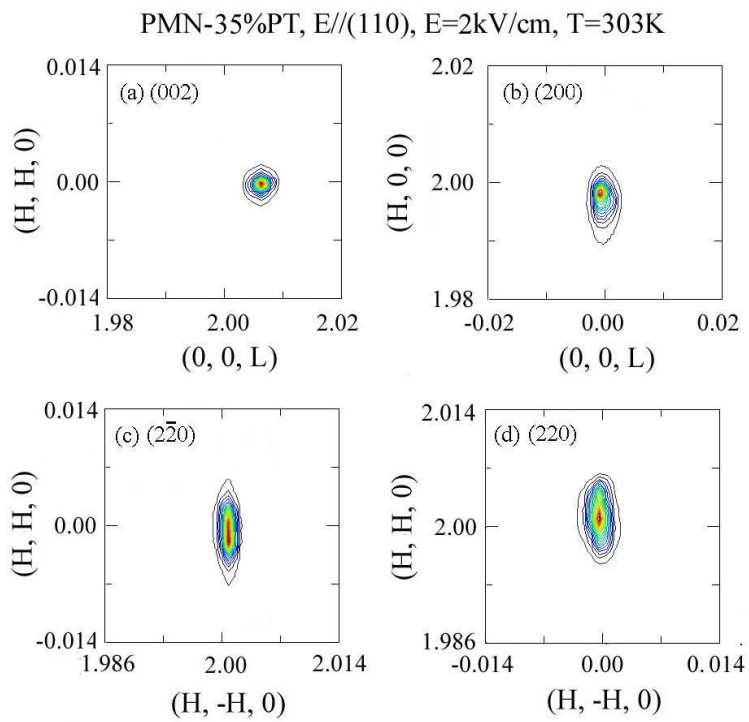


Figure 3.11 Mesh scans taken around (002), (200), ($2\bar{2}0$), and (220) reflections of PMN-0.35PT with E=2kV/cm applied along [110] at 303K in the FC condition.

from the (002). This O structure has an equivalent limiting M_C primitive cell with the corresponding lattice parameters of $a_m=c_m=4.0279\text{\AA}$, $b_m=4.005\text{\AA}$, and $\beta=90.186^\circ$.

Figure 3.12 shows the temperature dependence of the lattice constants for (a) an $E//[001]$ of 2kV/cm and (b) an $E//[110]$ of 2kV/cm. The results for the two orientations are identical except in the low temperature region, where [001] field cooling results in M_C , whereas [110] field cooling results in the O phase. The lattice constant c_t (a_t) gradually increased (decreased) as the temperature decreased and suddenly dropped near 308K. At lower temperatures, [001] field cooling resulted in a $T \rightarrow M_C$ transformation; whereas, [110] field cooling results in a $T \rightarrow O$. It is noteworthy that the values of b_m and b_o , were both continuous with a_t at their respective $T \rightarrow M_C$ and $T \rightarrow O$ transformations; whereas, the values of a_m ($a_o/\sqrt{2}$), and c_m ($c_o/\sqrt{2}$) exhibit sharp decreases at the $T \rightarrow M_C$ ($T \rightarrow O$) transformation relative to c_t . In addition, we found the O phase to be stable on removal of $E//[110]$, and correspondingly the M_C to be stable on removal of $E//[001]$. This illustrates a subtle yet important difference between the ground state of these two field-cooled conditions.

3.3 The intermediate monoclinic M_B phase in [110] and [111] electric field cooled PMN-xPT

Vanderbilt and Cohen predicted the stability ranges of monoclinic M_A and M_C phases using a thermodynamic approach [31]; in addition, they predicted a possible narrow stability range of a M_B phase, intermediate between R and M_C ones. Prior structural studies of PMN-xPT and PZN-xPT have only been performed under an E applied along the [001] direction – however, this is not an inherent restriction, as polarization rotation could occur in either direction in the permissible planes. For $BaTiO_3$, structural studies have been performed by Wada et. al. [34] under an E applied along the [111] direction, where a $T \rightarrow O \rightarrow R$ phase sequence was observed with increasing E at 300K; and where optical birefringence indicated the presence of bridging M phases. Dielectric property studies of PMN-0.33PT crystals with E along [110] have been published by Lu et. al.[33], who reported an intermittently-present metastable phase over a narrow temperature range sandwiched between M_C and M_A ones in the FC condition. Polarized light microscopy (PLM) indicated that this evasive phase was a

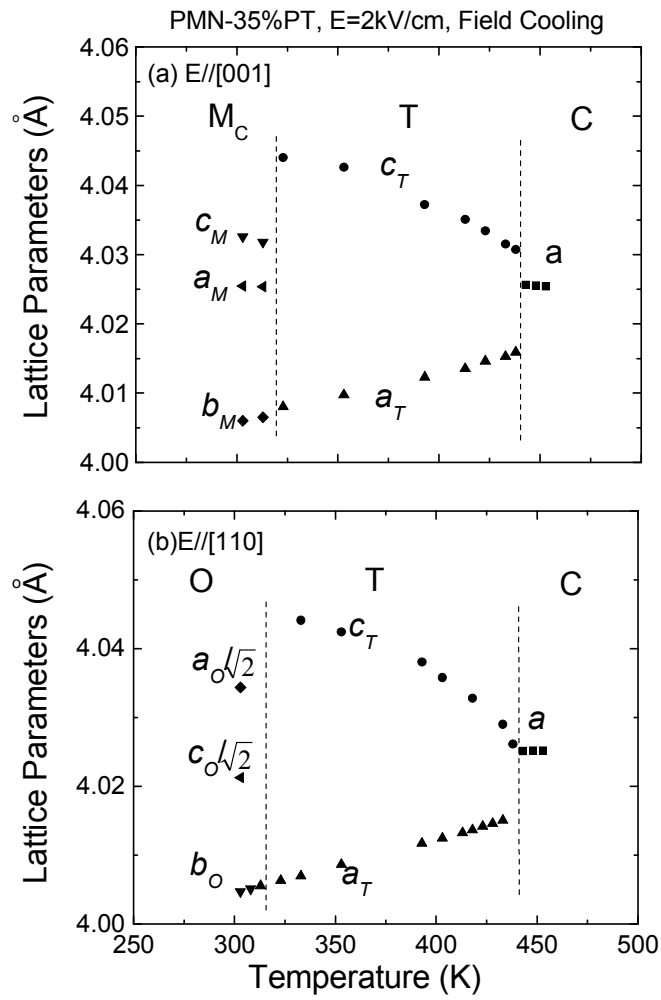


Figure 3.12 Temperature dependence of lattice parameters for PMN-0.35PT with (a) $E=1\text{kV/cm}$ applied along $[001]$; and (b) $E=2\text{kV/cm}$ applied along $[110]$.

single domain orthorhombic one [34]. In addition, the P-E and ϵ -E behaviors of ZFCPMN-0.30PT crystals with E along [110] have been reported by Viehland and Li [68], whom conjectured a field-induced O phase at room temperature, via a monoclinic M_B one. However, structural studies have not yet established this to be the case, nor has the phase sequence in [110] FC crystals yet been identified.

In this section, I have focused on establishing the structural transformation sequence of PMN-0.30PT crystals with E along [110] and [111]. The XRD studies unambiguously demonstrate a phase sequence of $C \rightarrow T \rightarrow O \rightarrow M_B$ for [110] and [111] FC PMN-0.30PT, but different than the $C \rightarrow T \rightarrow M_C \rightarrow M_A$ for $E//[001]$. Our results suggest that the phase sequences in a FC process with the electric field along different crystallographic orientations are distinctively different.

3.3.1 [110] electric field cooled PMN-xPT

Figures 3.13-3.15 show mesh scans taken around the (002), (200), $(2\bar{2}0)$ and (220) for PMN-0.30PT when the sample was cooled under $E=1\text{kV/cm}$. Data are shown at temperatures of 375 K, 343K and 298K, respectively. Please note the following points (i)-(iii).

- (i) At 450K under $E=1\text{kV/cm}$ (data not shown), the (002) and (220) mesh scans did not exhibit splitting, and it was found that $c=a$. Thus, it is clear that the lattice is cubic. As the temperature was decreased to 420K, the (002) reflection shifted towards slightly shorter wavevector and a splitting along the longitudinal direction was found around the (200) reflection indicating a transition to the T phase. The signature of the T phase became more pronounced with decreasing temperature.
- (ii) At 375K and 343K, the (002), (200), $(2\bar{2}0)$ and (220) reflections (see Figure 3.13 and 3.14) show the same domain patterns as tetragonal and orthorhombic phases observed for PMN-0.35PT under $E//[110]$. These interesting domain configurations confirm the same transformation sequence of $C \rightarrow T \rightarrow O$ for PMN-0.30PT under $E//[110]$. The tetragonal lattice constants were extracted to be $a=4.0142\text{\AA}$ and $c=4.0329\text{\AA}$. The lattice parameters for the orthorhombic phase were determined from the mesh scans to be $a_o=5.6924\text{\AA}$, $b_o=5.6812\text{\AA}$, and $c_o=4.0070\text{\AA}$.

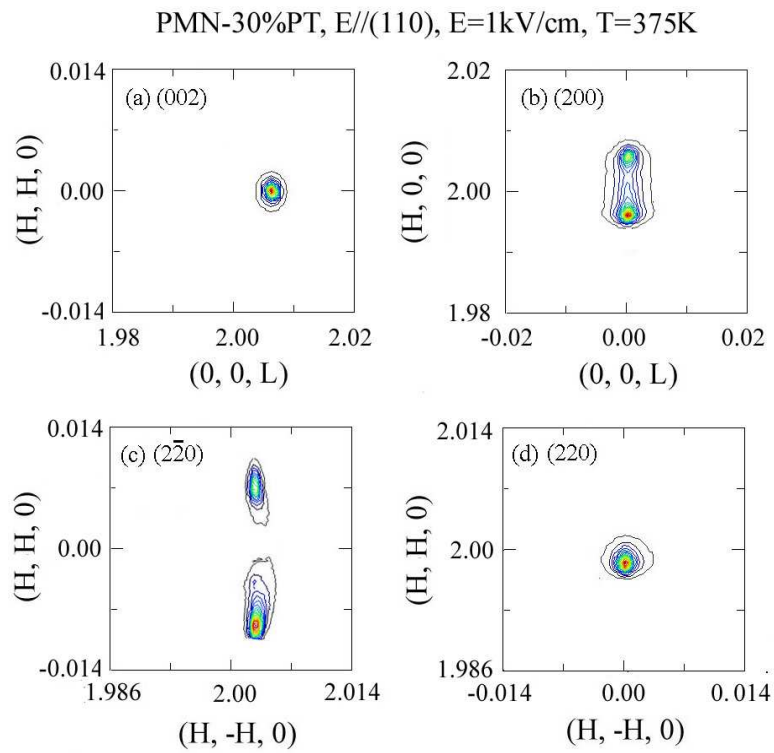


Figure 3.13 Mesh scans of (002), (200), ($2\bar{2}0$), and (220) of PMN-0.30PT with E=1kV/cm applied along [110] at 375K in FC condition

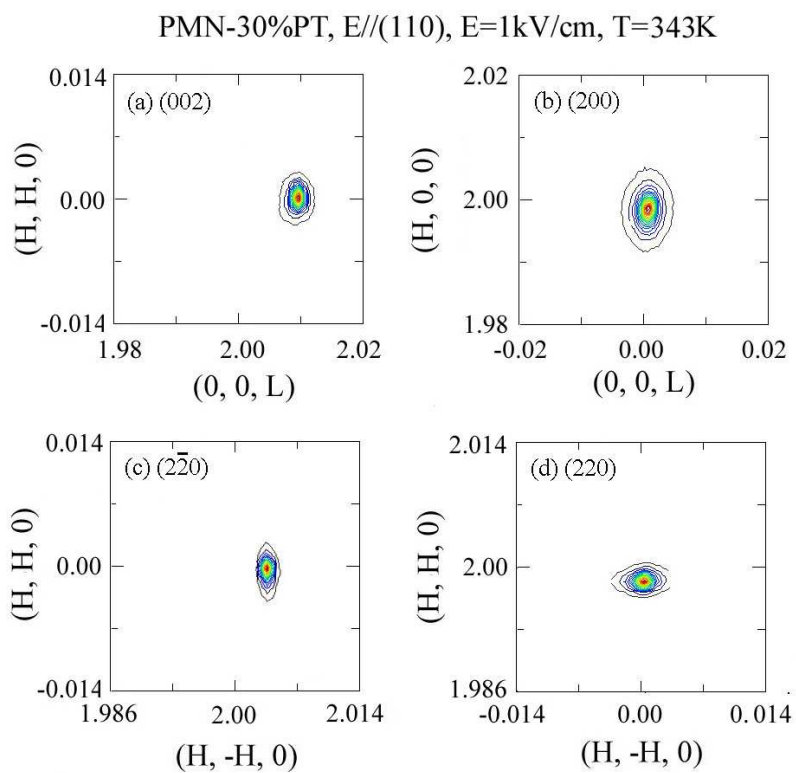


Figure 3.14 Mesh scans of (002), (200), ($2\bar{2}0$), and (220) of PMN-0.30PT with E=1kV/cm applied along [110] at 343K in FC condition

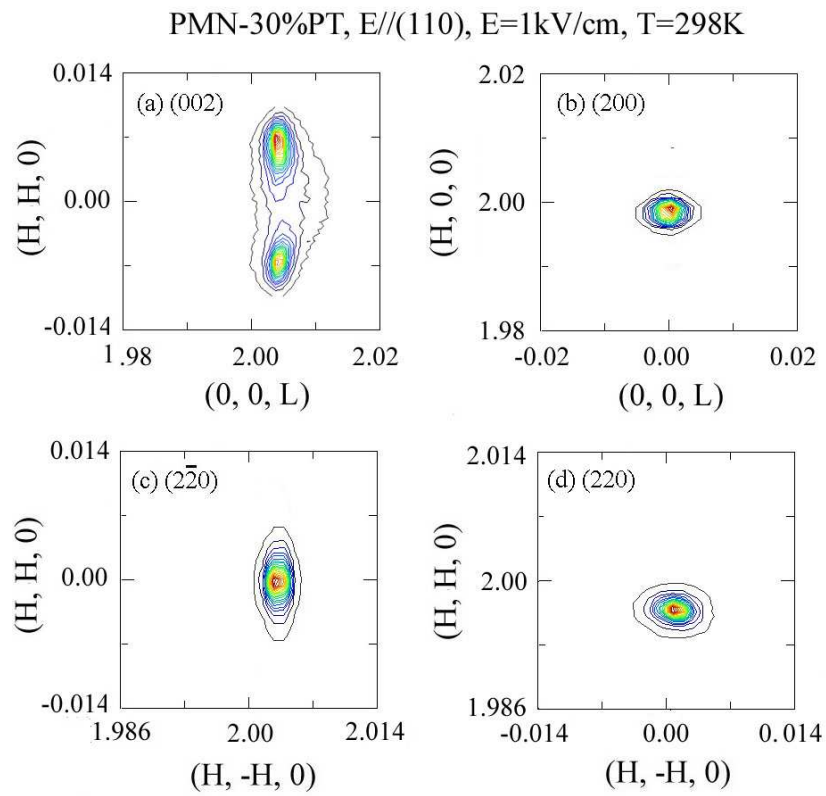


Figure 3.15 Mesh scans of (002), (200), $(2\bar{2}0)$, and (220) of PMN-0.30PT with E=1kV/cm applied along [110] at 298K in FC condition.

(iii) At 300K, the (002) mesh scan was found to split only along the transverse direction, revealing yet another phase transition. The (002) reflection (see Figure 3.15(a)) can be seen to split into two peaks with the same wavevector length; whereas, the other three mesh scans remained as a single peak. This is a signature of the monoclinic M_A/M_B phase. We then determined the lattice parameters by extraction from these mesh scans to be $c_m=4.0204\text{\AA}$, $a_m/\sqrt{2}=4.0280\text{\AA}$, and $b_m/\sqrt{2}=4.0181\text{\AA}$; where a_m and b_m were derived from the (220) and $(\bar{2}20)$ reflections, and c_m from the (002) one. These results that on field-cooling below $\sim 333\text{K}$, that a single-domain O phase, whose polarization is fixed to the [110] direction can no longer be saturated; rather, a transition to a polydomain monoclinic phase occurs. The unit cells of both the M_A/M_B phases are doubled with respect to the primitive pseudocubic one, where the polarization lies in the $(\bar{1}10)$ crystallographic plane. Although both the M_A and M_B phases belong to the Cm space group, there is difference between their polarizations, for M_A , $P_x=P_y<P_z$; whereas for M_B , $P_x=P_y>P_z$. The fact $a_m/\sqrt{2}>c_m$ confirms that this monoclinic phase is the M_B one. This is the first direct confirmation of the presence of the M_B phase in the transformational sequence of either PMN-xPT or PZN-xPT single crystals. It is relevant to note our prior reports of property data that indicate a $R\rightarrow M_B\rightarrow O$ phase transformational sequence in the ZFC condition [70] and equally relevant to note that it is consistent with thermodynamic theory of Vanderbilt and Cohen [30] that also allows for this transformation sequence.

The lattice parameters of [110] electric field cooled PMN-0.30PT at $E=1\text{kV/cm}$ are plotted as a function of temperature in Figure 3.16 (a). The lattice parameter a_c continuously decreases from 525K on cooling. At 428K, the value of a_c began to gradually increase, indicating the formation of a small volume fraction of tetragonal phase. Near 415K, a splitting of the lattice parameter into a_t and c_t was observed and the crystal was completely transformed into the T phase, where a_t was derived from the (002) reflection, whereas c_t was derived from the (200) one. Here, one thing should be mentioned. The [110] field-cooled PMN-0.30PT was a little different than the [001] field-cooled one, not only with regards to

the domain configurations, but also with respect to the derivation of the lattice parameters. For example, in the T phase, a_t was derived from the (200) reflection and c_t from the (002) reflection for [001] field cooled PMN-0.30PT. The C→T boundary shifted towards higher temperatures under a field of $E=1\text{kV/cm}$, relative to the ZFC condition. As the temperature was further decreased, subsequent phase transitions were observed. Between 358K and 333K, an orthorhombic phase was found with lattice parameters of c_o , a_o and b_o . It is noteworthy that the values of c_o and a_t , both determined from the (002) reflection, were continuous at the T→O transformation. The orthorhombic unit cell is a doubled one; and thus, the two lattice parameters, a_o and b_o , are square root two times of the corresponding monoclinic M_C unit cell. The values of $a_o / \sqrt{2}$ and $b_o / \sqrt{2}$ shown in Figure 3.16 (a) exhibit a sharp decrease at the T→O transformation, relative to c_t and a_t , respectively. On further cooling below 333K, a transformation to a monoclinic M_B phase was observed with three lattice c_m , $b_m / \sqrt{2}$, and $a_m / \sqrt{2}$. At the O→ M_B transformation, the values of $a_m / \sqrt{2}$ and $b_m / \sqrt{2}$ exhibited a sharp decrease, whereas c_m had a sharp increase.

The dielectric behavior of [110] electric field cooled PMN-0.30PT is shown in Figure 3.16 (b). A plate-like sample (0.7mm thickness) was polished from the original cubic-shape crystal used in the XRD studies. The results are consistent with the transformational sequence of C→T→O→ M_B in the FC condition for various field levels. First, no significant shift of the value of the temperature of the dielectric maximum (T_m) was observed at the C→T transformation with increasing E . It is relevant to note that the C→T boundary as determined by T_m did not shift with E , unlike that determined from the XRD data. The results of Figure 3.16 (b) also show subsequent lower temperature phase transitions, corresponding to the T→O and O→ M_B ones observed by the lattice parameter changes in Figure 3.16(a). The value of the dielectric constant was relatively high in all phase fields, except in the single domain orthorhombic region, in which the polar vector is in coincidence with the direction of [110] applied E .

Figure 3.17 (a)-(c) conceptually summarizes the domain configurations of the T, O, and M_B phases, in which an E has been applied along the [110] direction. In a ferroelectric T

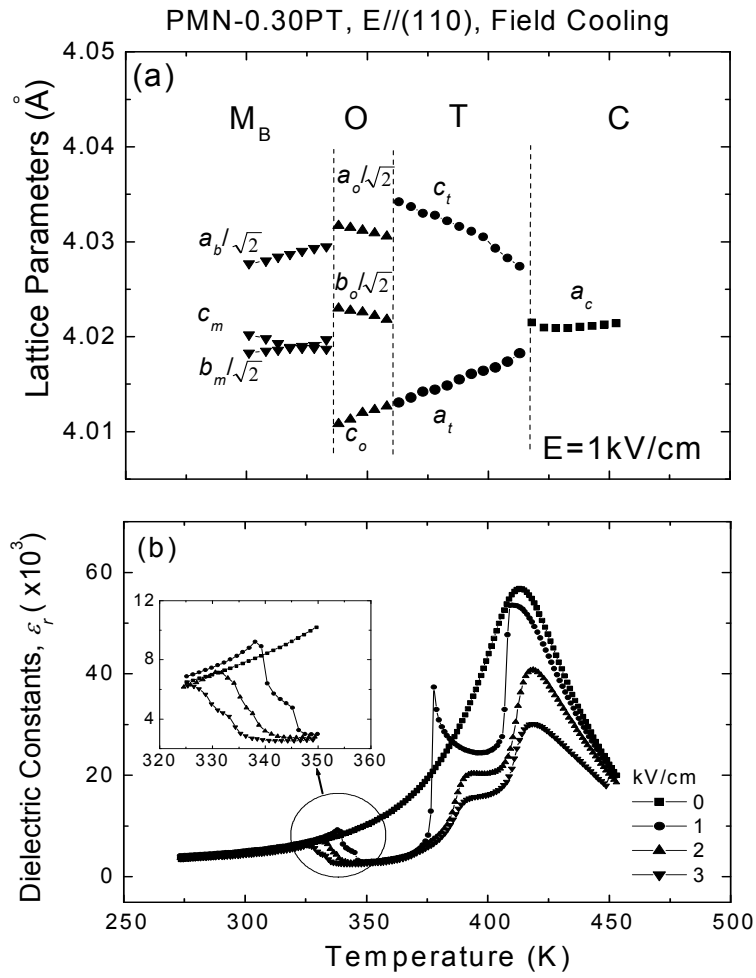


Figure 3.16 Temperature dependence of (a) lattice constants for PMN-0.30PT with $E=1\text{ kV/cm}$ along $[110]$, in which the lattice parameters $a_o/\sqrt{2}$, $b_o/\sqrt{2}$, and c_o ; and c_m , $a_m/\sqrt{2}$ and $b_m/\sqrt{2}$ are plotted, and (b) dielectric behavior under various levels of electric field at $f=1\text{ kHz}$ in FC condition.

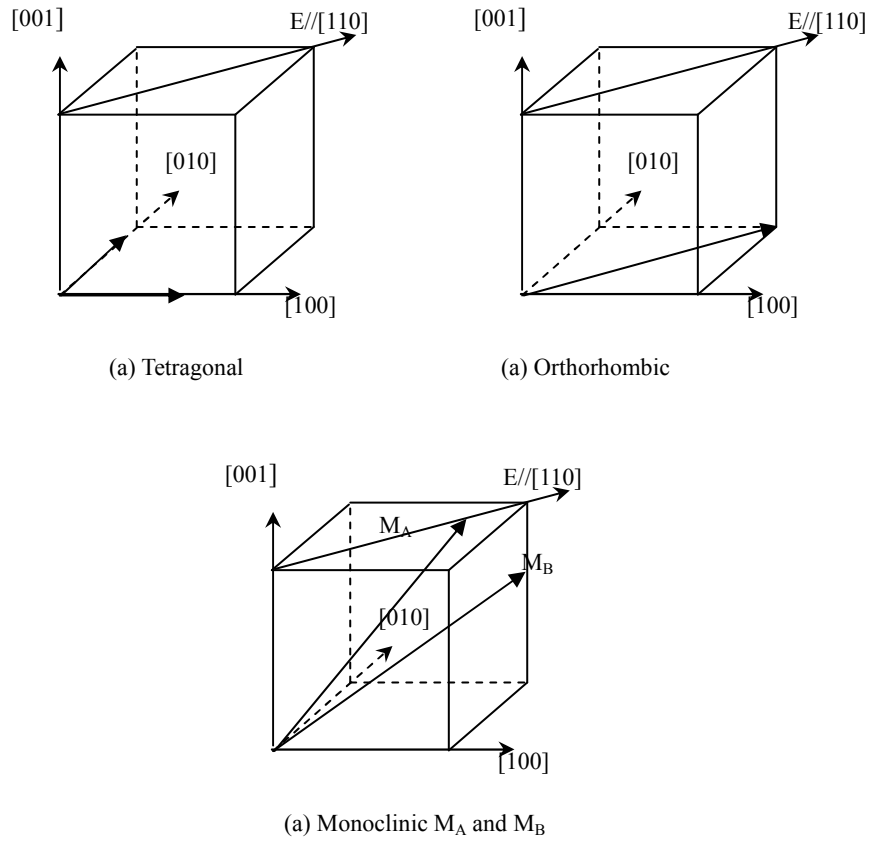


Figure 3.17 Schematic of tetragonal, orthorhombic and monoclinic M_C phases in PMN-0.30 PT with E along $[110]$. Arrows indicate the polar vector. Panels (a) are twin domains developed in the tetragonal phase and only two polarizations are constrained within (001) plane; panel (b) shows the single domain developed in the orthorhombic phase; and panel (c) indicates the domains developed in the M_B/M_A phase, in which the polarization vectors are constrained with the (110) plane.

phase, six equivalent variants are permissible along the [100] direction. However, only two of these six are favored by applying an E along [110], which are [100] and [010]. In the T phase of [110] electric field-cooled PMN-0.30PT, the [110] axis was fixed by the [110] field, and accordingly twinned *a*- and *b*-domains were found along [100] or [010] directions, as shown in Figure 3.17 (a). Figure 3.17(b) illustrates the single-domain orthorhombic state that is established throughout the crystal by [110] field cooling. Within this single domain, the polarization is fixed to only the [110] orthorhombic direction. There is no monoclinic tilting of this O variant away from the [110] direction. This unit cell is a doubled unit cell, formed by perfectly-adjusting two M_C simple cells. The domain configurations of monoclinic phases are quite complicated; however, once an E is applied, a much simpler situation prevails [22]. For example, in the case of [001] electric field cooled PMN-0.30PT [30] or PZN-0.08PT [35], the field fixes the *c*-axis to lie along the pseudocubic [001] direction; thus, there are only two *b*-domains related by a 90° rotation around the *c* axis, each of which has two *a*-domains. These are M_C (*a*-axis along [100]) and M_A (*a*-axis along [110]) domain configurations previously reported for PMN-0.30PT and PZN-0.08PT. However, [110] field cooling may result in slightly more complicated domain configurations, as an E field does not fix the *c*-axis to be along the [001] direction; rather, [110] field cooling fixes the [110] direction and forces the polarization as close as possible to the [110], as illustrated in Figure 3.17(c). However, in the monoclinic phase of [110] field cooled PMN-0.30PT, the polarization is rotated away from the orthorhombic within the $(\bar{1}10)$ plane, pointing towards the [001]. This domain configurations is that of the monoclinic M_B phase, since $P_x=P_y>P_z$ and $a_{M_B}/\sqrt{2} > c_{M_B}$. In this case, two polarizations were constrained to the $(\bar{1}10)$ plane, consistent with a single peak in the (220) mesh scan and two domains in the (002) mesh scan.

The field dependence of the lattice parameters was then determined at room temperature, beginning from the ZFC condition. The crystal was first heated to 525K, and subsequently cooled under zero fields. The (002) and (220) XRD mesh scans were obtained at various DC biases. Figures 3.18 (a)-(d) show the (002) scans for the field sequence of E=0kV/cm, 2kV/cm, 10kV/cm, and 0kV/cm (i.e., after removal of E) at 298K, respectively. For E=0kV/cm, only a single broad peak was found in the (002) scan, although a longitudinal

PMN-30%PT, E//(110), T=298K, beginning from ZFC

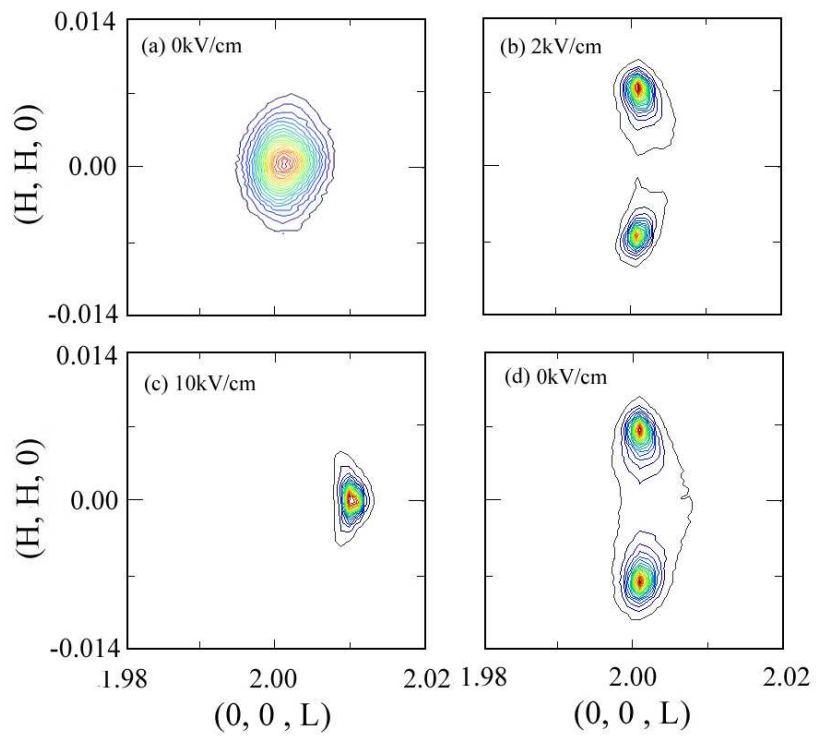


Figure 3.18 (002) mesh scans with increasing fields of (a) 0kV/cm, (b) 2kV/cm, (c) 10kV/cm, and (d) after removal of field in poled condition for PMN-0.30PT.

splitting was observed in (220) scan (data not shown). The results show that the R phase is stable in the ZFC condition, with a lattice parameter of $a_r=4.0220\text{\AA}$. Upon applying a field of 1kV/cm, a peak splitting was found to develop along the transverse direction in the (002) reflection, whereas the (220) scan only possessed a single peak (data not shown). These features are signatures of the monoclinic M_B/M_A phase. The lattice parameters, c_m and a_m , extracted from (002) and (220) reflections show that $a_m/\sqrt{2} > c_m$. Thus, we can conclude that the phase transformational sequence beginning from ZFC condition is $R \rightarrow M_B \rightarrow O$ with increasing E , with the $R \rightarrow M_B$ transition at $E < 1\text{kV/cm}$ and the $M_B \rightarrow O$ one near $E = 10\text{kV/cm}$.

Figure 3.19 shows the electric field dependence of the lattice parameters at 298K. With increasing E to 8kV/cm, the value of $a_m/\sqrt{2}$ and $b_m/\sqrt{2}$ can be seen to continuously increase, exhibiting a sharp increment at 9kV/cm; whereas, the value of c_m shows a gradual decrease and has a sharp decrease at 9kV/cm, at which point a single domain O phase is induced. Comparisons with the FC results in Figure 3.16(a) indicate that the crystal undergoes an abrupt transition to the O phase near 9kV/cm. It is also important to compare these results to recent studies of PMN-0.30PT with E along [110] crystals by Li and Viehland [68], which indicated an induced phase transformation, near this same field in the ZFC condition. It is relevant to note that an hysteretic P-E behavior was observed, whose remnant polarization was $\sim 0.24\text{C/m}^2$ (or $\frac{P_s}{\sqrt{3}}$) and whose value at the induced transition was $\sim 0.3\text{C/m}^2$ (or $\frac{P_s}{\sqrt{2}}$).

It appears that the polarization can near continuously rotate within the (110) plane of the M_B phase, from near the [111] direction to being in coincidence with the [110]. With decreasing electric field between 9kV/cm and 6kV/cm, the lattice parameters revealed hysteresis of the induced $M_B \rightarrow O$ transformation. For $E < 6\text{kV/cm}$, the orthorhombic phase did not remain stable, but rather a M_B phase was recovered. In addition, for $E < 6\text{kV/cm}$, the lattice parameters were equivalent between field increasing and decreasing sweeps. Upon removal of E , only a single domain was observed in the (220) scan, although a splitting along [220] was found in the (002) scan. We determined the monoclinic lattice parameters after removal of E and found that $a_m/\sqrt{2} > c_m$. These results show that the M_B phase is the ground state condition for

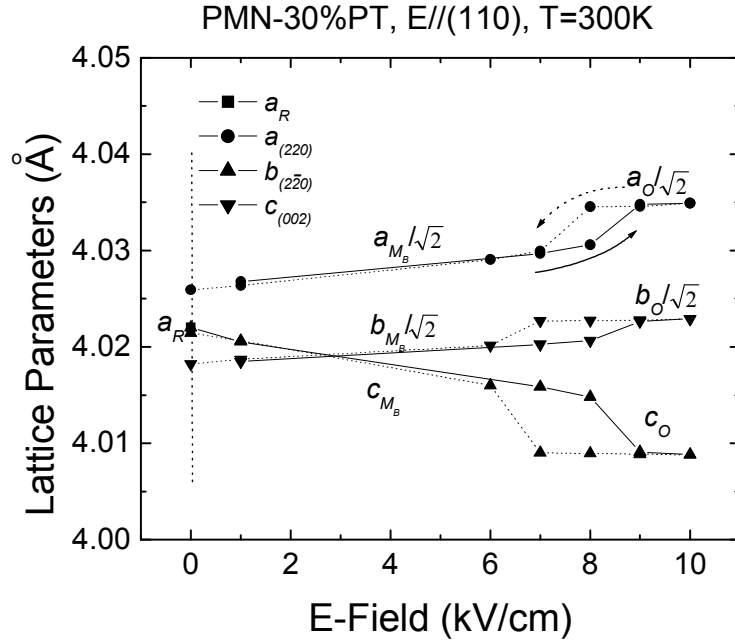


Figure 3.19 Electric-field dependence of the lattice parameters at 298K beginning from the ZFC condition, where lattice parameters $a_{(220)}/\sqrt{2}$, $b_{(220)}/\sqrt{2}$, and $c_{(002)}$ are plotted. Solid represent data obtained on field-increasing, whereas dotted lines field-decreasing. At $E=0\text{kV/cm}$, $c_{(002)}=a_R$; and once E is applied $a_{(220)}/\sqrt{2}$, $b_{(220)}/\sqrt{2}$ and $c_{(002)}$ correspond to $a_m/\sqrt{2}$, $b_m/\sqrt{2}$, and c_m in the M_B phase, and to $a_o/\sqrt{2}$, $b_o/\sqrt{2}$, and c_o in the O phase, respectively.

poled (110) crystals.

3.3.2 [111] electric field cooled PMN-xPT (x=0.30)

Next, I established the structural transformation sequence of PMN-0.30PT crystals with $E//[111]$. To obtain a comprehensive picture of the PMN-0.30PT structure properties in FC condition along [111], we took mesh scans around (002), (200), and (020) reflections at 393K, 353K and 323K as $E=2\text{kV/cm}$, as shown in Figure 3.20. In this study, the lattice parameters a , b , and c are those corresponding to that of primitive unit cell. Although not presented here, we obtained

- (a) the contour maps around (002), (200) and (020) scans At 450K. These scans revealed one peak. Analysis revealed a single lattice parameter, thus the structure is cubic with $a_c=4.022\text{\AA}$.
- (b) the (200) and (002) scans At 393K. Each exhibited a single peak, with different extracted lattice parameters of $a=4.018\text{\AA}$ and $c=4.031\text{\AA}$; whereas, the (020) scan exhibited a peak splitting along the longitudinal direction, with identical lattice constants. Please note that these values are quite close to those of c_t and a_t previously reported for [001] and [110] FC PMN-0.30PT. These results evidence that the structure is tetragonal; and that multiple domain configurations exist along the (020), (220) mesh scans. Table I shows these lattice parameters extracted from these mesh scans. Observations (c) and (d) that follow were made from these results.
- (c) the (002) and (020) reflections at 353K exhibited only one single peak, but the (200) reflection has the additional weak peak. The lattice parameters extracted from these reflections yield values of $a=b\approx 4.027\text{\AA}$ and $c\approx 4.014\text{\AA}$. In addition, two lattice parameters, 5.698\AA and 5.685\AA , were observed around (220) and (022) reflections (see Table I), which are very close to those of a_o and b_o of [110] FC PMN-0.30PT. Together, these results given the lattice parameters of the O phase: $a_o=5.698\text{\AA}$, $b_o=5.685\text{\AA}$, and $c_o=4.014\text{\AA}$.
- (d) all reflections exhibited only a single at 323K peak, from which I determined the two lattice parameters of $a=b\approx 4.023\text{\AA}$ and $c\approx 4.019\text{\AA}$. These scans from which these results were obtained are given in Figure 3.19 (g)-(i). The fact that $a=b\neq c$ rules out the

PMN-30%PT, E//[111], E=2kV/cm, FC

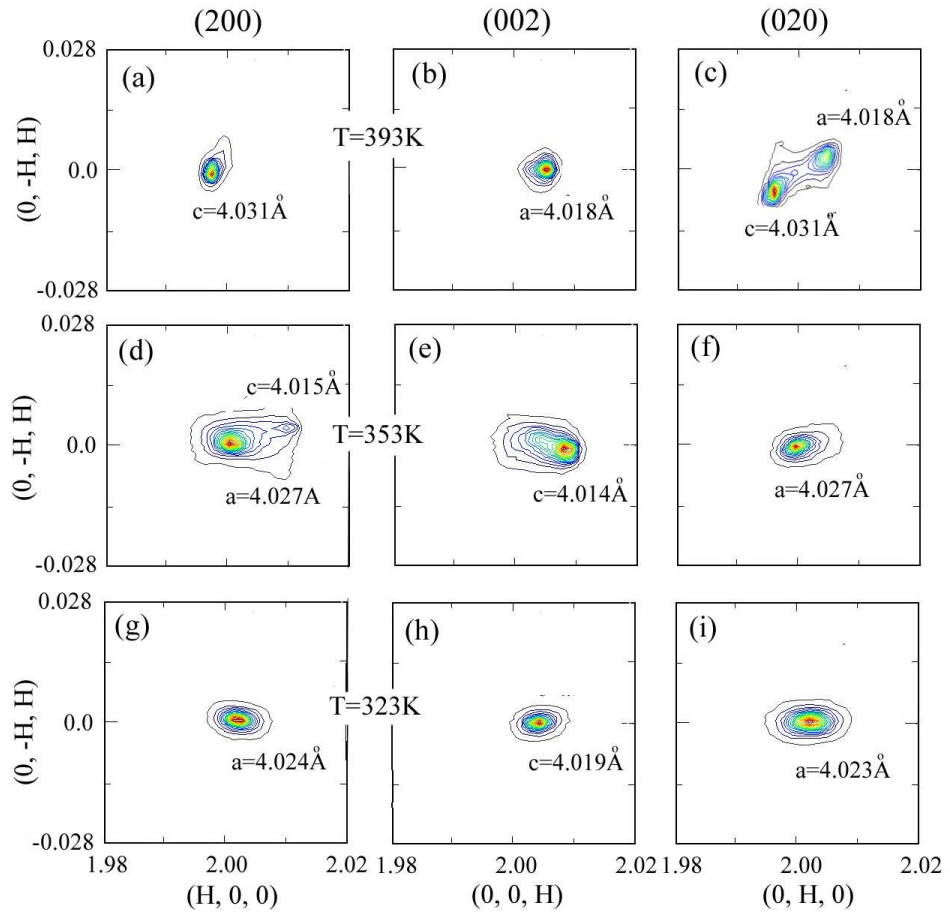


Figure 3.20 Mesh scans taken about the pseudocubic (200), (002) and (020) reflections for [111] electric field cooled PMN-0.30PT crystal with E=2kV/cm at 393K, 353K and 323K.

Table 3.1 PMN-0.30PT, E//(111), E=2kV/cm, FC

	T=393K (T)	T=353K (O)	T=313K (M _B)
(200)	$c_r=4.031\text{\AA}$	$a=4.027\text{\AA}, c=4.015\text{\AA}$	$a=4.024$
(220)	----	$a_o=5.699\text{\AA}, b_o=5.686\text{\AA}$	$a_m=5.695\text{\AA}, b_m=5.682\text{\AA}$
(002)	$a_r=4.018\text{\AA}$	$c=4.014\text{\AA}$	$c=4.019\text{\AA}$
(022)	----	$a_o=5.698\text{\AA}, b_o=5.685\text{\AA}$	$a_m=5.694\text{\AA}, b_m=5.682\text{\AA}$
(020)	$c_r=4.031\text{\AA}, a_r=4.018\text{\AA}$	$a=4.027\text{\AA}$	$a=4.023\text{\AA}$
(202)	----	---	---

possibility of the R phase although $E//[111]$ was thought to favor the R phase. The (220) and (022) reflections also only show two different values for the [110] inter-plane spacings of 5.695\AA and 5.682\AA (see Table I). These values are quite close to those of a_m , b_m and c_m that were previously reported for [110] FC PMN-0.30PT. In addition, the finding of equivalence around the (200) and (020) reflections indicates that the polarization is constrained to the (110) plane and that $a=b>c$, this confirms that this new phase is the as M_B one, instead of M_A , with $a_m=5.695\text{\AA}$, $b_m=5.682\text{\AA}$, $c_m=4.019\text{\AA}$.

To clarify the electric-field effects on the phase sequence, we determined the temperature dependence of the lattice parameters for PMN-0.30PT, as given in Figure 3.21. For comparison, the lattice parameters of the ZFC state are also shown. Above 410K, the lattice parameters of the (200), (002) and (020) reflections for in both the FC or ZFC conditions are quite similar, indicating that PMN-0.30PT has cubic symmetry. With decreasing temperature, the lattice behavior exhibited a very interesting feature: the (200) reflection becomes equivalent to the (020) one, which persists on cooling down to room temperature. Actually, the lattice parameters a and b of the primitive unit cell for O and M_A/M_B phases, have to be equal. It is worth noting that the value of a_t and c_t , both determined from (002) reflection, are continuous during the $T \rightarrow O$ transition, which was also found for [001] and [110] FC PMN-0.30PT. With further decrease of temperature the values of a and b continuously decreased, while c had a large increase at 343K: this is indicative of a polarization rotation along the pathway of $O \rightarrow R$. The finding of $a=b>c$ confirms the presence of the M_B phase, instead of R or M_A ones. These evidences unambiguously reveal that PMN-0.30PT has a sequence of $C \rightarrow T \rightarrow O \rightarrow M_B$ for $E//[111]$. In addition, comparison of [111] FC PMN-0.30PT to [001] and [110] FC ones also confirms the $C \rightarrow T \rightarrow O \rightarrow M_B$ sequence.

Table II lists the lattice parameters of the T, O and M phases for [001], [110] and [111] FC PMN-0.30PT. In Table II, slight differences between lattice parameters can be contributed to compositional fluctuation and different measurement conditions. In the [110] FC case, the lattice parameters for the limiting M_C phase ($a_{mc}=c_{mc} \approx 4.027\text{\AA}$, $\beta=90.130^\circ$) were obtained from the orthorhombic ones ($a_o=5.701\text{\AA}$ and $b_o=5.688\text{\AA}$), which were ($a=c \approx 4.027\text{\AA}$) for the [111] FC case. The lattice parameters b_{mc} , c_o and a_t in [001], [110] and [111] FC states, have been

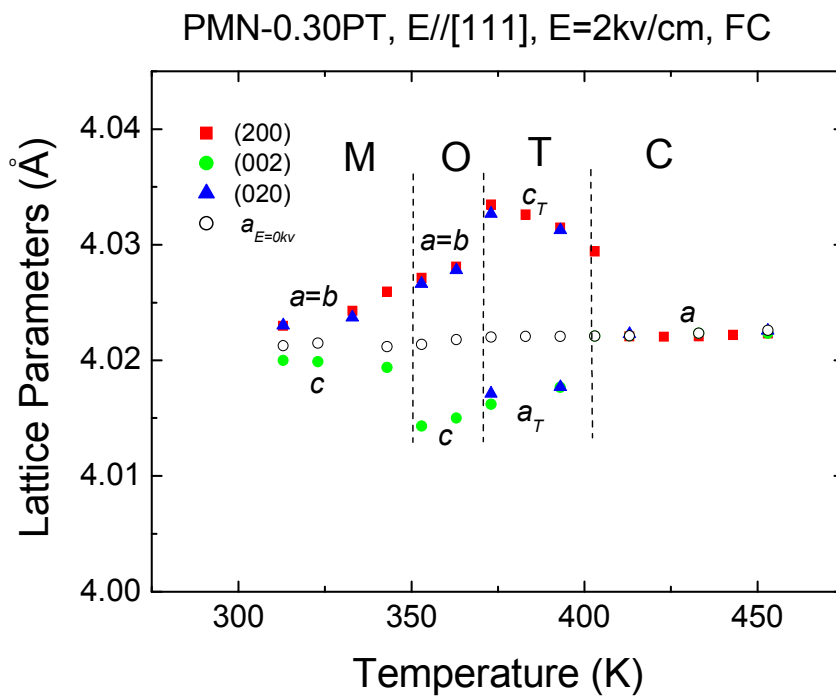


Figure 3.21 Lattice parameters as a function of temperature for a [111] electric field cooled PMN-0.30PT crystal with E=2kV/cm.

Table 3.2 PMN-0.30PT, FC

	393K	353K	313K
(001)	$a_i=4.017\text{\AA}$, $c_i=4.033\text{\AA}$	$c_{mc}=4.029\text{\AA}$, $a_{mc}=4.025\text{\AA}$ $b_{mc}=4.012\text{\AA}$, $\beta=90.07^\circ$	$a_{ma}=5.692\text{\AA}$, $b_{ma}=5.681\text{\AA}$ $c_{ma}=4.025\text{\AA}$, $\beta=89.96^\circ$
(110)	$a_i=4.016\text{\AA}$ $c_i=4.031\text{\AA}$	$a_o=5.701\text{\AA}$, $b_o=5.688\text{\AA}$ $c_o=4.012\text{\AA}$	$a_{mb}=5.696\text{\AA}$, $b_{mb}=5.682\text{\AA}$ $c_{mb}=4.019\text{\AA}$, $\beta=89.85^\circ$
(111)	$a_i=4.018\text{\AA}$ $c_i=4.031\text{\AA}$	$a_o=5.698\text{\AA}$, $b_o=5.686\text{\AA}$ $a=b=4.027\text{\AA}$, $c=4.014\text{\AA}$	$a_{mb}=5.695\text{\AA}$, $b_{mb}=5.682\text{\AA}$ $a=b=4.023\text{\AA}$, $c=4.019\text{\AA}$

*a) (001) and (110): E=1kV/cm; (111): E=2kV/cm

b) In (111)-fielded case, lattice parameters, a , b , and c are with respect to the primitive cubic unit cell.

c) For (110)-fielded case, the O is the limiting case of M_C with $a_{Mc}=c_{Mc}=4.027\text{\AA}$, $b_{Mc}=4.012\text{\AA}$, $\beta=90.13^\circ$ at 353K.

found to be quite close to each other, corresponding to the unique axis b_m of M_C . It also has been found that β in the limiting M_C phase for [110] ($\beta=90.13^\circ$) and [111] ($\beta=90.12^\circ$) FC cases is larger than that of the [001] one ($\beta=90.07^\circ$). Therefore, the phase observed at 353K in [111] state is definitely orthorhombic. Similarly, the phase observed at 313K in the [111] FC state can be confirmed to be M_B phase. If we take the lattice parameters of ($a_{mb}=5.696\text{\AA}$ and $b_{mb}=5.682\text{\AA}$) for the [110] FC state, we can get ($a=b\approx 4.023\text{\AA}$, $\beta=90.140^\circ$), which are quite consistent with those of the [111] FC state. Prior x-ray diffraction has shown that PMN-0.30PT has a R phase at low temperature. The rhombohedral phase is easily stabilized by electric-field poling along the [111] direction. Investigations on PZN-0.08PT and PMN-0.33PT by polarized light microscopy have evidenced the R phase as $E//[111]$. However, our results reveal that PMN-0.30PT has a M_B -type phase with $a=b>c$ in FC condition. Furthermore, this phase still processes the M_B -type symmetry even with increasing electric field applied along [111] beginning from an initial R state, as shown in Figure 3.22. This figure shows the lattice parameters for PMN-0.30PT as a function of electric field along [111] at (a) 353K and (b) 313K, respectively. In the zero field condition, the lattice parameters around the (200), (020) and (002) reflections have been found to be equal. However, with increasing E, the lattice parameters a around the (200) reflection and b around the (020) one become equivalent, and both of which are larger than c around the (002) reflection. Furthermore, the difference between a and c gradually increases with increasing E. Application of $E//[111]$ should not uniquely fix any particular {002} direction – as the (200), (002), and (200) reflections are 3-fold symmetric about the [111]. However, as we have shown in those mesh scans above, the (002) reflection is preferred, having important consequences upon the transformational sequence in the [111] field-cooled condition. The O phase, observed as single domain-like state, bridges the T and M_B phases. If decomposing $E//[111]$ as three components $E_{[100]}$, $E_{[010]}$ and $E_{[001]}$ it could be seen that two components of $E_{[100]}$, $E_{[010]}$ play the similar role as $E//[110]$, where the single domain O phase is induced. Then the third component of $E_{[001]}$ results in the polarization rotation following the path $O\rightarrow R$, which is M_B . It is more likely that the strain induced by E plays an important role, resulting in an anisotropy of the crystal lattice, where the redistribution of strain inside of the crystal for $E//[111]$ results in a macroscopic M_B phase.

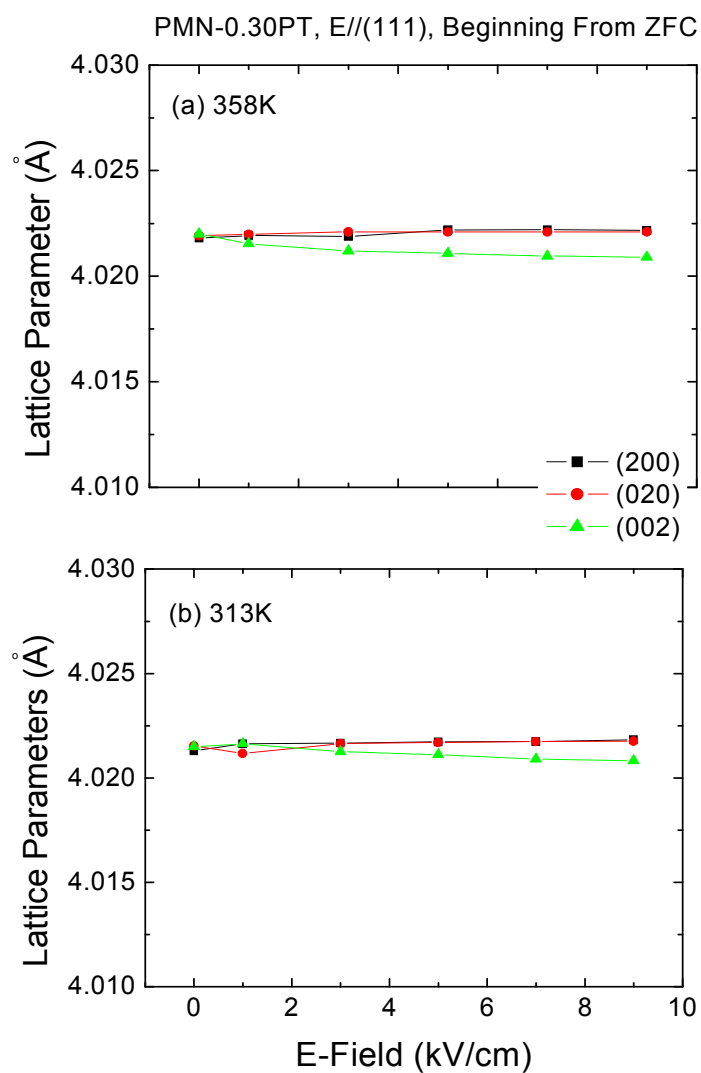


Figure 3.22 Electric-field dependence of the lattice parameters for PMN-0.30PT with E//[111] beginning from the ZFC (R) phase taken at (a) 358K, and (b) 313K. These lattice parameters correspond to those of the primitive unit cell.

3.4 PMN-xPT

3.4.1 [001] electric field cooled PMN-xPT

Figure 3.23 shows the temperature evolution of the lattice parameters for [001] FC PMN-xPT crystals whose composition is to the left of the MPB: $x=0.15, 0.24, 0.27,$ and 0.28 . Previously, we have reported those for compositions near and to the right of MPB, please see the reference given for the respective composition: $x=0.30, 0.32,$ and 0.35 .

For PMN-0.15PT and PMN-0.24PT, only a single phase transition was observed on cooling under a field of $E=0.5\text{kV/cm}$. However, there was an important difference between the temperature evolutions of the lattice parameters for these two compositions. Specifically for $x=0.15$, we observed the lattice parameter $a_m/\sqrt{2}$ to be notably larger than that of c_m ; whereas for $x=0.24$, we found $a_m/\sqrt{2} < c_m$, where on cooling the value of $a_m/\sqrt{2}$ approached that of c_m . Diffraction results then confirmed that these two crystals had identical domain configurations in their low temperature phases, belonging to the Cm space group. Using the values of $a_m/\sqrt{2}c_m$ and β , we conclude that both PMN-0.15PT and PMN-0.24PT have monoclinic M_A structure (please see Section 5.2). For PMN-0.27PT and PMN-0.28PT, two phase transitions were observed on electric field cooling with the sequence $C \rightarrow T \rightarrow M_A$. In addition, we observed for both crystals that the lattice parameter $a_m/\sqrt{2}$ increased with decreasing temperature, approaching that of c_m . The principle difference between the results with increasing PT content in this range was that the field required to stabilize the T phase on cooling was reduced with increasing x : $E=0.50\text{kV/cm}$ for $x=0.27$, but $E=0.25\text{kV/cm}$ for $x=0.28$. For $x \geq 0.3$, M_C is the dominant monoclinic phase, as the composition enters the region of the MPB: the transformational sequence for $x=0.30$ is $C \rightarrow T \rightarrow M_C \rightarrow M_A$, whereas that for $x=0.32$ and 0.35 is $C \rightarrow T \rightarrow M_C$. For $x \geq 0.38$, the T phase was stable down to 243K , with a transformational sequence of simply $C \rightarrow T$.

Next, we measured changes in mesh scans with increasing x in the [001] FC condition. Figure 3.24 shows a partial summary of the many measurements made at lower temperatures for various PMN-xPT compositions across the phase diagram. The mesh scans of the low

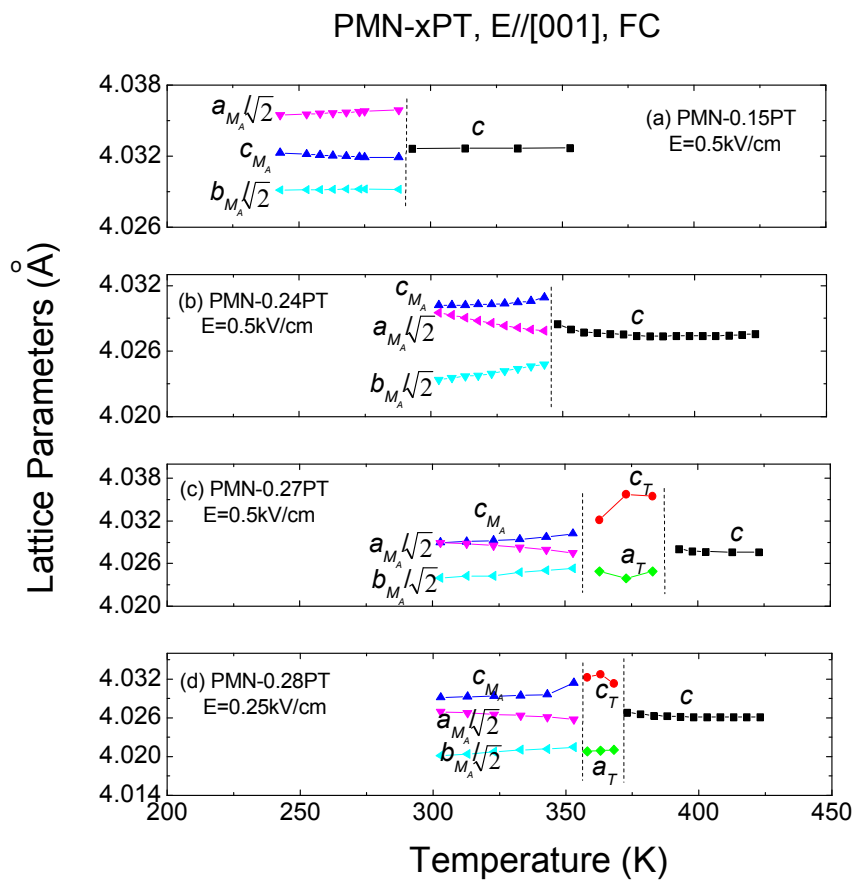


Figure 3.23 Lattice parameters as a function of temperature for [001] field cooled PMN-xPT crystals: (a) PMN-0.15PT, E=0.5kV/cm; (b) PMN-0.24PT, E=0.5kV/cm; (c) PMN-0.27PT, E=0.5kV/cm; and (d) PMN-0.28PT under E=0.25kV/cm.

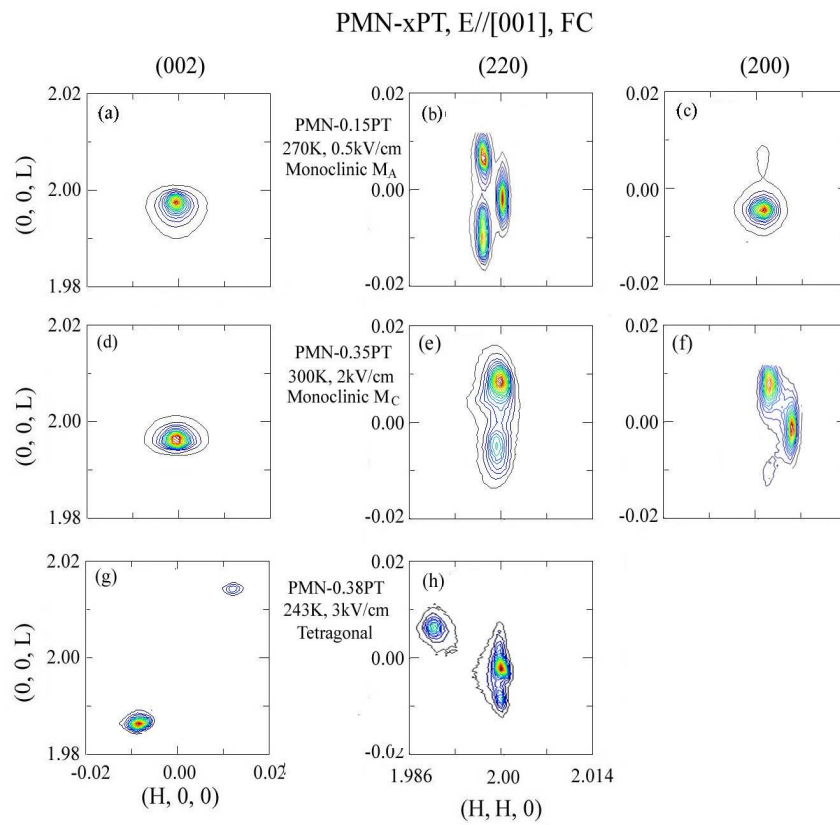


Figure 3.24 Mesh scans taken about the pseudocubic (002), (220) and (200) reflections for [001] field cooled PMN-xPT crystals: (a) PMN-0.15PT, $E=0.5\text{kV/cm}$ at 270K; (b) PMN-0.35PT, $E=2\text{kV/cm}$ at 300K; and (c) PMN-0.38PT, $E=3\text{kV/cm}$ at 243K.

temperature phase with $0.15 \leq x \leq 0.30$ were consistent with the known signatures for the M_A phase; whereas, those with $0.32 \leq x \leq 0.35$ for the M_C phase. Mesh scans at various temperatures confirmed signatures of the phase transformational sequences noted above for the various compositions. Our findings for [001] PMN-xPT are summarized in the phase diagram given in Fig. 3.1(a), above. The [001] FC transformational sequence was $C \rightarrow M_A$ for $x < 0.25$, $C \rightarrow T \rightarrow M_A$ for $0.25 \leq x \leq 0.30$; $C \rightarrow T \rightarrow M_C$ for $0.30 \leq x \leq 0.35$; and $C \rightarrow T$ for $x > 0.35$. Based on lattice parameter studies, we found that the intermediate T phase extends to $x=0.25$ in the FC condition, rather than $x=0.30$ as for the ZFC condition. Previous reports of dielectric relaxation in the temperature range of this extended T phase indicate that microdomains of tetragonal symmetry may be stabilized by application of $E//[001]$ over a narrow phase region, on cooling from the cubic to M_A phases. This possibility is further substantiated by the observation that the $C \rightarrow T$ boundary as determined by structural data ($c > a$) was found to shift to higher temperatures with increasing field for $E < 3\text{kV/cm}$, whereas the $C' \rightarrow T$ boundary determined by the dielectric maximum was independent of E .

3.4.2 (110) electric field cooled PMN-xPT

Figure 3.25 shows the temperature evolution of the lattice parameter for [110] FC PMN-xPT with $x=0.15, 0.22, 0.28, 0.30,$ and 0.35 . For $0.15 \leq x \leq 0.20$, a single phase transition was observed on cooling under $E=0.5\text{kV/cm}$. Structural analysis confirmed that the low temperature phase had a M_B lattice symmetry, with $a_m/\sqrt{2} > c_m$; and thus, the transformational sequence on cooling is $C \rightarrow M_B$. Temperature dependent lattice parameter studies revealed that the difference between $a_m/\sqrt{2}$ and c_m gradually increased with decreasing temperature in the M_B phase field, contrary to the observed increase in the M_A phase field from the [001] FC measurements. For $0.22 < x < 0.28$, two phase transitions were observed on field cooling. Structural analysis revealed the transformational sequence to be $C \rightarrow O \rightarrow M_B$: no intermediate T phase was found to extend to lower PT contents under E , rather a single domain O phase was found in its place. For $x=0.22$, coexistence of O and M_B phases was observed under $E \leq 1.0\text{kV/cm}$, but with increasing field to $E=2\text{kV/cm}$ such coexistence was not found. With increasing x between 0.22 and 0.28 , the field required to

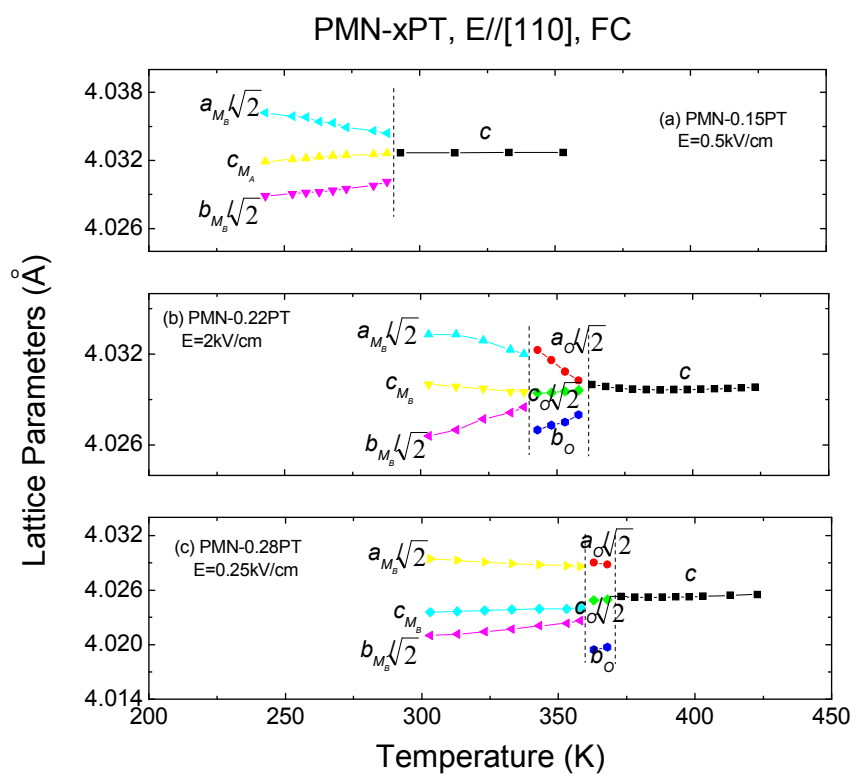


Figure 3.25 Lattice parameters as a function of temperature for [110] field cooled PMN-xPT crystals: (a) PMN-0.15PT, $E=0.5\text{kv/cm}$; (b) PMN-0.22PT, $E=2\text{kv/cm}$; and (c) PMN-0.28PT, $E=0.25\text{kv/cm}$

stabilize the O phase on cooling was found to be decreased. For $0.30 \leq x \leq 0.35$, an intermediate T phase was found, similar to that in the ZFC condition. Over a narrow compositional range near $x \approx 0.30$, the transformational sequence was found to be $C \rightarrow T \rightarrow O \rightarrow M_B$; whereas for $x=0.32$ and 0.35 , we found the sequence to be $C \rightarrow T \rightarrow O$. For $x > 0.32$, the T phase was found to become increasingly dominate with increasing x ; until for $x=0.38$, the sequence was simply $C \rightarrow T$. Next, we also measured changes in mesh scans of PMN-xPT ($x=0.15, 0.35, 0.38$) at low temperatures in the [110] FC condition, as shown in Figure 3.26. Results from one crystal are shown here, which reveals the signatures of both the M_B and O phases. We illustrate the signatures of the M_B phase using results for $x=0.15$ as shown in Figure 3.26(a)-(c). At 253K, the (220) reflection reveals a single peak, indicating that $E//[110]$ fixes the [110] crystallographic direction of the crystal: two peaks about the (002) reflection were found, which were split along the transverse direction L; and the $(\bar{2}20)$ reflection and (200) reflection (not shown) also revealed a single peak. The combination of these mesh scans provides the signatures of M_B : two polarization vectors constrained to the (110) plane that lie close to the [110]. A similar M_B lattice structure was found for $x=0.22, 0.28, \text{ and } 0.30$ at low temperatures. The signature of the O phase is illustrated in Figures 6 (d)-(f) for $x=0.35$, taken at 300K in the FC condition with $E=2\text{kV/cm}$. All mesh scans taken about the (220), $(\bar{2}20)$, (002), and (200) reflections revealed a single peak-demonstrating that a single domain O phase has been induced. For $x=0.38$, the domain configurations as shown in Figure 3.26 (g) and (h), show that the T phase remains stable on cooling to 243K as $E=3\text{kV/cm}$.

Our findings are summarized in Figure 3.1 (a) and (b). The dotted lines and open phase extends to $x=25$ in the FC condition, rather than $x=0.30$ as for the ZFC condition. Compared to the [001] FC phase diagram, in the [110] phase diagram, an extended O phase replaces the T and M_C phases, and a M_B phase replaces the M_A phase.

3.5. Discussion and summary

3.5.1 Fragile phase instability-a comparison of results

Our findings for [110] PMN-xPT are summarized in the phase diagram given in Figure

PMN-xPT, E//[110], FC

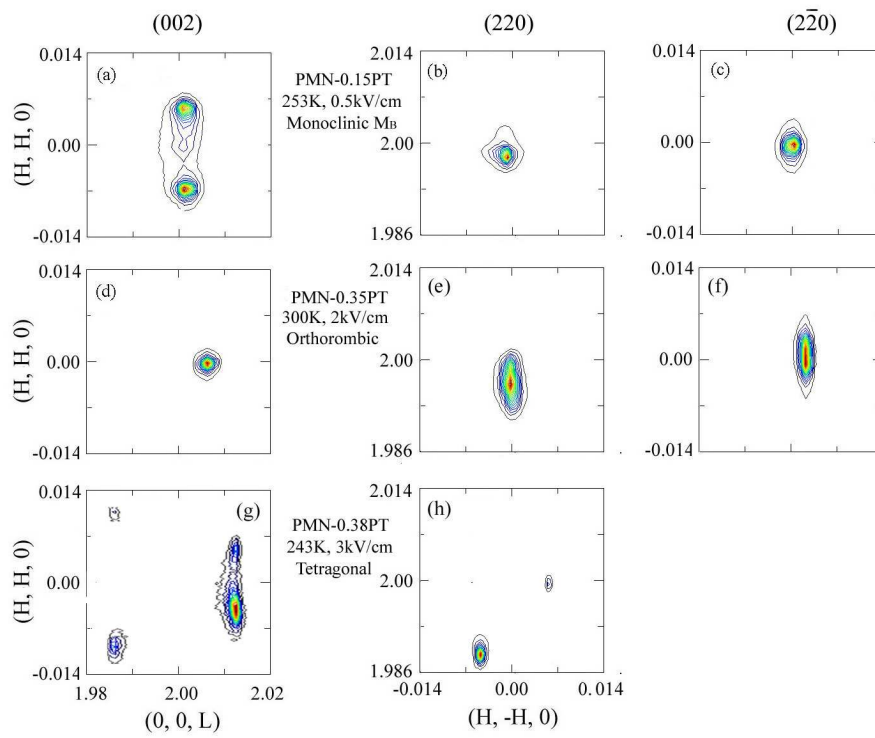


Figure 3.26 Mesh scans taken about the pseudocubic (002), (220) and (200) reflections for [110] field cooled PMN-xPT crystals: (a) PMN-0.15PT, E=0.5kV/cm at 253K; (b) PMN-0.35PT, E=2kV/cm at 300K; and (c) PMN-0.38PT, E=3kV/cm at 243K.

3.1(b) at the beginning of this chapter. The [110] FC transformational sequence was $C \rightarrow M_B$ for $x \leq 0.20$, $C \rightarrow O \rightarrow M_B$ for $0.22 \leq x < 0.30$; $C \rightarrow T \rightarrow O \rightarrow M_B$ for $x \approx 0.30$; $C \rightarrow T \rightarrow O$ for $0.31 < x \leq 0.36$; and $C \rightarrow T$ for $x > 0.37$. The intermediate T square signs were based on prior studies by Noheda *et al.* [22]. The bracketed italic R and M_C signs represents the rhomboheral and monoclinic phases of the zero-field-cooled condition. The solid square signs represent the temperature of the dielectric maximum (T_m) in ZFC condition. The solid circle signs represent the temperature of the phase transition in the FC condition determined by x-ray diffraction in this study.

Comparison of the [001] and [110] FC phase diagrams of PMN-xPT in Fig. 3.1 reveals several interesting findings, including: (i) that the R phase of the ZFC state is replaced by M_A in the [001] FC diagram, but with M_B in the [110] FC; (ii) a region (C') of abnormal thermal expansion above the dielectric maximum, whose stability range extended to higher temperatures by application of E; (iii) that the M_C phase in the [001] FC diagram is replaced by the O phase in the [110] FC; and (iv) that the stability of the T phase is extended to $x=0.25$ in the [001] FC diagram, whereas this extended T phase region is entirely replaced by the O phase in the [110] FC.

It is important to note that differences between the [001] and [110] phase diagrams was caused by moderate electric fields of $0.2 \leq E \leq 0.5 \text{ kV/cm}$ – clearly demonstrating that the phase stability of PMN-xPT crystals is quite fragile, or simply put many phases are apparently very close to being energetically degenerate. This phase fragility brings into question conventional wisdoms concerning the thermodynamics of classical phase diagrams – indicating an important role of an underlying structural heterogeneity.

3.5.2 The M_A and M_B phases

The M_A and M_B phases belong to the same group Cm ; accordingly, their mesh scans exhibit identical contour features. However, it is not easy to distinguish these two phases in experiments. For M_A phase, $P_x = P_y < P_z$; where as for M_B phase, $P_x = P_y > P_z$. In structural measurements, comparing P_x , P_y , and P_z is not always straight-forward. Here we discuss a robust but easy-to-use criterion that can be applied to structural measurements.

A schematic for the M_A/M_B phases is shown in Figure 3.27. It shows the plane defined by the [110] and [001] vectors. In both monoclinic phases, [110] (a_m) is tilted up toward [001] (c_m), and the length of a_m and c_m also deviates from those in the cubic phase (in the cubic phase, $a_m = \sqrt{2}a = \sqrt{2}c$). Therefore, the ratio $a_m/\sqrt{2}c_m$ and the monoclinic angle β between a_m and c_m are the only two parameters necessary to define a M_A/M_B phase. For a monoclinic phase with a fixed monoclinic angle β , the polarization components (P_x, P_y, P_z) are exclusively determined by the ratio $a_m/\sqrt{2}c_m$. The phase is M_A if the polarization falls closer to the [001] direction (T), M_B if the polarization falls closer to the [110] direction (O). The point in between M_A and M_B is therefore the one that has $P_x=P_y=P_z$, which is a R.

This provides a definitive way to distinguish M_A and M_B based on β and $a_m/\sqrt{2}c_m$. When we have a M_A/M_B type structure, we should compare the ratio $a_m/\sqrt{2}c_m$ to that of the rhombohedral phase, which has the same angle β between its [001] and [110] vectors. For example, for a rhombohedral phase with rhombohedral angle α^* (angle between [001] and [100]), the ratio $a_m^*/\sqrt{2}c_m^*$ (here a_m^* denotes the length along [110] direction) is $\sqrt{2} \cos(\alpha^*/2)$, while α^* also has to satisfy $\cos(\beta) = (1 - 2\sin^2(\alpha^*/2)) / \cos(\alpha^*/2)$ for the angle between [001] and [110] to be β . If $a_m/\sqrt{2}c_m$ from our measurements is greater than $\sqrt{2} \cos(\alpha^*/2)$, we have a M_B phase, otherwise we have a M_A phase. Since for most cases in lead perovskite relaxors, α and β are very close to 90° degrees, $\sqrt{2} \cos(\alpha^*/2)$ is close to 1. In practice, people usually can compare $a_m/\sqrt{2}c_m$ to 1 to determine whether the structure is a M_A or M_B phase. However, when $a_m/\sqrt{2}c_m$ is close to 1, the method described here should be used.

Table III shows calculated values of $a_m/\sqrt{2}c_m$ and $\sqrt{2} \cos(\alpha^*/2)$ for [001] and [110] FC PMN-xPT. Using this table, we can identify the polarization rotation pathway. For [001] FC PMN-0.15PT, it was found that $a_m/\sqrt{2} > c_m$ over the entire phase field of the low temperature phase. Thus, we can conclude that the polarization is constrained to the

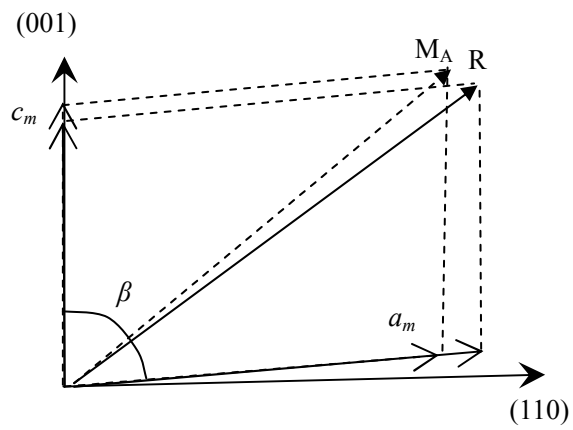


Figure 3.27 Polarization vectors of the rhombohedral (R) and monoclinic M_A (*Cm*) phases, represented with same monoclinic angle β in the HHL zone of reciprocal space. The R unit cell can be expressed in terms of a monoclinic one by: $a_m=2a_r\cos(\alpha/2)$, $b_m=2a_r\sin(\alpha/2)$, $a_m=a_r$, $\cos(\beta)=(1-2\sin^2(\alpha/2))/\cos(\alpha/2)$, where a_r and α are the *R3m* cell parameters.

Table 3.3 Calculated value of $a_m/\sqrt{2}$ and $\sqrt{2} \cos(\alpha^*/2)$ for low temperature phases in [001] and [110] electric field cooled PMN-*x*PT crystals. β , $a_m/\sqrt{2}$ and c_m were directly derived from the experiments and the imaginary rhombohedral angle α^* was determined according to $\cos(\beta)=(1-2\sin^2(\alpha^*/2))/\cos(\alpha^*/2)$.

<i>x</i>	T(K)	E(kV/cm)	$a_m/\sqrt{2}$ (Å)	c_m (Å)	β (°)	α^* (°)	$a_m/(\sqrt{2}c_m)$	$\sqrt{2} \cos(\alpha^*/2)$	$a_m/2c_m \cos(\alpha^*/2)$	<i>S</i>
E//[001]										
0.30	300	1.0	4.0245	4.0242	89.950	89.965	1.0001	1.0003	0.9998	M _A
0.28	353	0.25	4.0258	4.0314	89.895	89.965	0.9986	1.0007	0.9979	M _A
0.27	300	0.35	4.0299	4.0280	89.850	89.894	1.0005	1.0010	0.9995	M _A
0.24	300	0.5	4.0295	4.0302	89.870	89.908	0.9998	1.0008	0.9990	M _A
0.15	270	0.5	4.0348	4.0319	89.885	89.917	1.0007	1.0008	0.9999	M _A
E//[110]										
0.30	300	1.0	4.0280	4.0200	89.850	89.894	1.0020	1.0010	1.0009	M _B
0.28	353	0.25	4.0287	4.0240	89.900	89.929	1.0012	1.0006	1.0006	M _B
0.22	333	2.0	4.0322	4.0295	89.920	89.945	1.0007	1.0005	1.0002	M _B
0.15	243	0.5	4.0368	4.0319	89.853	89.897	1.0012	1.0009	1.0003	M _B

R→T path of the M_A phase, and it is not possible that it would follow the R→O one of M_B . However, for [110] FC PMN-xPT with $0.15 < x < 0.3$, it was found that $a_m / \sqrt{2}c_m > \sqrt{2} \cos(\alpha^*/2)$ over the entire phase field of the low temperature phase, demonstrating that polarization rotation occurs towards [110] away from [111], following the path R→O of the M_B phase. We note several other important points. For $x=0.15$, the difference between $a_m / \sqrt{2}c_m$ and $\sqrt{2} \cos(\alpha^*/2)$ is very small, demonstrating that the polarization vector lies quite close to [111]. Second for [001] FC PMN-xPT with $0.24 \leq x \leq 0.27$, we observed that the value of $a_m / \sqrt{2}$ approaches that of c_m with decreasing temperature. This demonstrates that the polarization of the M_A phase gradually rotates back on cooling towards [111] away from the [001].

3.5.3 The C' phase

Both the [001] and [110] phase diagrams of PMN-xPT exhibited a region of abnormal thermal expansion, designated as C'. In this region the lattice parameter c derived from the (002) reflection was found not to be equal to that of a derived from the (200) reflection. In addition, it was observed that the stability of the C' phase was extended to higher temperatures following application of E . As an example, Figure 3.28 shows the temperature dependence of the lattice parameters derived from the (002) reflection for PMN-0.28PT in the FC state at various fields for (a) $E//[001]$, and (b) $E//[110]$. Both figures show that the region of $c/a > 1$ extends to higher temperatures with increasing E . Please note for $E=2\text{kV/cm}$ that the lattice parameters changed continuously with decreasing temperature, rather than exhibiting an abrupt anomaly as for $E=0.25\text{kV/cm}$.

We are careful to distinguish the boundary C' from that of the true cubic C: C was determined from the Curie temperature (T_C) of the dielectric maximum, whereas C' from the temperature at which c/a first deviated from one. Thus, in the phase field C', we have tetragonal splitting that occurs above the temperature of the dielectric maximum. This is unconventional with respect to normal phase transitions: where symmetry breaking occurs at or below T_C , but never above. Rather, it has some similarities to relaxor ferroelectric behavior in PMN, where local polarizations are known to exist above the dielectric maximum.

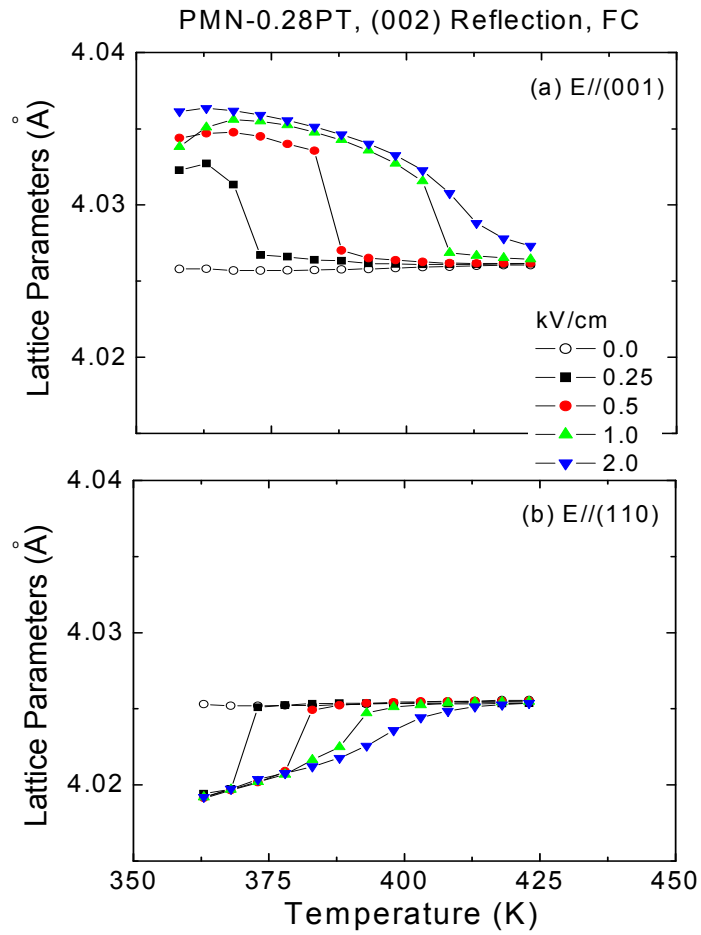


Figure 3.28 Lattice parameter as a function of temperature derived from the (002)-reflection of PMN-0.28PT under different electric field levels applied along: (a) $E//[001]$, and (b) $E//[110]$.

Accordingly, we attribute this anomalous phase field C' to polar nano-regions (PNRs). However, there are important differences between the phase field C' and a relaxor state. Relaxors are well-known to have a pseudo-cubic structure. The averaging over PNRs that are randomly distributed amongst all possible domain variants on a nanometer length scale yields a cubic structure on average. However, in the phase field C', under E//[001] or E//[110], the PNRs will be partially aligned under the direction of the applied E. Thus, the local structural asymmetric distortions of the PNRs will not be averaged to cubic, rather an ensemble of PNRs will exhibit a net distortion. Accordingly, a symmetry breaking above T_C may be observed, which gradually changes with E and temperature as the topological arrangement of PNRs is altered.

Here, we consider the structural evolution from the cubic to ferroelectric state to occur in three steps. First, near T_B (Burns temperature), clusters of short-range polar order (i.e. PNR's) develop and gradually increase in number on cooling. Second, with decreasing temperature, the ensemble of PNR's becomes percolating, resulting in the development of microdomains. However, since these micro-domains are on a scale much smaller than the x-ray coherence length, only a slight broadening of the Bragg reflections is observed. This evolution is believed to be continuous and the dielectric behavior correspondingly varies smoothly on cooling. Third, below a temperature that we designate as T_m , a thermally activated formation of critical ferroelectric nuclei occurs from the microdomain state – below which point, a long-range ordered ferroelectric phase is stable. Application of field assists in aligning the PNR along the direction that E is applied, resulting in PNR growth and an increase in its numbers, giving rise to the abnormal thermal expansion above T_C that defines the C' phase field. Higher fields favor PNR growth at higher temperature; and correspondingly, the C'→C phase boundary is shifted to higher temperature with increasing E.

It is worth noting that the stability range of the C' phase field was extremely narrow when the stable low temperature phase was tetragonal in both the [001] and [110] phase diagrams. The C' phase field widens significantly with increasing E only in the region where the transformational sequence was altered by changing the direction along which E was applied. The most pronounced changes were found for $x \approx 0.30$ where the sequence was

$C \rightarrow C' \rightarrow T \rightarrow M_C \rightarrow M_A$ for $E//[001]$, but $C \rightarrow C' \rightarrow T \rightarrow O \rightarrow M_B$ for $E//[110]$. These observations suggest that the fragileness of the phase stability might be related to the structural inhomogeneity originating from the PNR state. Recent experiments on PZN-xPT relaxor systems suggest that an external electric field along [111] direction actually enhances PNR with polarizations perpendicular to, instead of along the external field in the rhombohedral phase. Although the implications of these results on our [001] and [110] electric field measurements are not yet clear, they do indicate that the field can greatly affect the PNR configuration, and therefore the structural inhomogeneity.

3.5.4 Extension of T and/or O phase fields to lower x by E

In the ZFC phase diagram of PMN-xPT, the T phase extends only to $x=0.30$; and for $x < 0.30$, a $C \rightarrow R$ sequence is found on cooling. For the [001] FC crystals, the T phase was extended to $x=0.25$, and could be induced by fields as small as $E=0.25\text{kV/cm}$ for $x=0.28$. However, for the [110] FC crystals, the region where the T phase was extended was entirely replaced by the O phase.

Following the phase diagrams in Figure 3.1, it can be noted that the M_C/O phases are closely related to the presence of a stable T phase, whereas M_A/M_B are always connected to R. Thus, we can conclude that for compositions on the left side of the MPB ($x < 0.30$), the polarization rotation pathway is $R \rightarrow M_A \rightarrow T$ for $E//[001]$ and $R \rightarrow M_B \rightarrow O$ for $E//[110]$ with increasing E beginning from the ZFC condition; and that for compositions inside of the MPB ($0.30 < x \leq 0.35$), the path is $M_C \rightarrow T$ for $E//[001]$, but $M_C \rightarrow O$ for $E//[110]$. A special case occurs for PMN-0.30PT: the rotational pathway is $R \rightarrow M_A \rightarrow M_C \rightarrow T$ with increasing E from the ZFC, due to a monoclinic M_A to M_C transition.

In the PMN-xPT crystalline solution, the substitution of the octahedron $[\text{TiO}_4]^{4-}$ for the more complex $[\text{Mg}_{1/2}\text{Nb}_{2/3}\text{O}_4]^{4-}$ one, between relaxor PMN and ferroelectric PT, results in a MPB separating ferroelectric R and T phase. In the T phase field, the tetragonal splitting is known to be weakened with decreasing x [21, 69]. For $x=0.30$ in the ZFC condition, the T phase is only observed over a narrow range of temperatures; furthermore, relaxor ferroelectric behavior has been reported in ZFC crystals for $x \leq 0.30$. Thus, PMN-0.30PT can be

considered as a special composition in the phase diagram, where a gradual transition between microdomains of the T phase and a macroscopic T phase begins to occur. We note that microdomains have been observed by electron microscopy for $0 < x < 0.30$ [70]. Since these microdomains are much smaller than the coherence length of x-rays, the structure appears cubic below T_m in the ZFC state. However, in the FC state, the microdomains align along the direction that E is applied. Thus, an extended macroscopic T phase is observed to be sandwiched between the C and M_A ones on cooling for $0.25 \leq x < 0.30$, whose c/a ratio can be significantly altered by E. However, more thought is required to understand the presence of microdomains and intermediate orthorhombic and monoclinic phases.

3.5.5 A possible explanation for the Fragility: micro-domain averaging

Let us consider an insight which might help explain the origin of fragile phase stability. Consider for example PMN-0.28PT, T and O phases were found in the same temperature range for E//[001] and E//[110] respectively, under fields as small as $E=0.25\text{kV/cm}$. However, comparison of the lattice parameters of the T and O phases (at the same temperature) reveals an interesting feature: $a_t \approx b_o \approx 4.020\text{\AA}$ and $a_o / \sqrt{2} + c_o / \sqrt{2} = a_t + c_t \approx 8.049\text{\AA}$ (365K). Similar observations were made at other temperatures and for $x=0.30$ and 0.35 . Since the O phase is the limiting case of the M_C one, we observed an equally important relationship between the lattice parameters of the T and M_C phases for $x=0.30, 0.32, 0.35$: $b_m = a_t$, and $a_m + c_m = a_t + c_t$ where $a_m, b_m,$ and c_m are the lattice parameters of the M_C unit cell. These observations demonstrate the existence of an important crystallographic relationship/transformation between the T, O, and M_C phases – they are not independent of each other.

Recently, a theory of an adaptive ferroelectric phase [19, 20] has been developed to predict the microdomain-averaged crystal lattice parameters of a structurally inhomogeneous state, consisting of tetragonal microdomains. This theory predicts crystallographic relationships between T and M_C phases of

$$a_m + c_m = a_t + c_t \quad (1a)$$

$$b_m = a_t; \quad (1b)$$

which have been experimental verified for PMN-xPT and PZN-xPT. Recently, Wang *et al.* [36] have extended this analysis, obtaining a relationship between the monoclinic angle (β) and the tetragonal/monoclinic lattice parameters, given as

$$\beta = 90^\circ + 2A\omega(1-\omega)\left(\tan^{-1}\frac{c_t}{a_t} - 45^\circ\right); \quad (1c)$$

where $\omega = \frac{c_m - b_m}{a_m + c_m - 2b_m}$, $a_t = b_m$, $c_t = a_m + c_m - b_m$, and the constant $A \approx 1$. Furthermore, we note that the O phase is a limiting case of M_C , where $\omega = 1/2$.

The predictions of (1) are identical to the experimentally observed relationship between the T, O, and M_C lattice parameters that we noted above. These observations provide quantitative evidence that the M_C and O phases are adaptive phases consisting of tetragonal microdomains. Application of $E//[110]$ fixes the $[110]$ orientation, where the $[100]$ and $[001]$ variants of tetragonal microdomains are of equal volume fraction: thus, the stable phase appears to be a single domain orthorhombic. Whereas for $E//[001]$, the volume fraction of the tetragonal microdomains variants are variable and not equivalent: thus, the stable phase appears to be polydomain M_C . Furthermore, these authors state that a similar approach to R phase, yields the monoclinic M_A/M_B phase, claiming M_A/M_B could also be the twin of R phase depending on the crystallographic orientation. Figure 3.29 shows the lattice parameters as increasing electric field PMN-0.15PT as $E//[001]$ and $E//[110]$. We have known that the ground state for $x < 0.30$ is M_A/M_B upon the removal of E. These two figures also show a very interesting feature for M_A/M_B : $c_m = a_r$. Besides, in the FC condition, PMN-0.15PT also shows that $c_m \approx c$, where $c \approx a_r$ (Please note: a_r is also quite close to that of the cubic phase since the R phase is only slightly distorted from the cubic phase). Similar interesting features can also be seen for $x = 0.24, 0.28, 0.30$. In addition, experimental evidence of a high domain-wall density and domain structures at various length scales at the MPB of PMN-xPT observed by piezo-force microscopy has recently been reported by Bai *et al.* [71], which is consistent with this interpretation.

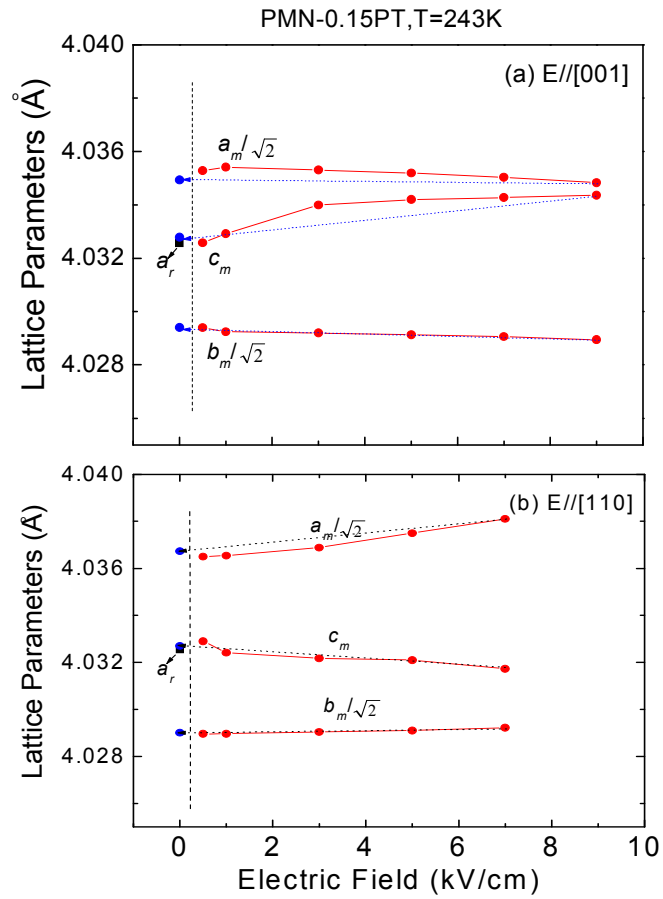


Figure 3.29 Electric-field dependence of the lattice parameters for PMN-0.15PT as $E=0.5\text{kV/cm}$ along (a) $E//[001]$ and (b) $E//[110]$. Solid represent data obtained on field-increasing, whereas dotted lines field-decreasing.

CHAPTER 4

Dynamic origin of the morphotropic phase boundary –Soft phonons and phase instability in PMN-xPT near the MPB

In Chapter 3, it was demonstrated that the phase stability is quite fragile: the phase diagrams can be altered by application of modest electric fields along different crystallographic axis. In addition, it also was found that the $C \rightarrow T$ boundary near the MPB was to shifted higher temperatures with increasing E , at a faster rate than either the $C \rightarrow M_A$ and $C \rightarrow T$ ones for higher and lower PT contents respectively. These results indicate an incipient structural instability within an apparent C phase inside the MPB – the phase field in which this incipient instability occurs has previously been designated as C' . In those two diagrams for $0.3 < x < 0.32$, an intermediate T phase is stabilized by E : inside the MPB, the transformational sequence is $C \rightarrow T \rightarrow M_C$ on cooling. However, there was been very little previous work done on the lattice dynamics of PMN-xPT crystals within the MPB: such studies would be important in understanding the C' phase and the pronounced $C \rightarrow T$ boundary shifting under E .

In this study, we report an investigation of the lattice dynamics of PMN-0.32PT (under $E=1\text{kV/cm}$) by neutron elastic and inelastic scatterings, comparing the results to that previously reported for PMN [43, 44] and PMN-0.60PT [45]. The main new result we present in this section is given in Figure 4.1, where the black thicker line in the PMN-xPT phase diagram going through large open circles with big errorbars has been added to represent the temperature at which the zone centre optic mode recovers for various PT concentrations. It can be seen that for pure PMN, the optic mode recovers at a temperature well above where a structural anomaly is measured. For heavily doped PMN (PMN-0.60PT), the two temperature scales overlap. In this work we address the zone centre optic phonon dynamics in PMN-0.32PT and show that the MPB defines a concentration where the structural transition and optic mode recovery occur at the same temperature.

Our work differs from a previous neutron investigation of zero field cooled PMN-0.32PT [72, 73] which focused on the low-energy quasielastic scattering which was associated with

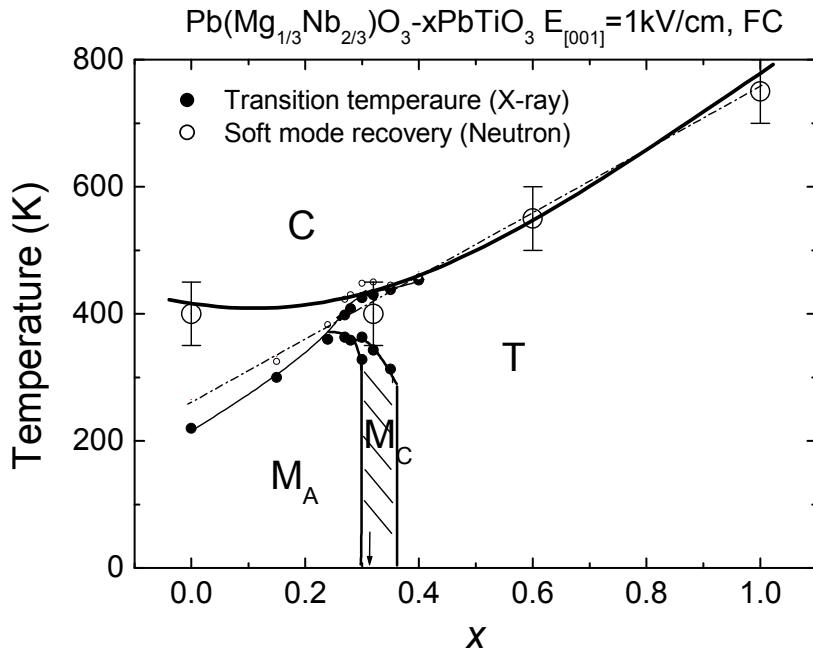


Figure 4.1 Phase diagram of PMN-xPT crystals in the field cooled (FC) condition under $E_{[001]}=1\text{kV/cm}$. The dashed and dotted line represents T_{max} of the dielectric maximum ($f=1\text{kHz}$) measured under zero field cooled (ZFC) condition. The solid line identifies T_C of the structural phase transition between cubic and ferroelectric phases. Some of this data was obtained from references [21] (Reprinted with permission from [21]. Copyright [2002], American Physical Society). The open circles represent the temperature at which a thermal abnormal expansion first observed on cooling, which was identified when the lattice constant of the (002) peak began to increase nonlinearly on cooling. The big open circles with errorbars stand for the onset temperature at which zone-center TO phonon recovery began, identified by a minimum in $(h\omega_0)^2$ with temperature. The black thicker line going through those large open circles with errorbars identifies the temperature at which underdamping of the zone-center mode became clearly evident.

dynamic polar fluctuations and did not track the optic mode dynamics through the critical temperature or give a detailed comparison of the optic mode dynamics to PMN and PMN-0.60PT. We will show that PMN-0.32PT has soft TO phonons over a broad temperature range in the C and T phase fields. Despite the fact that the structural properties change dramatically with temperature, we will show that the dynamics are nearly identical to relaxor PMN. The dynamics are also similar to that of PMN-0.60PT, but with the properties scaled by the critical temperature. These results indicate common dynamic properties across the PMN-xPT phase diagram for concentrations less than the MPB.

4.1 Neutron inelastic scattering results for PMN-0.32PT

Figure 4.2 shows a panel of selected phonon profiles obtained near (2, 2, 0.15) and (2, 2, 0.2) at 450K, 390K, and 100K. These three selected temperatures represent typical scans for the C, T and M_C phases, respectively. In the C and T phase fields, we did not observe propagating transverse optic (TO) modes at the zone center. Even scans at small but nonzero $q=0.1$ revealed no indications of a TO mode in either phase. Evidence of a TO mode only became apparent at larger values of $q=0.2$: at which point, a broad TO mode was observed. On cooling through the $C \rightarrow T$ phase transformation at T_C , a weak recovery of the optic mode was observed and it is only at low temperatures that an underdamped optic mode was found. These measurements are in accord with pure PMN and PMN-60PT as illustrated in Figure 4.3. For example, at 100K, a well-defined TO mode at $q=0.1$ was found, however at higher temperatures no well defined propagating mode was observed near the Brillouin zone center. We emphasize that a well defined TA mode was observed over the entire temperature range studied and the position in ΔE was relatively unchanged with decreasing temperature.

Combination of scans at $q=0.10, 0.15,$ and 0.20 for PMN-0.32PT demonstrated strong TO mode damping at small q near the zone-center in both the T and C phase fields, even though a structural $C \rightarrow T$ phase transformation occurred. In comparisons to prior inelastic neutron investigations of PMN [43, 44] and PMN-0.60PT [45], while it is possible that the degree of damping of the zone centre optic phonon is larger than in the PMN and PMN-60PT, the temperature dependence and energy scales of the zone centre optic mode are nearly identical to PMN and scale with the critical temperature T_c to that of PMN-60PT. These

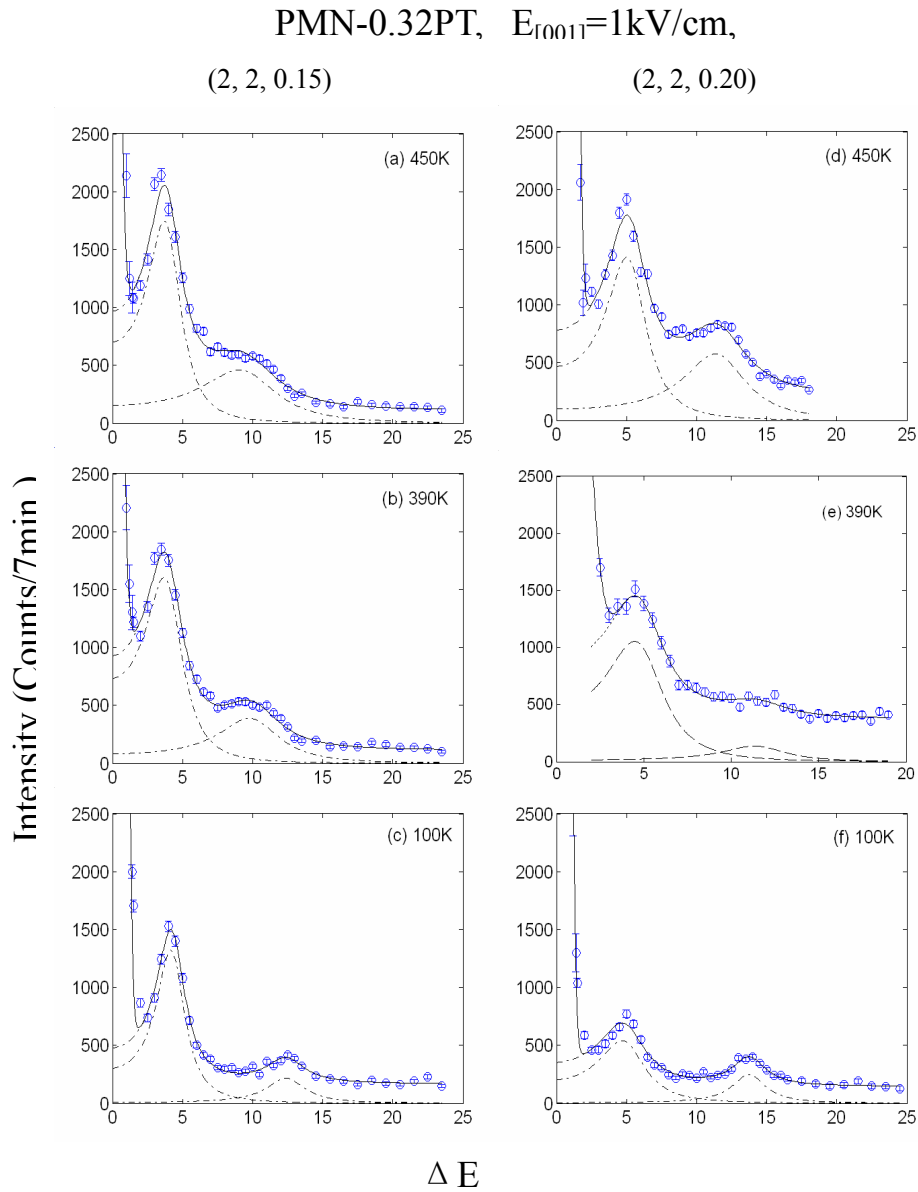


Figure 4.2 Panel of typical constant-Q scans taken at (2, 2, 0.15) and (2, 2, 0.2) for PMN-0.32PT under $E_{[001]}=1\text{kV/cm}$ at 450K, 390K and 100K. The three temperatures represent that of the cubic (C), tetragonal (T) and monoclinic M_C phases, respectively, as identified in the figure.

combined results show a common response in the lattice dynamics response throughout the PMN-xPT phase diagram, despite very different structural properties and phase transition sequences.

4.1.1 Observation and study of the soft zone center optic mode in PMN-0.32PT

To extract parameters, such as frequency and line-width, a line shape must be convolved with a resolution function and fit to the data. We have fit the data to a model with two damped harmonic oscillators as used in previous studies and described in detail elsewhere [66, 67]. Figure 4.3(b) shows the zone-center TO mode as a function of temperature for PMN-0.32PT. This data is compared to previously published results for PMN [43, 44] and PMN-0.60PT [45], which are shown in Figures 4.3(a) and (c) respectively. The open circle data points were taken from constant- Q scans at the zone-center; whereas, the solid symbol ones were obtained by extrapolating to the zero-center frequency from a nonzero q , using the formula $\omega^2 = \Omega_0^2 + \alpha q^2$ where Ω_0 is the zone-center frequency and α is a temperature independent constant. This second method is required in the “waterfall” region where the optic mode near the zone centre becomes very broad in energy and difficult to measure in a constant- Q scan. It can be seen in Figure 5-3 that the TO mode for the three PMN-xPT crystals did not completely soften to zero energy near a critical temperature. Rather, the zone-center TO mode for each of these three crystals was found to be over-damped across a broad temperature range near and above their respective T_C . The features of the phonon softening for all three crystals are very similar: the mode energy had a minimum at a particular temperature, near which a broad ‘water-fall’ effect was found due to over-damping, and which tended to recover at both lower and higher temperatures.

It is interesting to note for PMN-0.60PT that the minimum in the zone centre frequency corresponded to a C→T transition at $T_C=550\text{K}$, as determined by XRD and dielectric constant measurements: below which mode recovery began to occur. Whereas, for PMN, the minimum in the zone centre energy squared ($\hbar\omega_o^2$) did not correspond to an observable structural phase transition, either by XRD or dielectric measurements. In PMN-0.32PT, the TO mode recovery occurs near the C→T at 410 K. We note that we observed no obvious dynamic signature of the transition to the monoclinic phase at low temperatures, instead

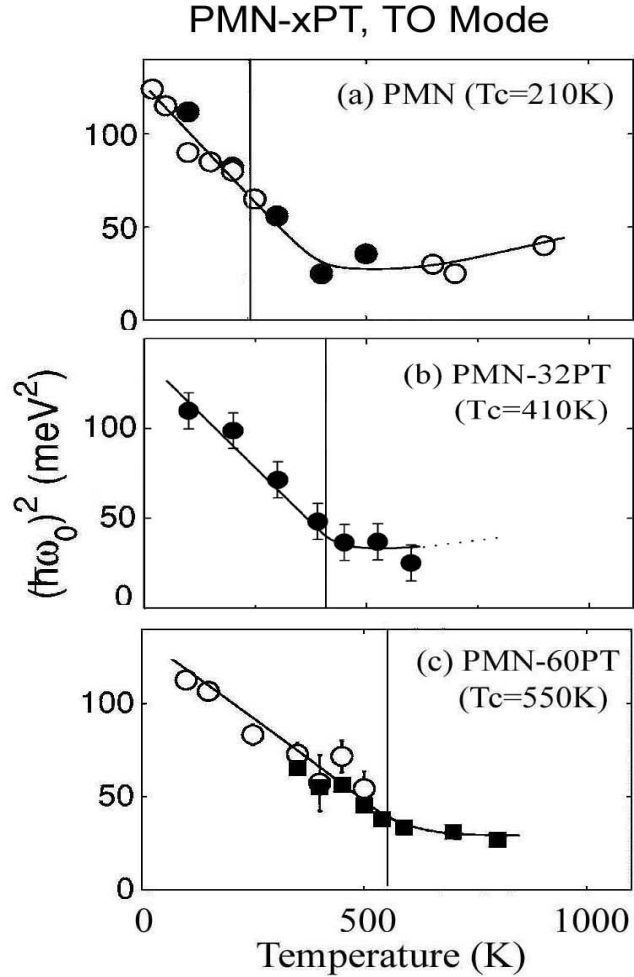


Figure 4.3 Temperature dependence of the zone-center TO phonon mode for (a) PMN (zero field); (b) PMN-0.32PT ($E_{[001]}=1\text{kV/cm}$); and (c) PMN-0.60PT (zero field): where the results for PMN and PMN-0.60PT were taken along the (200) zone, and that for PMN-0.32PT along (220). The data for PMN and PMN-0.60PT were taken from Stock *et al.* [66] (Reprinted with permission from [66]. Copyright [2005], The Physical Society of Japan). The closed symbols represent values obtained by extrapolation for nonzero q to the zone-center. The open circles were obtained from a direct constant- Q scan at the zone center.

the temperature dependence of the transverse optic mode is nearly identical to that in the relaxor PMN with short-ranged polar correlations, and in the ferroelectric PMN-0.60PT with long-ranged polar correlations. It is interesting to note that even though the dynamics (in particular the optic mode) behaves in a similar manner across the entire PMN-xPT phase diagram, the elastic diffuse scattering does not, and disappears for PT doping beyond the MPB boundary, where any relaxor properties in the dielectric response is replaced by a well defined peak characteristic of a ferroelectric phase [74].

A comparison of the temperature dependence of the zone center TO mode in PMN, PMN-0.32PT, and PMN-0.60PT reveals three interesting results. First, the overall shape is very similar with the slope of energy recovery increasing slightly with larger PT doping. Second, the temperature scale for the recovery is almost identical for PMN and PMN-0.32PT, while PMN-0.60PT goes through two well defined structural phase transitions yet no structural transition has been unambiguously identified in the bulk in PMN at zero or applied electric field using neutron or x-ray diffraction techniques [75-79]. Third, the TO mode recovery and the C->T phase transition occur at about the same temperature in both PMN-0.32PT and PMN-0.60PT with this temperature being higher in the latter. These results suggest that MPB defines a PT concentration where the structural transition matches the temperature at which the optic mode recovers. This conclusion will be discussed in more detail later.

4.1.2. Phonon dispersion and low zone-center energy

Next, we illustrate the dispersion of the TA and TO modes for PMN-0.32PT about the (220) zone at 600K ($E=0\text{kV/cm}$) and 300K ($E_{[001]}=1\text{kV/cm}$), as shown in Figure 4.4(a). At high q values (>0.2), the energy of the TO mode did not change notably with temperature. However, for $q\leq 0.2$, the TO mode began softening with decreasing q . At 600K in the C phase, a very strong softening can be seen. The dashed line represents the fact at small $q<0.15$ that the TO mode could not be resolved in the Q-scan, due to strong over-damping. Strong phonon softening and over-damping were found to persist on cooling from 600K throughout the C phase and into the T phase. At 300K, the softening of the TO mode was less pronounced and the phonon peak could be determined to lower q values: these observations

indicate a recovery of the TO phonons on entering the T phase. The TA mode was also found to soften with decreasing q , however this softening did not depend notably on temperature for that below T_{Burns} : similar TA phonon dispersion curves have previously been reported for PMN-xPT. Some changes in the TA mode parameters with temperature were revealed by analysis of the line shapes, as will be shown below.

The lack of any temperature dependence in the TA phonon energy with temperature is a key observation in light of recent models of the relaxor phase transition. The TA mode frequency is temperature independent despite a significant softening and recovery of the optic mode over a broad temperature range. This result, when compared with other results where strong TA-TO coupling is the case, indicates that there is no or very weak coupling between the TA and TO modes. This conclusion contrasts with those [72, 73], however, we note that these studies do not address the temperature dependence and the lineshape. We note that both the temperature dependence and the lineshape have been consistently described in pure PMN with a purely harmonic model with two uncoupled damped harmonic oscillators [66].

Estimation of the zone-center TO phonon energy at 600K was limited by over-damping. To overcome this limitation, the energy $(\hbar\omega_0)^2$ is given as a function of q^2 for PMN-0.32PT in Figure 4.4(b). Since the zone centre optic mode frequency can be approximated to be linear with q^2 for small q values near the zone center, we then performed an approximation by extrapolation of $(\hbar\omega_0)^2$ vs. q^2 . The results of the extrapolation are presented in Figure 4.4 which gives similar results both in absolute energy and temperature dependence to that in PMN [39, 40].

The data of Figure 4.4 clearly demonstrate (i) an anomalously phonon softening for temperatures less than T_{Burns} ; (ii) a ‘water-fall’ feature [42] at small q values presumably due to an inability of phonons to propagate in a dispersion of PNR; and (iii) an abrupt phonon recovery on cooling. The phonon energy and temperature dependence is analogous to that in PMN and PMN-0.60PT, however, the energy scale and temperature dependence of the dynamics in PMN-0.32PT are identical to those in PMN. This indicates that the dynamics

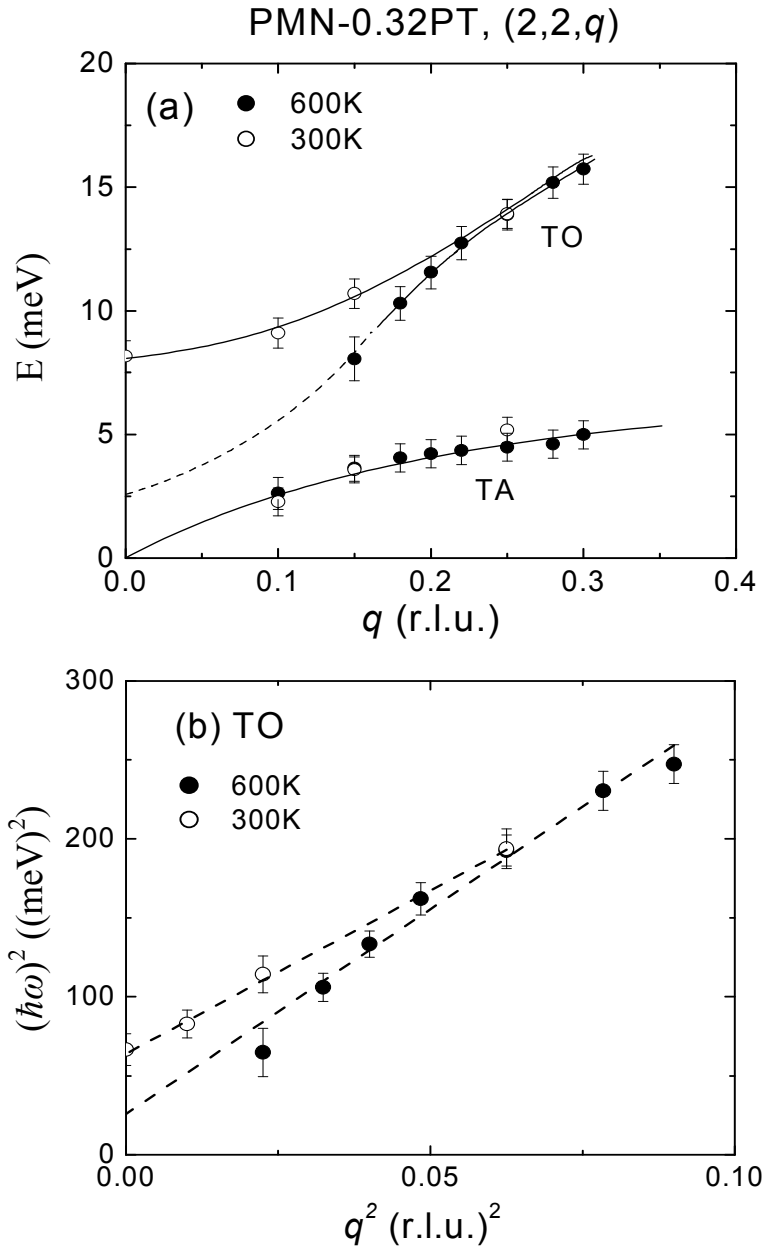


Figure 4.4 (a) Dispersion of the TA and TO modes along the (220) zone for PMN-0.32PT at 600K ($E=0\text{kV/cm}$) and 300K ($E_{[001]}=1\text{kV/cm}$). The dotted line in the 600K data represents the fact that the TO mode becomes over-damped, and hence it was hard to observe it in constant- Q scans. (b) Extrapolation of $(\hbar\omega)^2$ as a function of q^2 to the zone-center $q=0$, from which the zone-center phone energy was determined.

varies smoothly across the phase diagram despite very different structural properties and transitions. This again indicates a common dispersion and temperature dependence of the dynamics below the MPB where a structural transition and optic mode recovery coincide at the same temperature.

4.1.3 Temperature dependence of the phonon energy and line-width

Finally, we have fit the temperature dependence of the TA and TO phonon energies and line-widths away from the zone-center taken at $(2, 2, 0.15)$ for PMN-0.32PT under $E_{[001]}=1\text{kV/cm}$. In Figure 4.5(a), the energy of the TO mode can be seen to be increased on cooling below T_C , changing only slightly in the temperature range of 400-300K, and again increasing notably on cooling below 300K. These three regions of slope change are consistent in temperature with a phase sequence $C \rightarrow T \rightarrow M_C$ on cooling, as illustrated in Figure 4.1 In addition, the energy of the TA mode was found to be more temperature independent than that of the TO, except near 350K in the vicinity of the $T \rightarrow M_C$ transition, where there was a shallow minimum in E.

The temperature dependence of the line-width (Γ) of the TA and TO modes taken at $(2, 2, 0.15)$ is given in Figure 4.5(b). Strong broadening of Γ_{TO} was found at a higher temperature of 600K, which decreased (by $\sim 50\%$) in a near linear manner on cooling between 600-400K. Such broadening at high temperatures indicates a strong damping of the TO mode far into the C phase field. On cooling into the T phase field near T_C , Γ_{TO} became nearly independent of temperature. On further cooling in the M_C phase region, Γ_{TO} was found to again decrease with temperature down to 100K. Therefore, the optic mode linewidth does appear to respond to the presence of the two structural transitions despite the fact that zone centre energy extrapolates smoothly through these temperature scales. The line-width of the TA mode (Γ_{TA}) was narrower than that for the TO mode, over the entire temperature range investigated, and was relatively temperature independent. When we compare the widths of TO and TA modes to those measured from pure PMN, we find that the phonon widths in PMN-0.32PT are relatively larger, indicating a shorter lifetime and possibly more phase instability, which is hand-in-hand with the structural result discussed below.

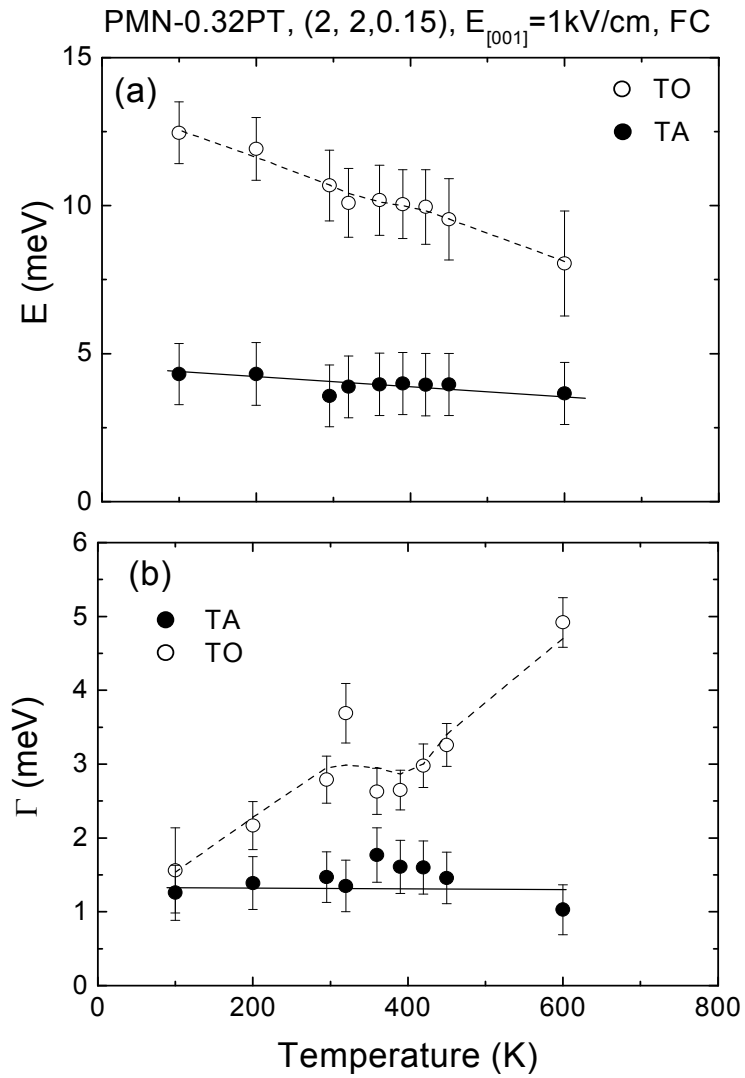


Figure 4.5 Temperature dependence of (a) the energy of the TA and TO phonon modes; the line-width Γ of the TA and TO modes; and (c) a blow-up of the line-width of the mode. These data were all taken at (2,2,0.15) for PMN-0.32PT under $E_{[001]}=1\text{kV/cm}$.

4.2 Comparative dielectric and XRD measurements

Prior dielectric and XRD measurements of PMN- x PT over a wide range of compositions have shown that T_{\max} is lower than T_C for small x , becomes closer to T_C with increasing x , and is equal to it for $x > 0.37$. These known results are summarized in Figure 5-1. Correspondingly, when $T_{\max} < T_C$ strong relaxor ferroelectric characteristics are found in the dielectric response, which become increasingly less apparent as $T_{\max} \rightarrow T_C$, and which disappear when $T_{\max} = T_C$ resulting in normal ferroelectric behavior. In the vicinity of the MPB, weak relaxor characteristics are found only in the ZFC condition, but not in the field-cooled one [80].

We also performed dielectric constant and lattice parameter studies in the field-cooled FC state for comparisons with our inelastic neutron scattering results, as shown in Figure 5-6. The temperature dependent dielectric constant ($1/\epsilon_r$) under $E_{[001]} = 1 \text{ kV/cm}$ clearly revealed two phase transitions on cooling: one near 410K and a second at 320K, as can be seen in Figure 5-6 (a). High resolution XRD studies confirmed this transformational sequence to be $C \rightarrow T \rightarrow M_C$ as shown in Figure 5-6 (b), in agreement with the diagram given in Figure 4.1. The dielectric constant peak was sharp with no noticeable frequency dispersion about T_{\max} , neither under $E_{[001]} = 1 \text{ kV/cm}$ as reported here nor in the zero-field-cooled condition as previously shown. In this regard, PMN-0.32PT exhibits phase transformational characteristics similar to those of a normal ferroelectric, rather than those of a relaxor. However, linear Curie-Weiss behavior of $1/\epsilon_r$ was not observed above the maximum in the dielectric constant, indicating the presence of a local polarization to temperatures much higher than that of T_{\max} : presumably up to T_{Burns} (620K).

We then measured the field dependence of the (002) d-spacing, in the vicinity of the $C \rightarrow T$ boundary for PMN-0.32PT. We found no significant difference in $d_{(002)}$ between $E = 0$ and $E_{[001]} = 0.5 \text{ kV/cm}$, except that the $C \rightarrow T$ boundary was increased by about 5K. However, at higher applied fields of $E_{[001]} > 2.5 \text{ kV/cm}$, we found that this boundary was dramatically shifted to higher temperatures by about 75K. Since $d_{(002)}$ was increased by application of $E_{[001]}$ above 425K, we can presume that the crystal does not remain cubic in the temperature range of 425-500K, rather the data evidence a lower symmetry structure. The shift of the

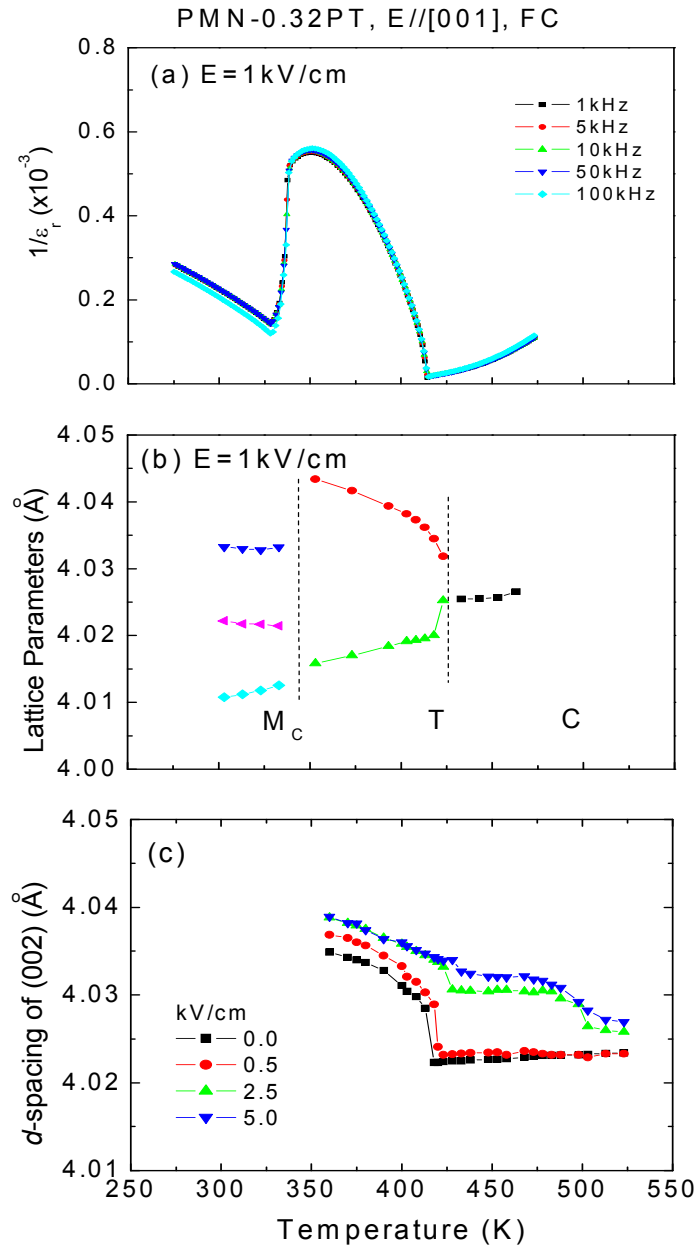


Figure 4.6 Temperature dependence of (a) the inverse dielectric constant ($1/\epsilon_r$) at different frequencies under $E_{[001]}=1\text{kV/cm}$; (b) the lattice parameters under $E_{[001]}=1\text{kV/cm}$; and (c) the d-spacing of the (002) under different electric fields for PMN-0.32PT with $E//[001]$.

C→T boundary by $E_{[001]}$ determined by XRD was not accompanied by a corresponding shift in the temperature of the dielectric maximum. Step-like changes in $d_{(002)}$ were observed near both 425K and 500K. For $E_{[001]}=5\text{kV/cm}$ (data not shown), it was not possible to determine a distinct C→T phase boundary, rather $d_{(002)}$ changed smoothly and continuously on cooling.

Please note that the temperature region in which the C→T boundary can be dramatically shifted by E corresponds to that in which overdamped phonons were observed above by inelastic neutron scattering. Also, both higher and lower PT contents did not exhibit such a dramatic shift in the C→T boundary (as summarized in Figure 4.1), nor did they exhibit such anomalously strong phonon over-damping in the C and T phase fields (as summarized in Figure 4.2).

4.3 Discussion and Summary

In the phase diagram of Figure 4.1, we have summarized our findings – by the addition of two more sets of points. The first are open circles with error bars that represent the temperature of the onset of TO phonon recover, which was defined by the temperatures of minimum in zone center TO phonon energy. We can see that for low PT concentrations, the phonon recovery occurs at higher temperatures than a detectable structural transition with x-rays. This clearly shows that the structural properties of the relaxors are defined by two temperature scales which merge at the morphotropic phase boundary and become a single temperature scale for large PT concentrations where a long-ranged ferroelectric phase is formed. The two temperature scales has been explained in terms of a random field model in direct analogy to model magnets [81]. Our results on PMN-0.32PT show that the merging of the two temperature scales occurs gradually with PT concentration.

The current results presented for PMN-0.32PT show that the zone centre optic mode recovers at the same temperature as a structural transition occurs. The zone centre dynamics are also identical to that of pure PMN but are scaled to lower temperatures to that of PMN-0.60PT. Therefore, the MPB defines a PT concentration where the optic mode recovery occurs at the same temperature as the zone centre optic mode recovery, and our results point to a dynamical definition of the MPB. This result is mimicked in temperature

of the diffuse scattering studied in Ref. [74] which reports that the diffuse scattering is onset at the same temperature for concentrations below the MPB. The diffuse scattering in those measurements showed the presence of two temperature scales which merged into a single one for PT concentrations near the MPB boundary. For concentrations above the MPB boundary, the temperature dependence of the diffuse component was interpreted in terms of critical scattering expected near a well-defined phase transition. The softening of the optic mode there looks to be associated with the formation of polar nanoregions below the MPB and a long-ranged ferroelectric phase for concentrations above. The combined results from the phonons and the diffuse scattering show that both are important and related to the presence of the high piezoelectric constants in these materials.

It is interesting to note that the minimum zone centre energy in PMN-0.32PT occurs near the C-T phase transition and there is no strong effect on the subsequent monoclinic transition on the zone centre dynamics. This result combined with PMN and PMN-0.60PT, show a common dynamic response across the PMN-xPT phase diagram. What is interesting is the dynamics of PMN, PMN-0.32PT, and PMN-0.60PT is quite different to the measured dynamics of pure PT [10]. Pure PT does not show the degree of dampening observed in PMN, PMN-0.32PT, and PMN-0.60PT and also softens to a much lower energy and recovers at the first order cubic to tetragonal transition. Phonon damping below T_{Bums} has previously been interpreted in terms of a condensation of PNR, which impede the propagation of long-wavelength polar modes [41, 42, 44]. Our results for PMN-0.32PT, combined with those from PMN and PMN-0.60PT, show that the strong damping persists in both relaxor and classical ferroelectric phases, and are not a distinct feature of the relaxor system. This seems to directly correlate the overdamped zone centre phonon mode with the disorder introduced through the extensive mixture between Mg^{2+} , Nb^{5+} , and Ti^{4+} cations in these compounds.

The ‘phase boundary’ along which the anomalously high temperature for (x=0.32PT) occurred had a corresponding abnormality in the C→T boundary (identified by XRD). The C→T boundary shifted to higher temperatures with increasing $E_{[001]}$ at a dramatically faster rate than either the C→ M_A or C→T ones for higher and lower PT contents respectively. Only in the compositional space inside the MPB, where the transformational sequence of

$C \rightarrow T \rightarrow M_C$ occurs on cooling, was the cubic \rightarrow ferroelectric transition notably shifted up in temperature with increasing $E_{[001]}$. These results indicate the presence of an incipient structural instability within an apparent C phase inside the MPB. Another indication of this comes from the abnormally broad TO mode (larger than that from PMN or PMN-0.60PT), which is also suggestive of phase instability, consistent with those measured from PMN-0.60PT.

In summary, our investigations clearly show the presence of soft phonons for PMN-0.32PT over a wide temperature range from T_{Burns} to the $T \rightarrow M_C$ phase boundary, within the compositional range of the MPB. The zone-center optic phonon behaves nearly identically to that of pure PMN and PMN-60PT. In addition, we observed that these soft phonons have a recovery which coincides with the transition into the T phase on cooling. We have also found that the phase boundary between C and T can be easily shifted by the application of an external electric field along [001], indicating a phase instability which is consistent with the extra broad TO mode in this compound. Our findings establish that MPB ferroelectrics have unique dynamical properties.

CHAPTER 5

Phase transformations and structural heterogeneity in Fe-Ga alloys

The properties of Galfenol can not be explained by assuming that the alloy is a structurally homogeneous body centered cubic phase and that its magnetostriction is an intrinsic property of this phase. The following observations indicate that Galfenol is inhomogeneous on a nano-scale:

1. The giant magnetostriction of bcc Fe-Ga depends on the thermal history of the alloys (see Figure 1.11). This fact can not be explained by the conventional theory of magnetostriction of homogeneous single phase materials.
2. Magnetic-force images reveal a miniaturization of conventional large-scale domain structures of 12at.%Ga with increasing Ga concentration towards the solubility boundaries, evolving into a featureless ensemble of ultra fine nano-domains [82]. This is the domain structure change predicted (and observed) by the frustration of the magnetization by randomly distributed nano-clusters.
3. Abnormally high reduction of the elastic modulus, E , in Fe-17at.%Ga ($\Delta E/E \approx 50\%$) and a very large frequency-dependent internal friction [83] indicate the presence of coherent nano-clusters.
4. Numerous prior X-ray and TEM observations of the related Fe-Al, Ni-Cr, Cu-Al, Cu-Zn, and Ni-Mo alloys exist that also indicate the presence of nano-clusters in the form of coarsening-resistant clusters in their bcc phase fields.

These observations indirectly support the idea that Galfenol is a nano-composite, spontaneously formed within the single-phase metastable field of the phase diagram that is conceptually shown in Fig. 1.10 (right).

In this section of my dissertation, I have carefully performed structural studies of Fe-Ga alloys by XRD and neutron diffraction. I will show that slow-cooling or annealing favor the development of a long-range ordered (LRO) DO_3 phase, whereas the as-grown or furnace-cooled state favor the formation of short-range ordered (SRO) DO_3 nano-precipitates.

Then, I will show, here, by diffuse scattering that indeed the $\{100\}$ superlattice reflections are split and off-center, indicating a tetragonal distortion or a lower symmetry that has $c/a \sim 1.2$.

5.1 Structural studies of decomposition

Recently, a metastable phase diagram of Fe-Ga alloys [54] has been reported, which was revised from an earlier equilibrium one by Okamoto [55]. At 300°C, a disordered bcc α -Fe (or A_2) structure extends to 15, whereas a long-range ordered DO_3 structure is dominant for $x > 23$ [5]. For $15 < x < 23$, a two-phase (A_2 and DO_3) region exists. In this composition range, quenching is known to preserve the high-temperature A_2 structure and slow cooling leads to the development of a long-range ordered (LRO) DO_3 structure. Recently, high resolution x-ray diffraction (XRD) studies have shown that Fe-19at%Ga is entirely A_2 when quenched from 700°C, but is a two-phase mixture of A_2 and DO_3 when slow-cooled (10°C/min.). However, the structural decomposition ($A_2 \rightarrow A_2 + DO_3$) in Fe-xat.%Ga alloys for $13 < x < 25$ has yet to be investigated. Here, we have performed high resolution x-ray and neutron diffraction measurements on Fe-xat%Ga for $14 < x < 25$. Our experiments show that (i) Fe-14at%Ga and Fe-20at%Ga have a disordered A_2 structure after quenching, but that in both cases a DO_3 phase precipitates out of the A_2 matrix on slow cooling (2°C/min.); (ii) phase separation occurs below 550°C on cooling (for $x=20$) where a notable radial line broadening develops; and (iii) the (200) and (002) Bragg peaks exhibit multiple peaks along the transverse directions, indicating the presence of several grains with a and c -axes that are slightly tilted with respect to each other.

X-ray diffraction

We investigated the phase stability of (100)/(010)/(001) oriented Fe-xat.%Ga alloys ($x=14, 20, 25$) at room temperature by x-ray diffraction around the (100), (110), (200) and (220) reflections: following quenching, furnace-cooling and slow-cooling. Figure 5.1 shows $\theta/2\theta$ scans taken around the (100), (200), and (110) reflections for furnace-cooled Fe-xat.%Ga alloys ($x=14, 20, 25$). The quenching treatment was successful in suppressing LRO DO_3 as evidenced by the absence of (100) or (111) superlattice reflection, which are not

allowed for the A₂ structure. However, under the furnace-cooling treatment, the (100) superlattice reflection were not found for x=14 and 20, as shown in Figs. 5.1(a) and 5.1(b); whereas, for x=25, a weak (100) reflection can be seen in Fig. 5.4(c). Considering that the (100) reflection is allowed for the DO₃ structure but not for the A₂, the furnace-cooled Fe-25at.%Ga data demonstrate the existence of a LRO DO₃ phase. Whereas, splitting of the (200) and (110) reflections was not observed for x=14 and 20 after furnace-cooling, consistent with the features of the A₂ structure. According to the phase diagram in Fig. 1.10, Fe-20at.%Ga is located in a two-phase region. Assuming this phase diagram is correct, we can reconcile the absence of (100) and/or (111) superlattice reflections by assuming the average size of any DO₃ clusters is quite small; if the size of DO₃ clusters is much smaller than the coherence length of the x-rays, then the diffraction pattern will only reveal features related to the A₂ structure. In fact, nanometer-scale clusters of DO₃ embedded into an A₂ matrix (~100nm) have previously been reported by electron microscopy for Fe-20at.%Ga [55]. As the Ga content was increased, these nano-clusters coarsened, reaching sizes of ~1μm for Fe-22.5at.%Ga, which are consistent with our observation of (100) superlattice reflections for the Fe-25at.% Ga sample after furnace cooling.

In order to investigate structural decomposition in Fe-xat.%Ga (x=14, 20, 25) in the slowly cooled state (2°C/min.), x-ray $\theta/2\theta$ scans were performed around the (110), (200) and (220) reflections. Figure 5.2 presents $\theta/2\theta$ scans taken about the high index (220), in order to clearly illustrate the peak splitting. These data points were fitted using Gaussian functions. These line scans clearly demonstrate that slow-cooling produces a mixture of A₂ and DO₃ phases that separate out from the high-temperature A₂ solution. For Fe-14at.%Ga, a broad shoulder is present on the low angle side of the main peak with lattice parameters, $a_1=2.880\text{\AA}$ and $a_2=2.877\text{\AA}$; Fe-20at.%Ga exhibits two distinct peaks with $a_1=2.894\text{\AA}$ and $a_2=2.880\text{\AA}$; and Fe-25at.%Ga shows only a single peak with $a_1=2.903\text{\AA}$. The Fe-25at.% Ga sample exhibits a LRO DO₃ structure on slow cooling, as evidenced by a weak (100) superlattice reflection with an intensity ratio of $I_{(200)}/I_{(100)}\approx 100/1$. However, no such (100) reflection was observed for Fe-20at.%Ga, even though two distinctly different peaks are observed about the (220) or (110) reflections. There may be two principal reasons for the absence of a (100)

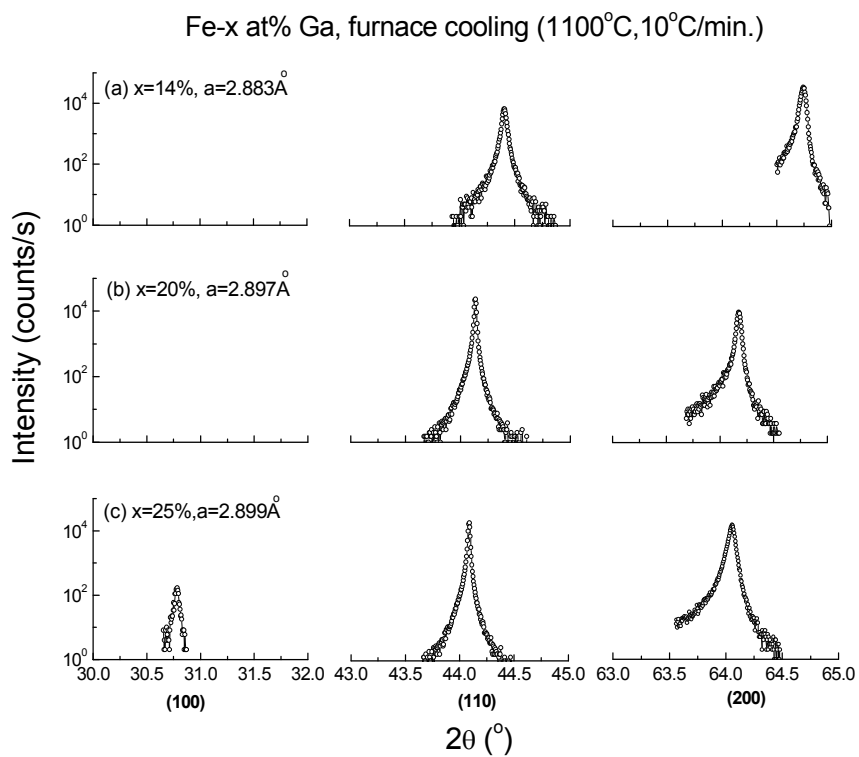


Figure 5.1 (100), (110) and (200) line scans of Fe-x at% Ga ($x=14, 20, 25$) measured with x-rays at room temperature after furnace cooling.

reflection for Fe-20at.%Ga: (i) the weak structure factor because Fe ($Z=26$) has an atomic number very close to that of Ga ($Z=31$); and (ii) a limited x-ray penetrating depth of 5 to 10 μm . The absence of this reflection in XRD scans makes it difficult to identify which peaks correspond to DO_3 and which to A_2 for Fe-14at.%Ga and Fe-20at.%Ga. However, neutron results for slowly cooled Fe-19at.%Ga exhibited a pronounced single Gaussian peak around the (100) with a lattice parameter $a=2.907\text{\AA}$, whereas in the as-grown condition, a flat and diffuse intensity distribution was found, as can be seen in shown in Figure 5.3. Comparisons of neutron results reveal that the Fe-19at.%Ga has a LRO DO_3 phase within the A_2 matrix in the slowly cooled state, but has fine-scale DO_3 precipitates in the as-grown state. Thus, we can identify the secondary low angle of (220) reflection in the XRD linear scans of Fig. 5.2 to be peaks of the DO_3 phase. Furthermore, this comparison reveals that lattice parameters for DO_3 in Fig. 5.2 consistently shifts to lower angles with increasing Ga, whereas the lattice parameter of the A_2 phase does not notable change. From the data after Gaussian fitting in Fig. 5.2, we estimate that the Fe-14at.%Ga sample has a $\langle 25/75 \rangle$ (DO_3/A_2) volume fraction ratio at room temperature. We cautiously note that this is an approximation: some difficulty lies with the presence of adjacent crystallites having slightly different orientations with respect to each other tilted along the omega direction, as will be shown below. Precise determination of the phase volume fractions would require intensity integration over all such transverse peaks. However, in the case of x-rays, these results would also be somewhat unreliable, due to the limited sample volume from which diffraction occurs. Also, please note that we found line scans taken at slightly different omega settings to have similar volume fractions. The phase diagram suggests that the disordered bcc structure (A_2) ends around $x=15$ above 300°C . By extrapolation of the phase diagram, the two-phase region should extend to lower Ga content at room temperature, which is consistent with our findings of a modest volume fraction of the DO_3 phase at room temperature for $x=14$. Near the $\text{A}_2/\text{A}_2\text{-DO}_3$ phase boundary, the development of fully ordered DO_3 precipitates requires decomposition into Ga rich and poor regions. This boundary moves to lower temperatures with decreasing x because the decomposition becomes diffusion-limited, as shown in the phase diagram of Fig. 1.10. Thus, only short-range correlated DO_3 -like regions can form within the A_2 matrix. Constraint of the DO_3 phase for $x=14$ is evidenced by the small

Fe-x at% Ga, (220), annealing (1100°C, 2°C/min.)

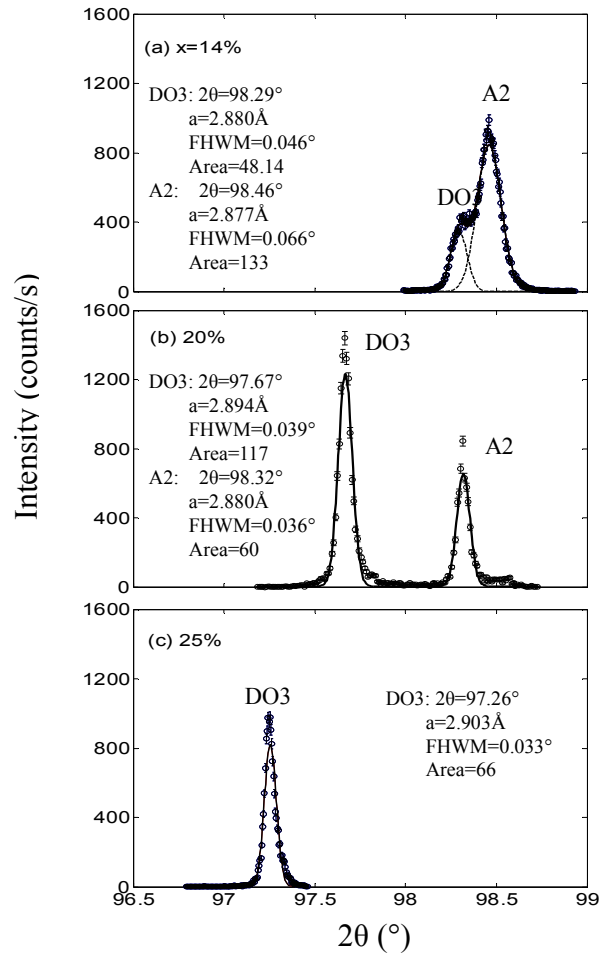


Figure 5.2 (220) line scans of Fe-x at% Ga (x=14, 20, 25) measured with x-rays at room temperature after very slow cooling. The curves are fitted to a Gaussian function.

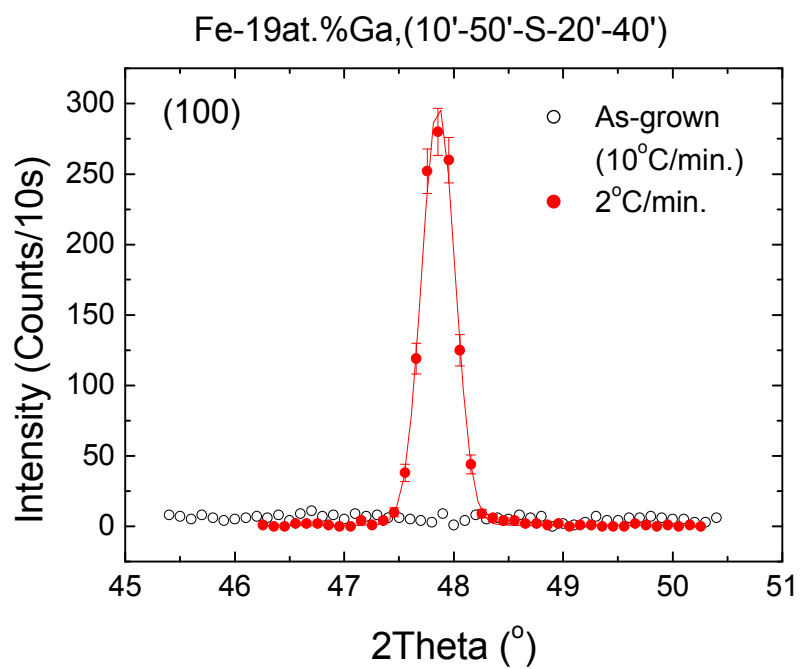


Figure 5.3 Neutron (100) profiles for (100)/(010)/(001) oriented Fe-19at.%Ga (5x5x5mm) in as-grown and slowly cooled states, respectively.

2 θ splitting (even at such high angles) in Fig. 5.2(a) between the DO₃ (shoulder) and A2 peaks, and by the relatively large linewidth (FWHM_{DO₃}=0.046°, FWHM_{A₂}=0.066°) for the individual peaks. Figure 5.2 (b) shows (220) line scans for x=20 in the slow-cooled state. These data indicate that the DO₃ volume fraction is ~70%, becoming a matrix containing A2 precipitates. Furthermore, this figure shows that the peak splitting between the DO₃ and A2 peaks is quite large; neither phase constrains the other. In this case, a coarsening of DO₃ precipitates can occur from the high-temperature A2 solution on cooling. In addition, the linewidth was noticeably more narrow (FWHM_{DO₃}=0.039°, FWHM_{A₂}=0.036°) than those for x=14. Finally, Figure 5.2 (c) shows that the (220) scan for x=25 exhibits a single DO₃ peak, consistent with the phase diagram of Fig. 1.10 that shows a DO₃ single phase field for x>23 (albeit the weak shoulder on the high angle side of the peak suggests the presence of a very small amount of A₂ precipitates constrained within the DO₃ matrix).

Neutron diffraction

To investigate the decomposition of the DO₃ phase out of the A2 matrix, we next performed neutron scattering measurements on the (110)/(1 $\bar{1}$ 0)/(001) oriented Fe-20at.%Ga after furnace-cooling from 800°C. Figure 5.4(a) shows (200) line profiles as a function of temperature for Fe-20 at% Ga. It can clearly be seen that the (200) peaks shifted towards the right side on cooling. The extracted lattice parameters (after fitting to a Gaussian function) decreased linearly with decreasing temperature, as shown in Fig. 5.4 (b). The thermal expansion was clearly linear on cooling from 800°C to room temperature. However, following the phase diagram (see Fig. 1.10) and our neutron results for as-grown and slowly cooled alloys (see Figure 5.3), Fe-19at.%Ga has the A2 structure at high temperature and decomposes into a two-phase region around 680°C with decreasing temperature. The linewidth of the (200) reflection on cooling in Figure 5.4 (c) is consistent with the phase diagram. The linewidth exhibits a sharp decrease between 800-700°C on cooling; and then broadens with decreasing temperature between 650-450°C, coinciding with the entry into the A2+DO₃ two phase field. The broadening of the linewidth in the vicinity of the two-phase field can be attributed to the formation of fine-scale DO₃ precipitates in the A2 matrix. However, the linewidth was independent of temperature on further cooling below 450°C.

Fe-20 at% Ga, (200), furnace cooling

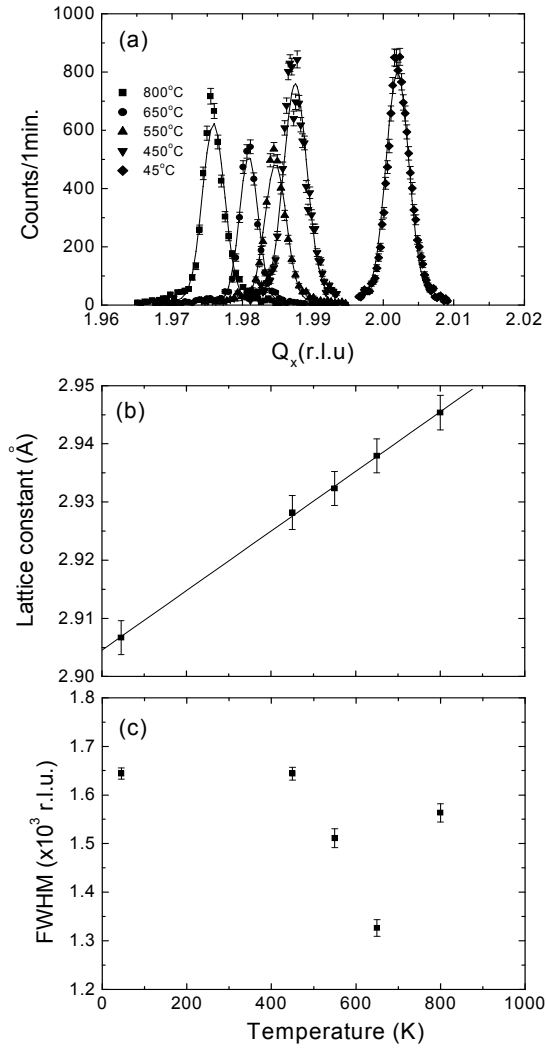


Figure 5.4 (a) (200) line profiles, (b) lattice parameters, and (c) linewidth (FWHM) of Fe-20 at% Ga alloy as a function of temperature on furnace cooling beginning from 800°C. These data were fit to a Gaussian function.

Since there exist short-range-ordered DO_3 clusters in the furnace cooled condition as discussed above, the single peaks in Figure 5.4 (a) only reveal features of the A_2 structure. The features for decomposition of DO_3 nano-clusters are only apparent in the broadness of the (200) linewidth. Furnace-cooling may not allow for sufficient annealing; thus the clusters of DO_3 that precipitate out of the A_2 matrix may remain small. We measured multiple scans ("mesh" scans) around the (200) and (002) reflections in the (H0L) zone to obtain intensity maps for furnace cooled ($10^\circ\text{C}/\text{min.}$) Fe-xat.%Ga square rings ($x=12, 20, 25$) at room temperature, as shown in Figure 5.5. The mesh scans for $x=12$ show at least four peaks along the transverse direction, which indicate the presence of multiple crystal grains. Similar results were obtained for $x=20$ and 25. A comparison of the mesh scans reveals that the (200) Bragg peak for $x=20$ is broader along both the radial and transverse directions than that for $x=12$ and 25. The nature of these satellite peaks are not fully understood at this time.

We also investigated the textures and grain structures on Fe-xGa alloys. Figure 5.6 (a) shows room temperature optical image of [110]-oriented Fe-20at.% Ga (in the very slow-cooled condition), which has a grain structure with an average grain size of 0.1~1mm. Similar grain structures also were observed on either very slow cooled or quenched (into icy water) Fe-xGa alloys for $x=12, 20$ and 25. Similarly, SEM images also revealed grain structures in Fe-23at.%Ga, as shown in Fig. 5.6 (b), which are outlined with dotted lines. The composition across the grain boundaries, determined by energy dispersive analysis by x-rays, revealed that the average Fe/Ga ratio was essentially constant, through of the various grains.

Please note that we performed mesh scans over a wider angle range than presented above, but did not find any additional splitting at larger angles; nor were splitting along ϕ or ψ tilt directions observed. These results show that adjacent crystallites are only slightly tilted with respect to each other. We also note that mesh scans taken in the very slow-cooled condition had only a single broad contour extending over the entire transverse scan (data not shown), rather than distinct satellite peaks: suggesting a possible release of elastic strain due to lattice parameter mismatch during decomposition.

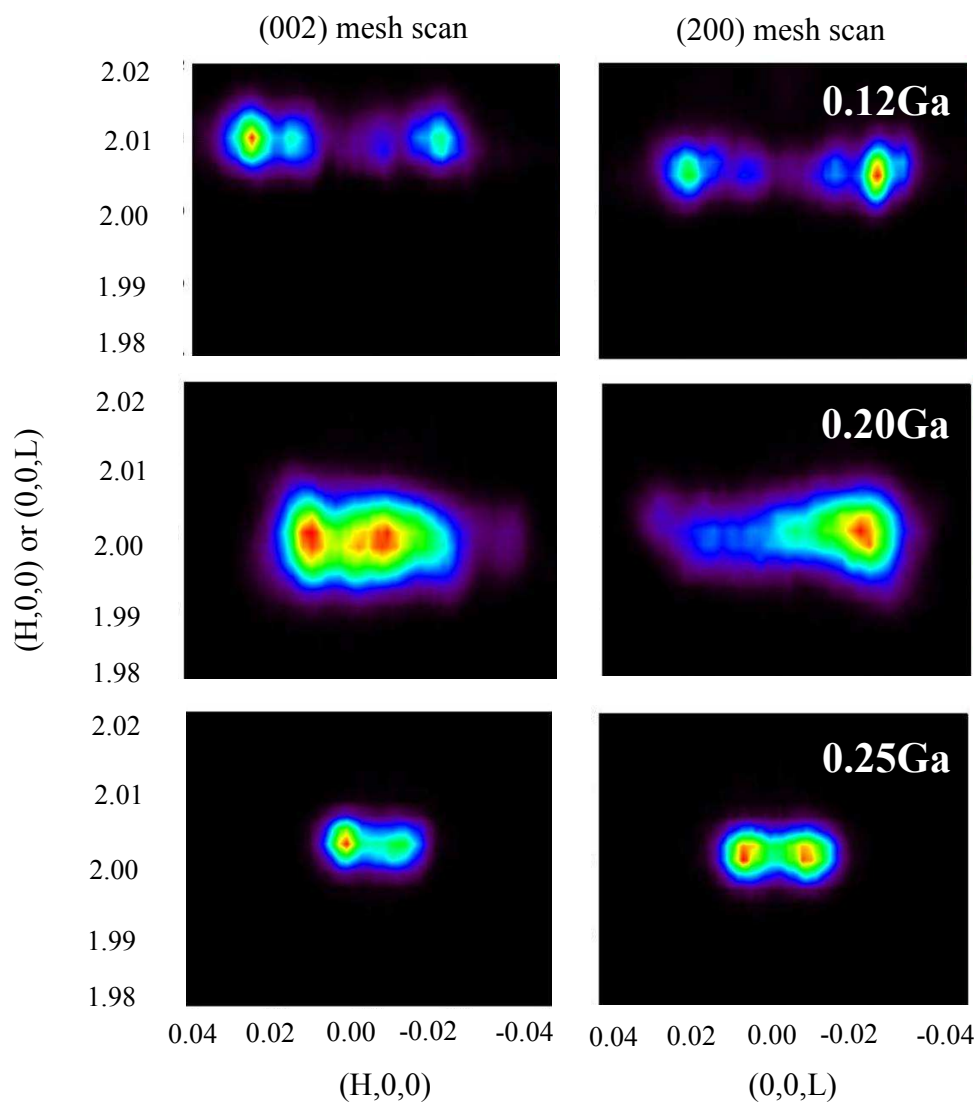


Figure 5.5 (200) and (002) Mesh scans of Fe-x at% Ga alloys measured with neutrons in the (H0L) zone at room temperature.

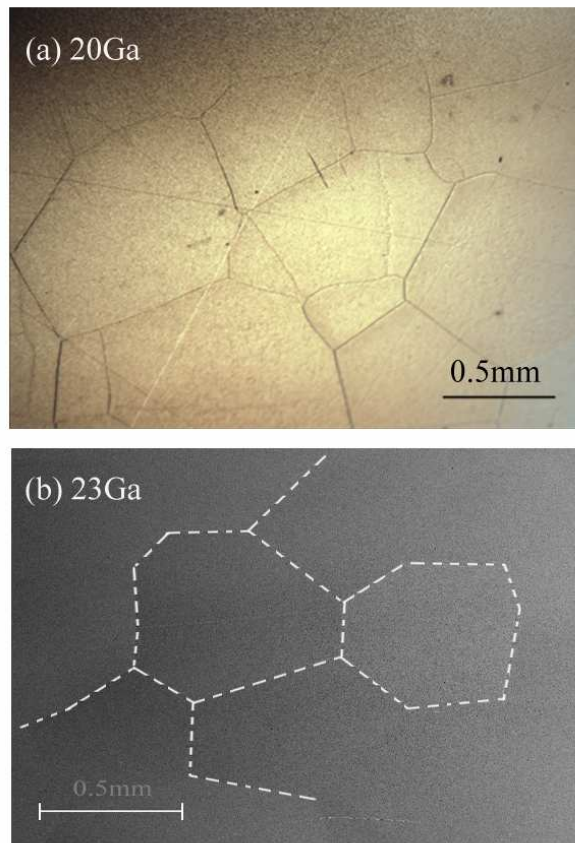


Figure 5.6 Textures and grain structures of Fe-xGa alloys, (a) optical image of [110] oriented 20 at% Ga, and (b) SEM image of [001] oriented 23at%Ga, annealed at 1100°C (2 hours) and cooled as a rate of 2°C/min.

5.2 Observation of tetragonal-like splittings in Fe-19at.%Ga by neutron diffuse scattering

Recently, Khachaturyan and Viehland [61] have proposed a structural heterogeneous model in Fe-Ga, based on decomposition and confined displacive transformations. This model first predicts that a DO₃ nanodispersion forms within an A2 matrix. This process was believed to occur within the A2 single-phase field of the coherent phase diagram, previously designated as K-state for the compositionally similar Fe-Al system.. This nanodispersion has recently been reported by high resolution transmission electron microscopy (HRTEM) studies, here at Virginia Tech of which I participated as a collaborative investigator. Computer simulations of the lattice image confirmed that the nanodispersion was indeed of a DO₃-like phase, whereas the matrix was A2. This HRTEM investigation also revealed that the DO₃-like nanoregions were full of fine dislocations, as predicted by the Khachaturyan-Viehland theory, which are required for stress accommodation.

However, to date, a second equally important prediction of the Khachaturyan-Viehland theory [61] for decomposition and confined displacive transformations in Fe-Ga alloys has not yet been confirmed. This is the prediction that the DO₃ nano-precipitates undergo a local martensitic transformation in the DO₂₂ structure. This transformation requires a large *c/a* splitting of ≈10%. That is confirmed within the DO₃ nanoprecipitates: i.e., that in fact the nanoprecipitates contain near atomically thin tetragonal twins, which require dislocation loops to elastically relax the stress. However, evidence of local tetragonal displacement within the DO₃ phase has not yet been reported. Broad {001} type superlattice reflections are well known to accompany the formation of short-range ordered DO₃ regions or clusters, but to date there has been no structural evidence of a tetragonal splittings.

Figure 5.7 shows diffuse scattering contours near the (100) zone that were taken at room temperature for (a) as-grown Fe-19at.%Ga, (b) slow-cooled Fe-19at.%Ga, and (c) as-grown Fe-25at.%Ga. The as-grown Fe-19at.%Ga exhibited a weak diffuse intensity that was very broad in Q_x, consistent with the presence of short-range ordered (SRO) nanoprecipitates. In the slow-cooled condition of Fe-19at.%Ga, a significantly different (100) scattering profile was found: a strong and well-developed intensity contour can be seen in Fig. 5.7(b). Similar

Fe-xat.%Ga, (100), 300K, $E_i=14.7\text{meV}$
BT-7, Open-50°-40°-180°

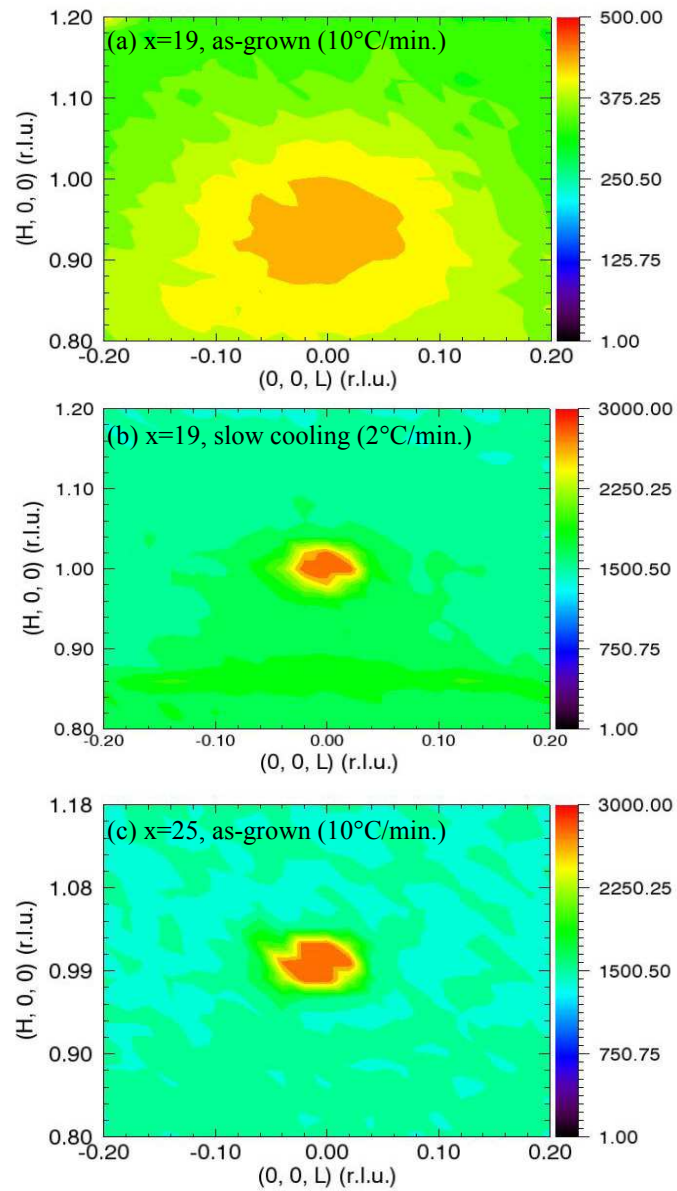


Figure 5.7 Diffuse scattering contours near the (100) zone that were taken at room temperature for (a) as-grown Fe-19at.%Ga, (b) slow-cooled Fe-19at.%Ga, and (c) as-grown Fe-25at.%Ga.

sharp intensity contours were found for as-grown Fe-25at%Ga, as that for $x=19$ in the slow-cooled condition. These findings are consistent with recent structural studies by x-ray diffraction (XRD) (please refer to the next section): in that a long-range ordered (LRO) DO_3 phase was found to coexist with an A2 phase in the slow-cooled condition for $19 \leq x \leq 22$, but not in the furnace-cooled one. The presence of $(1/2, 1/2, 1/2)$ superlattice reflections, confirmed by XRD (data not shown), eliminates the possibility of B2 ordering as the origin of the (100) superlattice reflection; also we can eliminate the A2 phase, as it does not have a (100) superlattice reflection. Thus, we can conclude that (i) the DO_3 phase is the structural origin of the (100) superlattice reflection; (ii) a LRO DO_3 phase decomposes out of the A2 matrix on slow-cooling of $x=19$ and 25; whereas instead (iii) SRO DO_3 nanoprecipitates decompose out in the as-grown and/or furnace cooled conditions of $x=19$.

It is important to note several other features for Fe-19at%Ga in the as-grown condition, given in Fig. 5.7(a). First, the intensity profile of the diffuse scattering had an isotropic or circular contour in reciprocal space. This type of diffraction pattern indicates that the shape of the DO_3 nanoprecipitates tends to be spherical in real space. This is consistent with reports of the DO_3 nanoprecipitates morphology by electron microscopy [54]. Second, the peak in the diffuse scattering was off-centered to lower values of Q_x , relative to that expected by the position of the principle (200) reflection from which a^* was determined. This off-centering indicates a distortion to a structure with symmetry lower than cubic on the local scale. Considering the (100) superlattice diffraction is a characteristic of only the DO_3 structure within the possible phases (A2, DO_3 and L1_2), and that we have excluded B_2 , we designate this SRO structure as DO_3 -like nanoprecipitates.

Next, we investigated the effect of Ga content on the decomposition of nanoprecipitates from the A2 matrix. Diffuse scattering was performed along the radial direction of the (100) zone for $x=10, 15$, and 19 in the as-grown condition, as shown in Figure 5.8. The sharp peaks centered at $Q_x=1.0$ for $x=10$ and 15 were due to half wavelength neutron contamination, as indicated in the figure: this was confirmed because these peaks entirely disappeared after placing the third HOPG filter in front of the sample, as shown for $x=10$ in the inset of the figure. The very low intensity spikes near $Q_x=0.65$, circled in the figure, are probably related

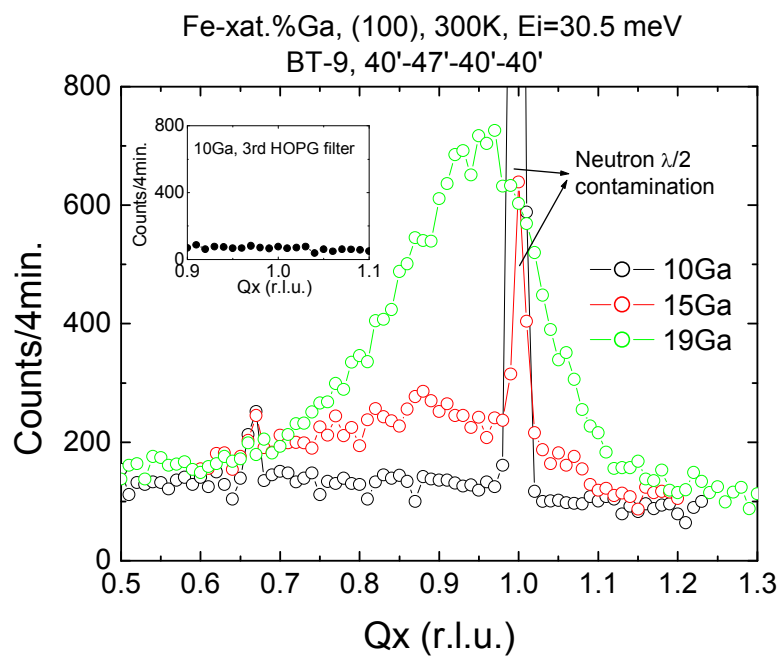


Figure 5.8 Diffuse scattering profiles around (100) along the radial [100] for the as-grown Fe-xat.%Ga (x=10, 15, 19). The inset shows that the diffuse scattering intensity is zero in x=10 after putting the third HOPG filter before the sample.

to either statistics or another unknown contamination. For $x=10$, no diffuse scattering was observed; rather, the diffuse scattering profile was flat over the range of $0.5 < Q_x < 1.3$. By comparing the intensity at $Q_x=0.5$ and 1.2 , it can be seen that this flat response is from the background, as it was equal for all compositions studied ($x=10, 15, 19$) independent of any other features in the intensity profile. For $x=15$, a weak and broad off-centered bump can be seen in the figure, indicating formation of SRO DO_3 -like nanoprecipitates. With further increasing Ga content to $x=19$, the intensity of this broad peak notably increased, but remained very broad and off-centered: consistent with the intensity contours of Fig. 5.7(a). The radial scans for $x=22$ (not shown) were very sharp Bragg peaks centered exactly on the (100), as can also be seen to be similar to the contour scan of $x=25$ in Fig. 5.7(c).

These results show that the volume fraction of DO_3 -like nanoprecipitates decomposing out of the A2 matrix increases with increasing Ga-content. This is consistent with the phase diagram of Fe-Ga [55]: where $x=10$ is in the A2 single phase field far away from the two-phase region, $x=15$ and $x=19$ are located in the two-phase A2- DO_3 field, and $x=22$ is in the LRO DO_3 single phase field but close to the boundary with the two phase region. The decrease in peak width for $x=19$, relative to $x=15$, indicates that the size of the nanoprecipitates increases with increasing Ga content on approaching the boundary. Furthermore, slow cooling of $x=19$ results in a very sharp Bragg peak, indicating that the nanoprecipitates dramatically grow in size forming a LRO DO_3 phase with time; however, precipitation of DO_3 occurs rapidly for $x=22$, and it was impossible to form a SRO DO_3 -like phase on furnace-cooling.

There is an additional unusual feature in our diffuse scattering data for $x=15, 19$ in the as-grown condition. This is that the peaks were notable asymmetric along the (100) radial direction, in addition to the intensity contour being shifted to lower Q_x . These experimental results were repeated several times on both BT-7 and BT-9. The fact that the asymmetric and off-center features remained present after several thermal cycles from high temperatures indicates that they are intrinsic to the alloys, related to a distortion from the ideal cubic DO_3 structure. We illustrate this peak asymmetry in Figure 5.9 for $x=19$. The sharp peaks near $Q_x=1.2$ and 1.45 are from the (111) and (200) reflections of the Al wires that were used in the

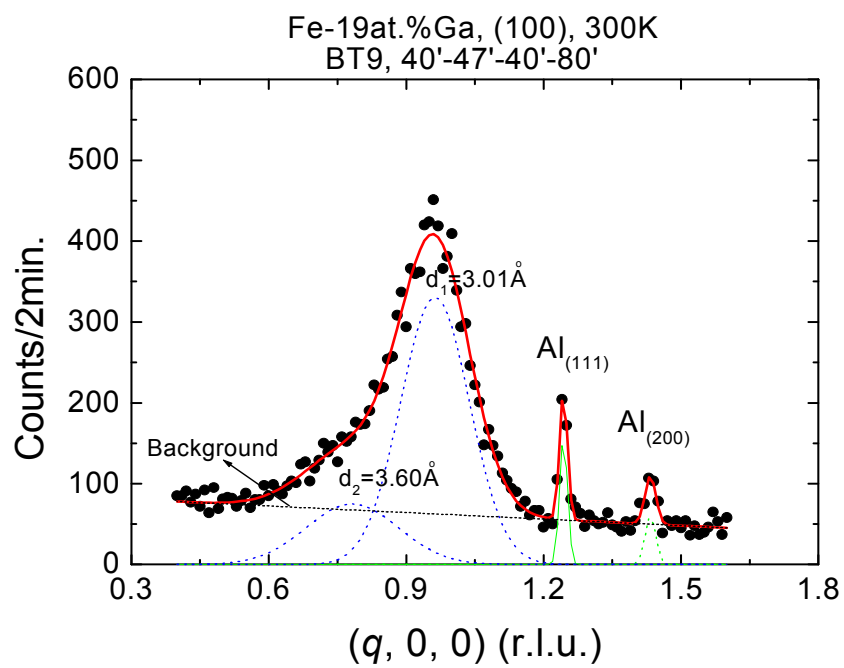


Figure 5.9 Diffuse scattering profile along the radial [100] for the furnace cooled Fe-19at.%Ga.

displex chamber. In order to analyze the peaks, we carefully determined the background intensity as a function of Q_x , using constant counting times and beam collimation measurement conditions. These data are illustrated as a black dotted line in Fig. 5.9. We then fit the entire radial scan using multiple Gaussian peaks and the calibrated background intensity: this peak fitting is illustrated as a solid black line in the figure. Analysis revealed that the diffuse intensity profile of the asymmetric peak was well-fit by two Gaussian peaks: centered at $Q_{x1}=0.965\text{\AA}^{-1}$ ($d_1=3.00\text{\AA}$) and $Q_{x2}=0.805\text{\AA}^{-1}$ ($d_2=3.60\text{\AA}$). Our results show that the DO_3 -like nanoprecipitates for $x=19$ are strongly distorted from cubic symmetry, where the lattice of the DO_3 -like particles has tetragonal or lower symmetry with $c/a\approx 1.2$. This is a very large elastic strain, which is on the order of that of a martensitic alloy.

The findings of Fig. 5.9 support the predictions of step (ii) in the transformation sequence of the structurally heterogeneous model. This model predicted that the DO_3 nanoprecipitates undergo a cubic \rightarrow tetragonal displacive transformation on cooling from DO_3 nanoprecipitates that have a bcc-based DO_3 structure to fct-based DO_{22} one. As shown in Fig. 1.13 (please refer to the Introduction of Chapter 1), part (a) of Figure 1.13 shows the unit cell of the DO_3 structure, which is based on eight ordered bcc unit cells with Ga-Ga atom pairing along the $\langle 110 \rangle$. Part (b) then shows the unit cell of the DO_{22} structure after application of a homogeneous Bain strain. The Bain strain transforms the underlying bcc host lattice of the DO_3 to a new fct-based DO_{22} without atomic interchanges between these atomic sites. In addition, the structurally heterogeneous model predicted that the c/a ratio of the DO_3 -like nanoprecipitates should be on the order of 1.15. This is quite close to our observed value of $c/a\approx 1.2$; in particular, in consideration that the lattice parameters (a_t, c_t) of fct-based DO_{22} cell are unknown. Although we lack a precise structural determination of the lattice parameters of our DO_3 -like phase, we can conclude that (i) the structure is distorted from cubic to tetragonal or lower symmetry; in a matter that is (ii) consistent with a confined bcc $\text{DO}_3 \rightarrow$ fct DO_{22} transformation with a large Bain strain.

Finally, it is important to compare our diffuse neutron results to prior studies of the dependence of magnetostriction on Ga content. These studies have shown that $\frac{3}{2}\lambda_{100}$ is maximum near the boundary between the A2- DO_3 two phase region and the LRO DO_3 single

phase one, near $x=19$: in the same vicinity of the phase diagram that we observed the strongest diffuse scattering intensity. Furthermore, near this boundary region, the value of $\frac{3}{2}\lambda_{100}$ was decreased by furnace-cooling, relative to quenching: similarly, the diffuse intensity was dramatically weakened by furnace-cooling, resulting in formation of a LRO DO_3 phase. Comparisons of our diffuse neutron data and these prior studies reveal a direct causality between structural heterogeneity and enhanced magnetostriction. The enhancement clearly has a structural origin which is related to the volume fraction of DO_3 -like nanoprecipitates. We can infer that enhanced magnetostriction may result from the redistribution of the orientation of lower symmetry DO_3 -like nanoprecipitate particles under field or stress.

5.3 Discussion and Summary

The thermal history dependence of decomposition in Fe– x at.%Ga alloys has been investigated by X-ray and neutron diffraction for the quenched, furnace-cooled, and slow-cooled conditions. Quenching suppresses the formation of the LRO DO_3 phase, whereas slow-cooling favors it. In fact, slow-cooling stabilizes the DO_3 –A2 two-phase field to Ga contents of $x \leq 14$. In situ temperature dependent neutron investigations have shown (i) an increase in the neutron peak linewidth on cooling into the two-phase region, consistent with precipitation of DO_3 clusters constrained within the A2 matrix (the existence of a nanodispersion of DO_3 in the compositionally similar Fe–Al alloys has previously been designed as K-state [86]); (ii) that the linewidth of individual DO_3 peaks is notably less than that of A2 peaks, presumably reflecting that the DO_3 precipitates undergo concurrent ordering upon decomposition; and (iii) that residual line broadening persists into the high-temperature pure A2 phase, which itself is nearly unchanged on cooling.

Diffuse neutron investigations have then shown that the crystal structure of the DO_3 nanoprecipitates within the A2 matrix are in fact strongly distorted from cubic symmetry. This is evidence by an asymmetry of the (100) superlattice reflection intensity and by an off-centering of the (100) zone from $Q_x=1$. Analysis of the diffuse intensity profile revealed a peak-splitting consistent with tetragonal or lower symmetry that has $c/a \approx 1.2$. Investigations

as a function of Ga content revealed that the diffuse scattering intensity was strongest near Fe-19at%Ga, in the vicinity where $\frac{3}{2}\lambda_{100}$ is maximum: for x=15 the intensity was notably less, whereas for x=22 a LRO DO₃ single phase was found. This confirms that enhanced magnetostriction is directly related to the structural heterogeneity of the DO₃ nanoprecipitates.

CHAPTER 6

Conclusion and future work

6.1 Conclusions

In this dissertation, I have performed a systematic investigations of phase transformations, phase fragility, and structural inhomogeneity on highly electrostrictive $(1-x)\text{Pb}(\text{Mg}_{1/3}\text{Nb}_{2/3})-x\text{PbTiO}_3$ (PMN- x PT) crystals and highly magnetostrictive Fe- x at.%Ga alloys having various thermal and field (electric/magnetic) histories, by x-ray and neutron scattering techniques. Many interesting and significant findings have been made during the course of this study.

The main findings can be summarized as follows:

6.1.1 PMN- x PT crystals

- Investigations of phase transformations in electric-field cooled PMN- x PT demonstrated that the phase stability is “fragile”: the phase diagrams can be altered by application of modest electric fields along different crystallographic axes.
- Phase diagrams have been identified for both (001) and (110) field cooled states. Bridging monoclinic M_C or orthorhombic (O) phases were observed to be associated with the T phase, whereas bridging monoclinic M_A or M_B phases with the R phase. Comparisons of the lattice parameters of the different phase fields indicate the possibly “fragility” may only be a perception – as the lattice parameters between O/ M_C and T phases, and between M_A/M_B and R phases are inter-related;
- The ferroelectric adaptive phase model provides an appealing interpretation for the phase fragility observed in PMN- x PT crystals. Analysis of the lattice parameters suggests that in fact the O and M_C phases consist of tetragonal microdomains that are geometrically aligned with respect to each other, in a manner to achieve stress accommodation; whereas the M_A and M_B phases consist of R microdomains. In this case, the O/ M_C (or M_A/M_B) phase may appear to be uniform on a length equivalent or larger than that of the coherence length of x-rays, but in fact consists of a structurally inhomogeneous phases of T (or R) microdomains on a local scale.
- Neutron inelastic scattering of PMN-0.32PT revealed the dynamic origin of the

MPB in PMN-xPT. A softening of the TO mode there appeared to be associated with the formation of polar nanoregions below the MPB, and a long-range ferroelectric one for concentrations above.

These findings are significant, as they expected to extend to other ferroelectric systems: such as PZN-xPT and BaTiO₃ crystals. Our investigations may provide important insights into how to design materials with better performance through nanodomain engineering.

6.1.2 Fe-xat.%Ga alloys

- Investigations of the thermal history dependence of decomposition in Fe-xat.%Ga alloys revealed that quenching suppressed DO₃ formation, whereas slow-cooling favored it. Very slow-cooling stabilized the DO₃-A2 two-phase field to Ga contents of $x \leq 14$; whereas, in situ temperature dependent neutron investigations showed the precipitation of DO₃ clusters constrained within the A2 matrix on cooling into the two-phase region. The precipitation of the thermally stable L1₂ phase was so slow that the metastable DO₃ phase developed.
- Diffuse scattering only appeared when the Ga contents entered the two-phase A2+DO₃ ($14 < x < 22$) region in the furnace-cooled state. In the slow cooled state, a long rang ordered DO₃ phase decomposed out of the A2 matrix. The strongest diffuse scattering was observed for $x=19$, which correspondingly had a maximum magnetostriction: indicating a structural origin for enhanced magnetostriction.
- Diffuse neutron investigations have shown that the crystal structure of DO₃ nanoprecipitates within the A2 matrix is in fact strongly distorted from cubic symmetry. Analysis of the diffuse intensity profile revealed a peak-splitting consistent with tetragonal or lower symmetry that has $c/a \approx 1.2$. This confirms that enhanced magnetostriction is directly related to the structural heterogeneity of the low symmetric DO₃ nanoprecipitates.

6.2 Future work

6.2.1 PMN-xPT crystals

The adaptive phase (or nanotwins) model claims that the ferroelectric monoclinic phases are stress accommodating T or R nanotwins. Our structural findings also revealed the existence of an important crystallographic relationship/transformation between the monoclinic phases (M_C/O and T, M_A/M_B and R). In addition, it is important to note that differences between the [001] and [110] phase diagrams were caused by moderate electric fields of $0.25\text{kV/cm} \leq E \leq 0.5\text{kV/cm}$ – clearly demonstrating that the phase stability of PMN-xPT crystals is quite fragile, or simply put many phases are apparently very close to being energetically degenerate. Therefore, it would be interesting to continue investigations of the structural inhomogeneity and the phase fragility under thermal/electrical histories, especially to obtain further structural information on a nanoscale.

High resolution synchrotron x-ray diffraction in nanotwins

Recent studies of PZT54/46 ceramics have shown very interesting findings [87]. High resolution synchrotron x-ray diffraction study revealed that PZT54/46 has a monoclinic phase, whereas high resolution TEM bright-field images revealed miniaturized nanodomains within tetragonal micro-sized domains. These observations are actually very intriguing, and it will be very interesting and also important to solve this apparent contradiction.

One thing that we try is Brillouin Zone-dependent fine peak structures: which would be a signature of nanotwins. The transition from an adaptive state to a conventional domain structure would provide signatures at finite wave vectors: ones relate to the nanodomains [36] the information of nanodomain sizes. Brillouin zone-dependent diffractions are actually critical experiments that distinguish heterogeneous nanotwins from a homogeneous phase.

Diffuse scattering of nanotwins

In twin-related nanodomain structures, diffuse scattering must obviously result from diffraction from the twin boundaries and domain walls. In addition, the M_C and O phases have different orientations in polarizations from the M_A and M_B ones. It can be expected that the diffuse scattering profiles will be different between M_C/O and M_A/M_B . Therefore, it would be interesting to perform diffuse scattering on PMN-xPT for E applied along both

[001] and [110].

- There would be possibility to study diffuse scattering profiles for these fragile phases, and determine how the diffuse scattering profiles relate to the presence of nanotwins;
- There is also the possibility to study the effect of field on the diffuse scattering between bridging phases.

6.2.2 Fe-xat.%Ga alloys

Our neutron diffuse scattering studies have confirmed that the enhancement of magnetostrictions is directly related to an underlying structural inhomogeneity of DO₃-like nanoprecipitates in the A2 matrix. We have shown that the diffuse scattering is dependent on Ga content in the two-phase A2+DO₃ (14<x<22) region in the furnace-cooled state. The strongest diffuse scattering was observed for x=19, which correspondingly had the maximum magnetostriction. More interestingly, we found that the DO₃-like nanoprecipitates were strongly distorted from cubic symmetry, where the lattice of the DO₃-like particles has tetragonal or lower symmetry with $c/a \approx 1.2$. In addition, it is important to note that the magnetostriction of Fe-19at.%Ga is increased by 30% after quenching, which incidentally results in a higher volume fraction of nanoprecipitates. It is thus reasonable to expect that rapid quenching will result in significant changes in diffuse scattering: including changes in peak intensities, peak broadness, and any possible local tetragonal distortions. Therefore, it would be interesting to continue neutron diffuse scattering studies for various thermal, magnetic and stress histories. I suggest the follows:

- To perform the neutron diffuse scattering on Fe-xat.%Ga (x=10, 15, 19, 22) on “ultra-fast”, and “medium-fast” quenched states; compare these diffuse scattering profiles under different thermal treatments; and try to relate the structural inhomogeneity of SRO DO₃-like nanoprecipitates to any changes in the diffuse scattering profiles;
- To investigate the tetragonal or lower symmetry distortions for the “fast-quenching” states; and try to see if there are any changes in peak shapes and off-centerings;
- To investigate the effect of magnetic field on the diffuse scattering profiles, and on the low symmetry distortions;

- To monitor the magnetostrictions for these various thermal treatments, and compare the results with local structural studies of the DO₃-like nanoprecipitates. Hopefully, this will provide insights into how to design Fe-xat.%Ga alloys that enhance the magneto-elastic properties.

REFERENCE

1. S.-E. Park, T.R. Shrout, J. Appl. Phys. 82, 1804 (1997).
2. Pengdi Han, Weijing Yan, Jian Tian, Xinling Huang, and Huixin Pan, Appl. Phys. Lett., 86, 052903 (2005).
3. A.E. Clark, J.B. Restorff, M. Wun-Fogle, T.A. Lograsso, and D. L. Schlager, IEEE Trans. on Magnetism, vol. 36, p 3238 (2000).
4. A. E. Clark, K. B. Hathaway, M. Wun-Fogle, J. B. Restorff, T. A. Lograsso and V. M. Keppens, G. Petculescu and R. A. Taylor, J. Appl. Phys. 93, 8621 (2003).
5. Robert E. Newnham, Properties of Materials, (Oxford University Press, 2005), 34th page.1
6. A. F. Devonshire, Philos. Mag. 40, 1040 (1949).
7. A. F. Devonshire, Philos. Mag. 42, 1065 (1951); Adv. Phys. 3, 85 (1954).
8. C. Kittel, *Introduction to Solid State Physics*, (1976).
9. W. Cochran, Phys. Rev. Lett., 3, 412 (1959); Adv. Phys., 0, 367 (1960).
10. G. Shirane, J. D. Axe, J. Harada, and J. P. Remeika, Phys. Rev. B 2, 155 (1970).
11. W. Cochran, R. A. Cowley, J. Phys. Chem. Solids, 23, 447 (1962).
12. H. Jaffe and D. A. Berlincourt, “*Piezoelectric Transducer Materials*,” *Proceedings of IEEE*, ~IEEE, Bellingham, WA, 1965!, Vol. 53, pp. 1372–1386.
13. T. Shrout and J. Fielding, IEEE Ultrasonics Symp. 711 (1990)
14. R. E. Service., “*Shape-changing crystals get shiftier*”, Science, 28, 275:1878 (1997).
15. C. Randall, M. Kim, J. Kucera, W. Cao, and T. Shrout, J. Am. Ceram. Soc. 81, 677 (1998).
16. S.F. Liu, S-E. Park, T. R. Shrout, and L. E. Cross. J. Appl. Phys. 85, 2810 (1999).
17. B. Noheda, D.E. Cox, G. Shirane, J.A. Gonzalo, L.E. Cross and S-E Park, Appl. Phys. Lett. 74, 2059 (1999); B. Noheda, J. A. Gonzalo, L.E. Cross, R. Guo, S.-E. Park, D.E. Cox and G. Shirane, Phys. Rev. B, 61, 8687 (2000); B. Noheda, D.E. Cox, and G. Shirane, R. Guo, B. Jones and L.E. Cross, Phys. Rev. B, 63, 014103 (2000).
18. H. Fu and R.E. Cohen, Nature (London) 403, 281 (2000).
19. D. Viehland, J. Appl. Phys. 88, 4794 (2000).

20. Y. M. Jin, Y. U. Wang, A. G. Khachatryan, J. F. Li, and D. Viehland, *J. Appl. Phys.* 94, 1 (2003); Y. M. Jin, Y. U. Wang, A. G. Khachatryan, *Phys. Rev. Lett.*, 91, 197101-1 (2003).
21. B. Noheda, D.E. Cox, G. Shirane, J. Gao and Z.G. Ye, *Phys. Rev. B*, 66, 054104 (2002).
22. B. Noheda, D.E. Cox, G. Shirane, S.E. Park, L.E. Cross and Z. Zhong, *Phys. Rev. Lett.* 86, 17, 3891 (2001).
23. D. La-Orauttapong, B. Noheda, Z.G. Ye, P. M. Gehring, J. Toulouse, D.E. Cox and G. Shirane, *Phys. Rev. B*, 65, 144101 (2002).
24. B. Noheda, Z. Zhong, D.E. Cox, G. Shirane, S.E. Park and P. Rehrig, *Phys. Rev. B*, 65, 224101 (2002).
25. Ohwada, K. Hirota, P. Rehrig, Y. Fujii and G. Shirane, *Phys. Rev. B* 67, 094111 (2003).
26. J. Kiat, Y. Uesu, B. Dkhil, M. Matsuda, C. Malibert and G. Calvarin, *Phys. Rev. B* 65, 064106 (2002).
27. Z. G. Ye, B. Noheda, M. Dong, D. Cox and G. Shirane, *Phys. Rev. B* 64, 184114 (2001).
28. B. Noheda, D.E. Cox, G. Shirane, J. Gao and Z.G. Ye, *Phys. Rev. B*, 66, 054104 (2002).
29. F. Bai, N. Wang, J. Li, D. Viehland, P. Gehring, G. Xu, and G. Shirane, *J. Appl. Phys.* 96, 1620 (2004).
30. D. Vanderbilt and M. Cohen, *Phys. Rev. B* 63, 094108 (2001).
31. F. Jona and G. Shirane, "Ferroelectric Crystals", Pergamon Press, New York, NY (1962).
32. G. Xu, H. Luo, H. Xu, and Z. Yin, *Phys. Rev. B* 64 020102 (2001).
33. Lu, D.-Y. Jeong, Z.-Y. Cheng, and Q. M. Zhang, H. Luo, Z. Yin, and D. Viehland, *Appl. Phys. Lett.* 78, 3109 (2001).
34. S. Wada, S. Suzuki, T. Norma, et al, *Jpn. J. Appl. Phys.* 38(9B) 5505 (1999).
35. M. S. Wechsler, D. S. Lieberman, and T. A. Read, *Trans. J. Metals* 197, 1503 (1953).
36. Yu Wang, et al., *Phys. Rev. B* 73, 014113 (2006); Yu Wang, et al., *Phys. Rev. B* 74, 104109 (2006); Yu Wang, et al., *Phys. Rev. B* 76, 024108 (2007).
37. V. I. Ayurkin and E. S. Jakovleva, *Phys. Status Solidi* 21, 465 (1967).
38. G. Burns and F. H. Dacol: *Solid State Commun.* 48, 853 (1983).
39. P.M. Gehring, S. Wakimoto, Z. G. Ye, and G. Shirane, *Phys. Rev. Lett.* 87, 277601 (2001).
40. Z.-G. Ye and H. Schmid, *Ferroelectrics* 145, 83 (1993).

41. P. M. Gehring, S. E. Park, and G. Shirane, *Phys. Rev. Lett.* 84, 5216 (2000).
42. P. M. Gehring, S. E. Park, and G. Shirane, *Phys. Rev. B* 63, 224109 (2000).
43. C. Stock, H. Luo, D. Viehland, J. F. Li, I. P. Swainson, R. J. Birgeneau, and G. Shirane, *J. Phys. Soc. Jpn.* 74, 3002 (2005).
44. S. Wakimoto, C. Stock, Z. G. Ye, W. Chen, P. M. Gehring, and G. Shirane, *Phys. Rev. B* 66, 224102 (2002); S. Wakimoto, C. stock, R. J. Birgeneau, Z. G. Ye, W. Chen, W. J. L. Buyers, P. M. Gehring, and G. Shirane, *Phys. Rev. B* 65, 172105 (2002).
45. C. Stock, D. Ellis, I. P. Swainson, G. Xu, H. Hiraka, Z. Zhong, H. Luo, X. Zhao, D. Viehland, R. J. Birgeneau, and G. Shirane, *Phys. Rev. B* 73, 064107 (2006).
46. Guangyong Xu, G. Shirane, J. R. D. Copley and P. M. Gehring, *Phys. Rev. B* 69, 064112 (2004).
47. D. La-Orauttapong, H. Toulouse, J. L. Robertson, and Z. G. Ye, *Phys. Rev. B* 64, 212101 (2001).
48. É. du Trémolet de Lacheisserie, *Magnetism I- Fundamentals*, Kluwer Academic Publishers (2003),
49. É. du Trémolet de Lacheisserie, *Magnetostriction theory and applications of magnetoelasticity*, CRS press, (1993).
50. L. Néel, *J. Phys. Radium* 15 225 (1954).
51. A.E. Clark, J.B. Restorff, M. Wun-Fogle, T.A. Lograsso, and D. L. Schlagel, *IEEE Trans. on Magnetics*, vol. 36, p 3238 (2000).
52. A.E. Clark, M. Wun-Fogle, J.B. Restorff, T.A. Lograsso, A.R. Ross, and D. Schlagel, in: H. Borgmann (Ed.), *Proceedings of the 7th International Conference on New Actuators*, Messe Bremen, Bremen Germany, June 2000, p. 1111.
53. E. Tatsumoto and T. Okamoto, *J. Phys. Soc. Jpn.* 14, 1588 (1959).
54. O. Ikeda, R. Kainuma, I. Ohnuma, K. Fukamichi, K. Ishida, *J. Alloys and Compounds* 347, 198 (2002).
55. H. Okamoto, In: H. Okamoto (Ed.), *phase diagrams of binary iron alloys*, ASM International, Materials Park, OH, 1993, p. 147.
56. A. E. Clark, M. Wun-Gogle, J. R. Restorff, T. A. Lograsso and J. R. Cullen, *Ieee Trans. on Magn.* 37, 2678 (2001).

57. A. E. Clark, K. B. Hathaway, et al., *J. Appl. Phys.* 93, 8621 (2003).
58. M. Wuttig, L. Dai, and J. Cullen, *Appl. Phys. Lett.* 80, 1135 (2002).
59. F. Bai, J.F. Li, D. Viehland, D. Wu, and T.A. Lograsso, *J. Appl. Phys.* 98, 023904 (2005).
60. S. Bhattacharyya, J. R. Jinschek, A. Khachatryan, H. Cao, J. Li and D. Viehland, *Phys. Rev. Lett.*, accepted for publication (2008).
61. A. G. Khachatryan and D. Viehland, *Matal. and Mater. Trans. A* 38A, 2308 (2007).
62. G. D. Liu, L. B. Liu, Z. H. Liu, M. Zhang, J. L. Chen, et al., *J. Appl. Phys.* 84 2124 (2004).
63. H. Luo, G. Xu, P. Wang and Z. Yin, *Ferroelectrics*, 231 97 (1999); H. S. Luo, G. S. Xu,, H. Q. Xu, P. C. Wang, and Z. W. Yin, *Jpn. J. Appl. Phys.* 39, 5581 (2000).
64. A.E. Clark, M. Wun-Fogle, J.B. Restorff, T. Lograsso, *Proc. Fourth Pacific Rim Int. Conf. on Advanced materials and Processing (PRICM4)*, Eds. S. Hanada, Z. Zhong, S. Nam, R. Wright, (The Japan Institute of Metals), p. 1711 (2001).
65. C. Stock, W. J. L. Buyers, R. Liang, D. Peets, Z. Tun, D. Bonn, W. N. Hardy, and R. J. Birgeneau, *Phys. Rev. B* 69, 014506 (2004).
66. C. Stock, H. Luo, D. Viehland, J. F. Li, I. P. Swainson, R. J. Birgeneau, and G. Shirane, *J. Phys. Soc. Jap.*, 74, 3002 (2005).
67. S. Wakimoto, C. Stock, Z. G. Ye, W. Chen, P. M. Gehring, and G. Shirane, *Phys. Rev. B* 66, 224102 (2002).
68. D. Viehland and J. F. Li, *J. Appl. Phys.* 92, 7690 (2002).
69. Akhilesh Kumar Singh and Dhananjai Pandey, *Phys. Rev. B*, 67, 064102 (2003).
70. Z. Xu, M. Kim, J. Li and D. Viehland, *Phil. Mag. A* 79, 305 (1996).
71. F. Bai, J.F. Li, and D. Viehland, *Appl. Phys. Lett.* 85, 2313(2004).
72. S. N. Gvasaliya, B. Roessli, R. A. Cowley, S. Kojima and S. G. Lushnikov, *J. Phys.: Condens. Matter* 19, 016219 (2007);
73. J. Hlinka, et al., *Phys. Rev. Lett.* (2001).
74. M. Matsuura, K. Hirota, P. M. Gehring, Z.-G. Ye, W. Chen, and G. Shirane, *Phys. Rev. B* 74, 144107 (2006).
75. G. Xu, Z. Zhong, Y. Bing, Z.-G. Ye, C. Stock, and G. Shirane, *Phys. Rev. B* 67, 104102 (2003).

76. G. Xu, Z. Zhong, Y. Bing, Z.-G. Ye, C. Stock, and G. Shirane, *Phys. Rev. B* 70, 064107 (2004).
77. K. H. Conlon, H. Luo, D. Viehland, J. F. Li, T. Whan, J. H. Fox, C. Stock, and G. Shirane, *Phys. Rev. B* 70, 172204 (2004).
78. G. Xu, P.M. Gehring, C. Stock, K. Conlon, *Phase Transitions* 79, 135 (2006).
79. P. M. Gehring, W. Chen, Z.-G. Ye, and G. Shirane, *J. Phys.: Condens. Matter* 16, 7113 (2006).
80. D. Viehland, L. E. Cross, J. Powers, and J. F. Li, *Appl. Phys. Lett.* 78, 3508-3510 (2001).
81. C. Stock, R. J. Birgeneau, S. Wakimoto, J. S. Gardner, W. Chen, Z.-G. Ye, and G. Shirane, *Phys. Rev. B* 69, 094104 (2004).
82. D. Viehland and J. F. Li, S. J. Jang, L. E. Cross, M. Wuttig, *Phys. Rev. B* 43, 8316 (1991)
83. D. Viehland, S. J. Jang, L. E. Cross, and M. Wuttig, *J. Appl. Phys.* 69 (9), 6595 (1991)
84. J. R. Cullen, A. E. Clark, M. Wun-Fogle, J. B. Restorff, and T. A. Lograsso, *J. Magn. Mater.* 226, 948 (2001).
85. M. C. Zhang, H. L. Jiang, X. X. Gao, J. Zhu, and S. Z. Zhou, *J. Appl. Phys.* 99, 023903 (2006).
86. A.G. Khachaturyan, *The Theory of Phase Transformations in Solids*, John Wiley & Sons, New York, NY, 1983.
87. Kristin A. Schonau, Ljubonira A. Schmitt, et al., *Phys. Rev. B* 75, 184117 (2007).